UNIVERSITÀ DEGLI STUDI DI PARMA

DOTTORATO DI RICERCA IN INGEGNERIA INDUSTRIALE

XXIII CICLO

Study, automation and planning of micromachining processes based on infrared pulsed Fiber Laser

Coordinatore: **Chiar.mo Prof. Marco Spiga**

Tutor: **Chiar.mo Prof. Roberto Groppetti**

Dottorando: **Stefano Pini**

To my family,
for their constant support.

To Sara,
for just being here.

Acknowledgements

First and foremost, I would like to thank my advisor Prof. Roberto Groppetti for his support and assistance during the past three years. I would also like to thank Prof. Nicola Senin for providing firm support and constructive feedback during the course of my Doctorate research.

I am particularly grateful to Professor David R. Wallace for welcoming me at the CADlab of the Massachusetts Institute of Technology: the time spent in the lab proved to be a very enriching experience.

I would like to acknowledge the support of this work by several industrial partners. SM Srl (Lombardore, Torino, Italy) and LaserPoint Srl (Vimodrone, Milano, Italy) provided some of the components used to implement the Fiber Laser micromachining system presented in this thesis. Lafer Spa (Borghetto di Roncaglia, Piacenza, Italy) supplied the DLC-coated stainless steel specimens used in the experimental activities. Finally, Olympus Italia Srl (Segrate, Milano, Italy) and Remet Sas (Casalecchio di Reno, Bologna, Italy) offered the use of the Olympus LEXT confocal microscope which was employed to measure and characterise the microfeatures generated during the experiments.

Lastly, I offer my regards to all of those who supported me in any respect during the completion of the Doctorate course.

Contents

List of Figures

List of Tables

Listings

Introduction

Microtechnology has become a word of wide use in the last two decades. The term itself has acquired a broad meaning and comprehends a wide range of fields in many disciplines: it concerns the design, characterization and production of structures, devices and systems by controlling their shape and size at the micrometer scale.

In particular, the term *micromanufacturing* refers to the production of high-precision three-dimensional products, with sizes ranging from tens of micrometers to a few millimeters [5, 6]. Microcomponents are generated by means of a variety of processing methods [7, 8], which can be classified into *material addition*, *shape change* and *selective material removal*.

Micromanufacturing processes based on material addition employ additive types of microfabrication that rely on the repeated deposition and patterning of material. Examples are *stereolithography* [9], *LIGA processes* [10] and *micro-injection moulding* [11]. Bulk production of microparts with high accuracy can be realised by these technologies, but costs are high and the number of different materials is limited (for the most part to polimers). For these reasons, their application is essentially restricted to MEMS fabrications.

Microproducts may be produced with plastic forming technologies, that is to say by changing the shape of the workpiece without any addition or removal of material [12]. *Microforming* is particularly suited for mass production of metallic parts, due to the higher production rate when compared

to other micromanufacturing techniques. Nevertheless, the applicability of the process to the production of microparts is limited by size effects and handling difficulties, which may lead to low accuracy and uncertain mechanical properties of the resulting microcomponents [13].

Several processes can be employed to modify the shape of a workpiece by selectively removing material. *Mechanical micromachining* processes are scaled down versions of the traditional cutting processes: material removal is obtained as a result of the mechanical interaction of a sharp tool with the workpiece material [14]. This category of material processing techniques can provide high material removal rates, while at the same time achieving good accuracy and low surface roughness. However, a number of issues remain to be addressed, including the understanding of the chip formation mechanism and the design of machine tools with adequate dynamics stiffness [15].

A major drawback of microcutting processes is the relatively high machining force required for the chip formation. This influences the machining accuracy, due to the deflection of tool and workpiece, and it is particularly important for micromachining of hard or brittle materials. Another important issue is the fabrication of microtools: the tool edge radius must be smaller of the cut thickness and the cutting edge must present high uniformity [16].

In recent years, numerous investigations have focused on the application of *micro-electric discharge machining* (μ-EDM) to the generation of microfeatures on microcomponents [17, 18]. The μ-EDM process is based on the difference of potential created between a workpiece and an electrode which are submerged in a dielectric fluid. When the distance between electrode and workpiece is reduce, a pulsed discharge occurs, eroding the surface material through melting and evaporation. The process can achieve good accuracy and it is suited to micromachining of hard-to-cut materials, since the absence of contact between tool and workpiece makes the hardness of the workpiece material not critical. However, the inability of μ-EDM to process non-conductive

materials and its limited productivity prevent a wider adoption of the process.

Laser beam micromachining is an advanced thermal machining process in which the material is selectively removed by melting, vaporization and chemical degradation of the material [19, 7]. In particular, short-pulsed lasers have many practical advantages over conventional lasers: when the laser beam is delivered to the workpiece surface, the reduced length of the pulses achieves material removal without thermal effects on the remaining structure. Thermally induced damage of the workpiece material is therefore avoided, as opposed to standard laser material processing techniques with longer pulse length. Moreover, materials traditionally difficult to cut can be easily processed, since no mechanical contact between the workpiece and the tool (the laser beam) is required.

Fiber lasers [2] have gained increasing popularity as an efficient, reliable and compact solution for micromachining. The high beam quality of fiber lasers enables focusing of the laser beam to a small spot with high power density. Such characteristic is essential for several micromachining processes. In laser *microdrilling*, a laser beam is employed to drill holes with micron or submicron resolution into surfaces [20]. The laser *microcutting* and *microgrooving* processes are used to create blind cut or through-cut for various manufacturing applications: the excess material is removed by scanning a laser beam over the workpiece surface [21]. Laser *microwelding* offers temperature resistant high strength joining, without need for filler material [22, 23]. Finally, laser *microcladding* utilises a laser beam as energy source to melt and apply a material onto a substrate [24].

Laser micromachining is a complex dynamic process, which is influenced by numerous parameters. Traditionally, the selection of process parameters has been performed via a *trial and error* method. Such a technique is non-systematic, time-consuming and it is not guaranteed to output an optimum combination of the process parameters. These limitations can be overcome by

means of more systematic studies, which allow for prediction of the interactive effects of the process input parameters on the process outcome.

However, the definition of a laser micromachining process for micromanufacturing of a part does not end with the selection of the laser process parameters, but it requires the complete definition of all the single machining operations, their allocation in the specific order, the calculation of process time and costs as well. This is based on the analysis of the part design data and of shape, size, tolerance, location, orientation and mutual relationship of the various geometric microfeatures which compose the micropart. Such process is defined as *process planning* and it is documented in terms of a *part program*.

Process planning requires the evaluation of a number of alternative process plans, within a limited time frame, and such a task requires extensive manufacturing knowledge and experience. For these reasons, Computer Aided Process Planning (CAPP) has been introduced, to take advantage of modern computer consistency and computing power in process planning.

Process planning translates *design information* into *process steps* and *instructions*, in order to efficiently and effectively manufacture products. Therefore, CAPP represents the natural link between Computer Aided Design (CAD) and Computer Aided Manufacturing (CAM).

In the scope of this thesis, the interface between the CAPP/CAM system and the Computer Numerical Control (CNC) machine is particularly important. The traditional approach, based on the use of rigid-syntax procedural languages (ISO code, APT code), is slow and it requires the planner to be familiar with part programming in general and with the particular set of commands of the CNC language of choice.

This issue is particularly important in Fiber Laser micromachining processes, since the difficulties in defining part programs for microparts machining may result in a reduction of the optimum flexibility characteristics of the

process.

In this thesis, micromachining processes based on infrared pulsed Fiber Laser are studied in the perspective of their optimisation. To this end, an experimental micromachinining setup based on an infrared pulsed Fiber Laser source is designed and integrated. The emission of laser radiation is coordinated with a part positioning system: the relative motion established between the laser beam focusing device and the workpiece surface allows for thee-dimensional microfeatures to be machined.

A new approach to part programming for laser micromachining is proposed, based on the use of natural language for the generation of part programs for Pulsed Fiber Laser micromachining. Under the new approach, the traditional ordered list of program blocks in a ASCII formatted file is replaced with almost free syntax, non procedural sentence commands, expressed in natural language, without any particular syntax constraints. The input processor system is responsible for the interpretation and translation of the input according to a statistical knowledge base learnt from real-world examples.

Overview

This dissertation is divided in 5 main chapters:

Chapter 1 In this chapter, laser devices are introduced. The properties of the emitted radiation, the principles of the laser beam generation and the mode of operation of a laser source are explained. Subsequently, the main laser active media and laser architecture employed in industrial laser applications are described, with particular focus on fiber lasers.

Chapter 2 The fundamentals of laser material processing are presented. The principles of interaction between material and laser radiation and the resulting thermal effects are explained. Finally, after a theoretical

analysis of laser-induced material removal, the laser microcutting, laser microdrilling and laser microgrooving processes are reviewed.

Chapter 3 In this chapter, the design and automation of a micromachining setup based on a infrared pulsed Fiber Laser source are presented. Detailed descriptions of the components, of the control system and of the user interface are given.

Chapter 4 In this chapter, the problem of process planning for fiber laser micromachining is presented and a new approach to part programming based on free syntax, non procedural commands expressed in natural language is presented. After an introduction to stochastic modelling and Hidden Markov Models, a formal description of the proposed approach is given.

Chapter 5 Experimental investigations conducted with the fiber laser micromachining system on AISI 304 stainless steel strips and on DLC-coated AISI 440 stainless steel specimens are reported in this chapter.

Chapter 1

Laser theory and operation

Laser is an acronym for *Light Amplification by Stimulated Emission of Radiation*, where light denotes electromagnetic radiation of any frequency. Laser light is essentially a coherent, convergent, and monochromatic beam of electromagnetic radiation with wavelength ranging from ultraviolet to infrared [1].

Light may be treated either as a wave according to Maxwell's theory, or as a quantum mechanical stream of particles called photons. Classically, electromagnetic radiations consist of propagating waves associated with the oscillating electric field ($\vec{B}$) and magnetic field ($\vec{H}$), which oscillate in phase perpendicular to each other and also perpendicular to the direction of energy propagation.

Conventionally, the description of the wave considers the oscillation of the electric field vector only, since the magnetic field is perpendicular to the electric field and proportional to it. When the oscillations of the electric field vector are in a particular order, the light is said to be polarized. Fig. 1.1 shows a schematic of a plane-polarized wave: the electric field varies in space and time along the y axis sinusoidally, according to Eq. (1.1):

$$E = \sin 2\pi \left(\frac{x}{\lambda} - \nu t\right), \tag{1.1}$$

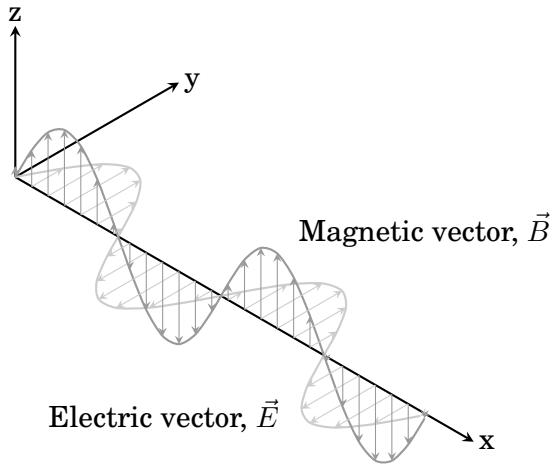

Figure 1.1: Propagation of a plane electromagnetic wave in space.

where A is the amplitude, λ is the wavelength and ν is the frequency of the wave.

Quantum mechanically, the electromagnetic radiation is thought of as a stream of particles called photons. Each photon is associated with an amount of energy, which is proportional to its frequency and can be expressed as:

$$E = h\nu = h\frac{c}{\lambda} \tag{1.2}$$

where h is the Planck constant ($6.63 \times 10^{-34} J/s$) and c is the velocity of light.

It is evident from Eq. (1.2) that the shorter the wavelength of the light is, the higher the energy of the photon results; consequently, ultraviolet light (short wavelength) is more energetic than infrared light (longer wavelength).

1.1 Laser generation mechanism

Electrons in atoms can occupy many different energy levels. The further away an energy level is from the nucleus, the higher its energy. Under the right circumstances an electron can move from the lowest-energy orbit (*ground state*) to a higher state (*excited state*). In the same way, it can move from an excited state to a lower state (*decay*), but it cannot remain in any

position between those two states. These allowed energy states are referred to as *quantum states* (Fig. 1.2).

The transition between different quantum states is driven by the absorption or emission of energy. When an electron moves to a higher quantum state, the atom must receive energy through one of several mechanisms, such as semielastic collisions or electromagnetic radiation absorption. In the same way, when an electron drops to a lower quantum state, energy must be released as kinetic energy or electromagnetic radiation. In the scope of laser physics, only transitions with absorption or emission of radiative energy are considered.

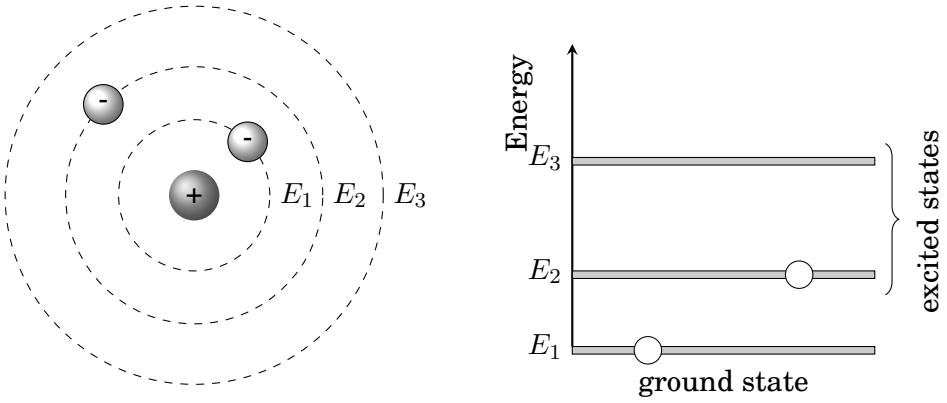

Figure 1.2: Simplified energy-level diagram.

For a transition to occur from a lower energy state E_n to a higher energy state E_m, the photon energy, as expressed by the Planck relationship (Eq. 1.2), must be equal to the energy difference of the considered pair of quantum energy states:

$$\Delta E = E_m - E_n = h\nu. \tag{1.3}$$

Consequently, the wavelength of the absorbed photon must be:

$$\lambda = \frac{hc}{E_m - E_n}. \tag{1.4}$$

If no pair of energy states with energy difference equal to the particular photon energy is available, the matter will be transparent to that radiation and no absorption will occur.

Similarly, when an electron decays from a higher quantum state to a lower energy level, the excess energy is released by emitting a photon with energy equal to the energy difference of the pair of quantum energy states and with wavelength as expressed by Eq. (1.4).

1.1.1 Stimulated emission

In general, when an electron occupy an excited energy state, it will spontaneously return to its ground state or to some intermediate energy level after an average time τ, by emitting a photon of radiation in a random direction and at random phase. This phenomenon is called *spontaneous emission*. However, it is also possible that an electron already in an excited state is reached by an incoming photon with suitable photon energy; in that case, the passing photon may cause the electron to decay in such a manner that a photon is emitted with exactly the same wavelength, direction and phase as the photons of the incident wave, effectively generating a second photon of the same energy (Fig. 1.3) [25]. In effect, if a group of atoms all in the same excited state interacts with an incoming radiation at the exact wavelength, the intensity of the incoming radiation is amplified. This process is called *stimulated emission* and it represents the physical basis of light amplification in laser devices.

However, in a real population of atoms, not all the atoms are in an excited state. In general, the relative populations N_2 and N_1 of the upper and lower energy levels, respectively, are distributed according to the Boltzmann's principle:

$$\frac{N_2}{N_1} = \exp \frac{-(E_2 - E_1)}{kT}, \tag{1.5}$$

where T is the equilibrium temperature and k is the Boltzmann constant.

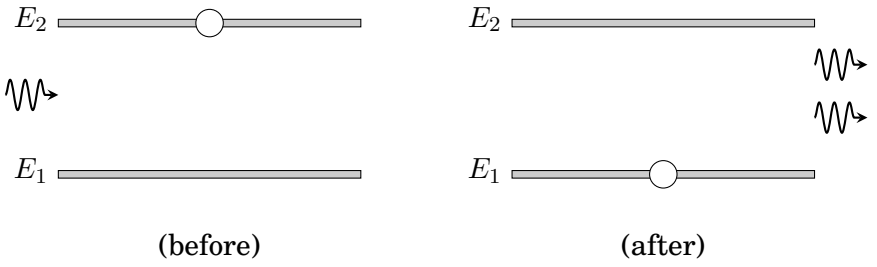

Figure 1.3: Schematics of stimulated emission.

It is seen from Eq. (1.5) that for a system in thermal equilibrium the lower energy state N_1 is more populated than the higher energy level N_2, and therefore this is the normal state of the system. As the temperature increases, the number of electrons in the high-energy quantum state increases, but N_2 cannot exceed N_1, since even at infinite temperature the N_2 populations only reaches N_1. Consequently, *population inversion* ($N_2 > N_1$) can never occur in a system at thermal equilibrium. Since the probability for an atom in the lower energy state to absorb a photon is the same as the probability for an atom in the excited state to emit a photon through stimulated emission, it is clear that a population of atom in thermal equilibrium can only be a net photon absorber, therefore making amplification of the incoming radiation impossible. For that reason, in order to achieve laser radiation emission a population inversion must be established by pushing the system into a non-equilibrated state.

1.1.2 Population inversion

As described above, a population inversion is required for laser operation: the term refers to a non-equilibrium distribution of electrons such that the higher energy states have a larger number of electrons than the lower energy states.

To obtain non-equilibrium conditions, a method of artificially populating

the higher excited state must be used. The process of achieving the population inversion is usually referred to as *pumping*.

In most of lasers, population inversion generally involves three or four energy levels. A *four-level laser* system requires four different energy levels, with energies E_1, E_2, E_3, E_4, and populations N_1, N_2, N_3, N_4, respectively. The energies associated to each level are such that $E_1 < E_2 < E_3 < E_4$. The schematic of such a system is reported in Fig. 1.4.

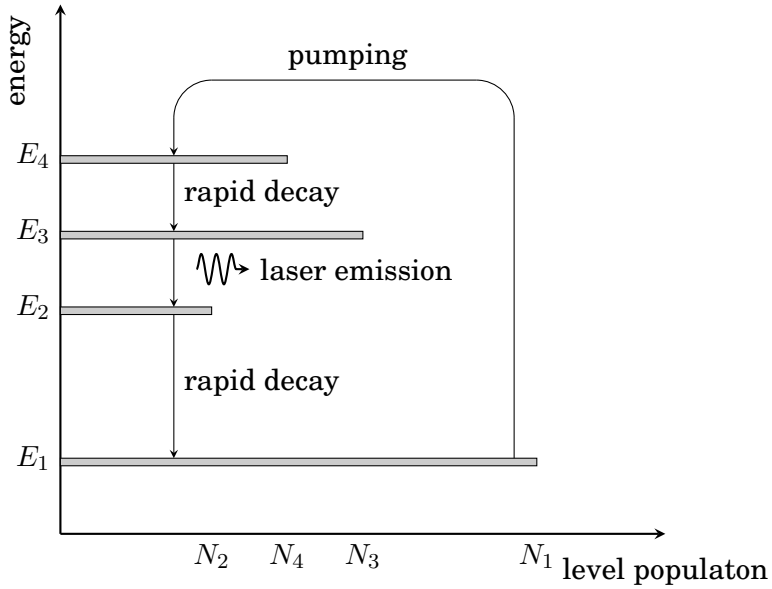

Figure 1.4: A four-level laser energy diagram.

In this system, electrons are pumped from energy level E_1 to E_4 by the absorption of pumping radiation of frequency $\nu = (E_4 - E_1)/h$. The atoms decay from level N_4 by a fast, non-radiative transition into the metastable level N_3. The lifetime of such laser transition is much shorter than that of the following transition from level N_3 to level N_2 ($\tau_{3\to2} \gg \tau_{4\to3}$). Therefore, electrons accumulate in level N_3 and a population inversion is achieved between level N_3 (*upper laser level*) and N_2 (*lower laser level*). The now established population inversion allows the emission of radiation through stimulated emission at frequency $\nu_{3\to2} = (E_3 - E_2)/h$. This light is very similar to the input signal

in terms of phase and polarization.

Ideally, the lower laser level should be well above the ground state: if this condition is satisfied, level E_2 is quickly depopulated and no appreciable population density can occur. On the other hand, if the energy difference between level E_1 and level E_2 is comparable to the quantity kT in Eq. (1.5), then some population will exist in thermal equilibrium in the lower laser level at the operating temperature, as given by the Boltzmann distribution. Such a system is called a *quasi-three-level laser*.

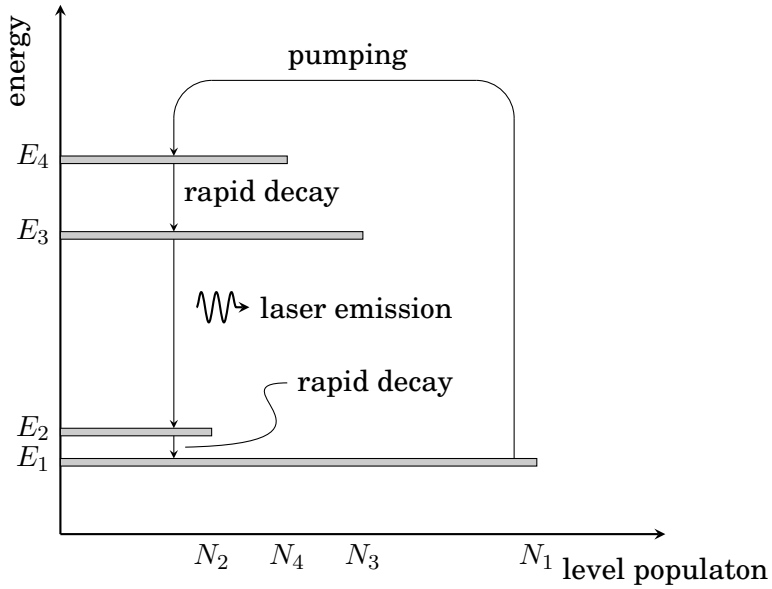

Figure 1.5: Energy diagram if a quasi-three-level laser.

Non-zero population of the lower laser level leads to partial reabsorption of the laser emission. Such reabsorption does not constitute a real loss of energy, because it excites ions into the upper level, so that stimulated emission can again occur at a later time. However, the higher pump energy densities needed to overcome reabsorption may lead to higher losses through fluorescence.

On the other hand, the reduced energy difference between ground level and lower laser level give an important advantage: the wavelength of the

laser radiation is not much longer than the pump wavelength, meaning that the energy of the laser photons is closer to the energy of the pump photons (small *quantum defect*). As a consequence, quasi-three-level lasers can potentially achieve very high power, to the detriment of overall wall-plug efficiency [4].

1.1.3 Laser resonators

Although the population inversion condition consents the amplification of the incoming signal, the single-pass gain is small and a large part of the electrons in the excited state decay spontaneously, thus not contributing to the overall output. Moreover, spontaneous emission radiation emerges in all directions, effectively acting as a superimposed random noise on the coherent radiation generated by stimulated emission.

To obtain laser radiation, a mechanism is required to cause most of the atoms in the population to contribute via stimulated emission to the coherent output. This process is realized by employing a *laser resonator*, which typically consists of a pair of mirrors between which a coherent beam of light travels in both directions. Generally, one of the mirrors is fully reflective, while the other has a partially transmitting coating, which allows a fraction of the radiation to escape from the resonator (Fig. 1.6). The purpose of the mirrors is to provide *positive feedback*. This means that some of the light is reflected from side to side within the cavity several times, so that an average photon will pass through the gain medium repeatedly, for further amplification. As the photons are reflected back and forth, they interact with more and more atoms, moving the equilibrium towards stimulated emission, which now predominates. As a result, coherent laser radiation is emitted from the partially reflective mirror.

For simplicity, in the above discussion the reflective mirrors have been assumed to be flat. However, other configurations may be used, depending on

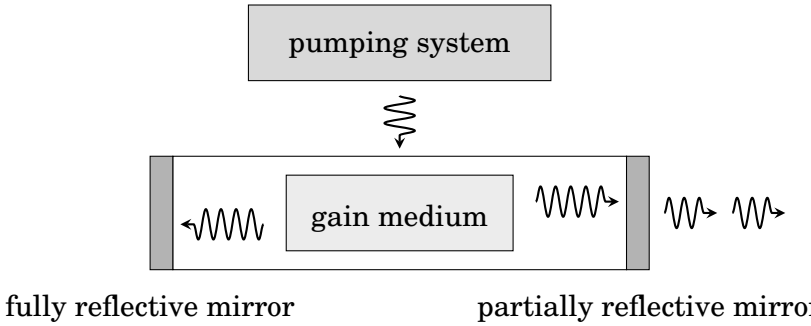

Figure 1.6: Schematic driagram of a laser resonator.

the design of the oscillator. The geometry of the mirror impacts on the extent of *mode volume* and on the *stability* of the cavity. Mode volume is defined as the fraction of the laser medium with which the oscillating radiation interacts in the cavity, while stability indicates the ability of the cavity to retain the light after several reflections.

The plane parallel mirror design maximise the mode volume, but it lacks stability, since any slight misalignment between the mirrors causes the light to spread towards the side of the cavity, resulting in the beam eventually growing larger than the mirrors and leaving the optical system. On the other hand, spherical mirror designs have smaller mode volume, but increased stability.

1.2 Resonator modes

Laser radiation is automatically generated within the laser resonator at frequencies which correspond to resonances (*resonator eigenmodes* or simply *modes*). Resonator modes are radiation distributions inside the resonator which reproduce themselves on every round-trip of the light due to the effect of interference. They can be divided into two categories: *longitudinal* modes and *transverse* modes.

1.2.1 Longitudinal modes

The longitudinal resonator modes correspond to the wavelengths which are reinforced by constructive interference after many reflections. The resonance condition for light with wavelength λ in oscillation within a plane-mirror cavity of length d can be expressed as:

$$d = \frac{n\lambda}{2}, \tag{1.6}$$

where n is an integer value called *mode order*. Eq. (1.6) shows that allowed modes are only those for which the distance between the mirrors is an exact multiple of half the wavelength of the light. The frequence separation between two adjacent modes is therefore given by

$$\nu = \frac{c}{2d}. \tag{1.7}$$

Only modes whose frequencies are within the stimulated emission range of the gain medium are responsible for the generation of the laser output, as shown in Fig. 1.7.

Since the amplification bandwidth is usually broader than the cavity mode spacing, many lasers operate on several cavity modes simultaneously.

1.2.2 Trasversal modes

The transverse mode are patterns of radiation which occur in a plane perpendicular to the direction of propagation of the light wave. In the simplest case, transverse intensity distribution of the electromagnetic radiation is approximated by a Gaussian function, as expressed by:

$$I(r) = I_0 \exp\left(\frac{-2r^2}{w^2}\right), \tag{1.8}$$

where r is the radius of the beam, I_0 is the intensity of the beam at $r = 0$, and w is the radius of the beam at the beam waist. In this case, the laser is

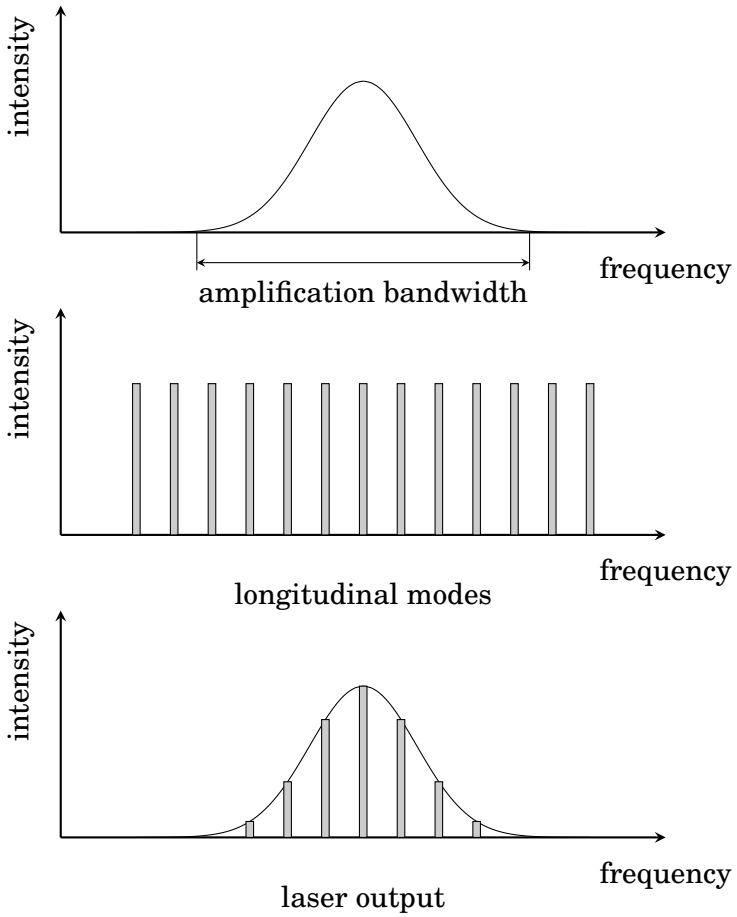

Figure 1.7: Structure of laser spectrum.

said to be operating on the fundamental transverse mode of the laser optical resonator and the laser beam is called *Gaussian beam*.

In addition to the Gaussian mode, a resonator may have other higher-order modes which present more complicated intensity distributions. For laser with field distributions with rectangular symmetry, the electric field intensity can be expressed as a product of two Hermite polynomials and two Gaussian functions (*Hermite-Gaussian* modes):

$$I_{mn}(x,y) = I_0 \left[\mathrm{H}_m \frac{\sqrt{2}x}{w} \exp\left(\frac{-x^2}{w^2}\right) \right]^2 \left[\mathrm{H}_n \frac{\sqrt{2}y}{w} \exp\left(\frac{-y^2}{w^2}\right) \right]^2 , \tag{1.9}$$

where the subscripts m and n indicate the order of the Hermite polynomial

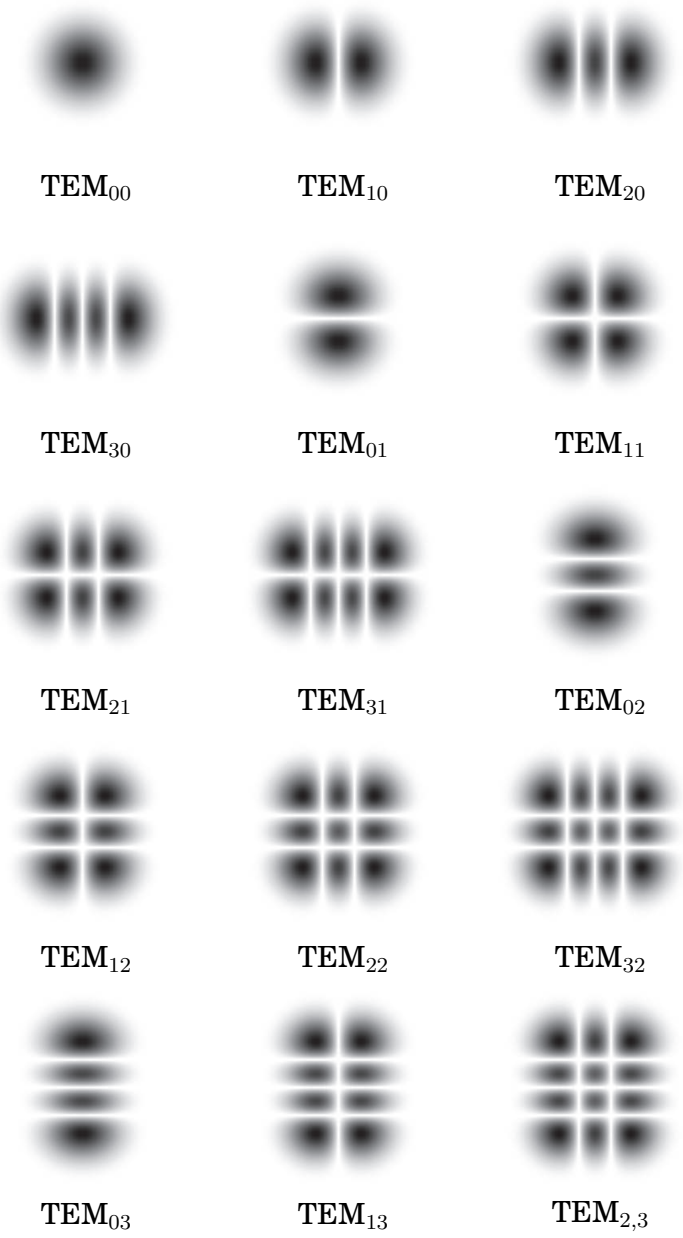

Figure 1.8: Intensity distributions of laser radiation for different TEM_{nm} modes.

H and they are correlated to the number of nodes in the x and y direction. These modes are indicated by TEM_{mn} (Fig. 1.8). It should be noted that TEM_{00} corresponds to the basic Gaussian mode.

1.3 Laser temporal mode of operation

A laser can operate in either *continuous* or *pulsed* mode, depending on whether the power output has continuous constant amplitude over time or whether its output takes the form of pulses of light.

In *continuous wave* (CW) mode, the pumped energy is discharged uninterruptedly over time. In pulsed mode, the pumped energy is stored until a threshold is reached and then rapidly discharged into short pulses with high energy density. Pulsed lasers mainly implement the pulsing in two ways: *Q-switching* and *mode-locking*.

1.3.1 Q-switching

Q-switching is a technique for generating energetic short pulses from a laser by modulating intra-cavity losses. Q-switching derives its name from the *Q factor* (*quality factor*), which is a measure of the strength of the damping of oscillations in an oscillator. At first, losses in the laser resonator are kept at a high level (low Q factor). Since no laser output is generated, the pump energy accumulates into the gain medium. Then, losses are suddenly reduced (high Q factor), so that the power of the laser radiation builds up very quickly in the laser resonator. The stored energy emerges as short and intense pulse of laser light.

Q switching can be either *passive*, when losses are automatically modulated by a saturable absorber (a material whose optical losses decrease when the intensity of light exceeds some threshold), or *active*, if losses are modulated by an active control element, typically an acousto-optic, electro-optic or

mechanical modulator.

Pulse duration in the nanosecond range and pulse repetition rates up to $100kHz$ can be obtained by Q-switching laser systems.

1.3.2 Mode-locking

Mode-locking is a method to obtain ultrashort pulses from lasers by inserting in the laser resonator either an active element (an optical modulator) or a nonlinear passive element (a saturable absorber). These elements cause the longitudinal modes of the oscillator to operate with a fixed phase difference, thus constructively interfering with one another periodically. The resulting modulation of the light being reflected within the laser resonator leads to the formation of an ultrashort pulse of light, which circulates in the laser resonator at a fixed frequency. Each time the pulse hits the partially reflective mirror, an output pulse is emitted, so that the laser output consists of short and equally spaced laser pulses.

Typical values of pulse duration and pulse repetition rate for mode-locking laser operation are in the femtosecond range and in the MHz to GHz range, respectively.

1.4 Properties of laser radiaton

The light emitted by laser devices differs from that produced by common light sources with respect to some unique properties, which arise from the stimulated emission process providing the amplification mechanism.
These properties are:

- *monocromaticy*: laser light has very narrow finite bandwidth, thus being regarded as highly monochromatic;
- *collimation*: laser light propagates with very small *divergence*, i.e., with

approximately constant beam radius. As a result, laser light can be focused on a very small area at long distances.

A laser beam is defined *diffraction-limited* when its potential to be focused to small spots is limited only by the effects of diffraction. For a given optical power and wavelength, a diffraction-limited beam has the highest brightness, i.e. its beam quality is ideal. The degree of collimation of such a laser beam is related to the beam divergence angle, which can be expressed as:

$$\sigma = \frac{\lambda}{\pi w_0}, \tag{1.10}$$

where w_0 is the beam waist radius and d is the aperture of the resonator cavity (Fig. 1.9).

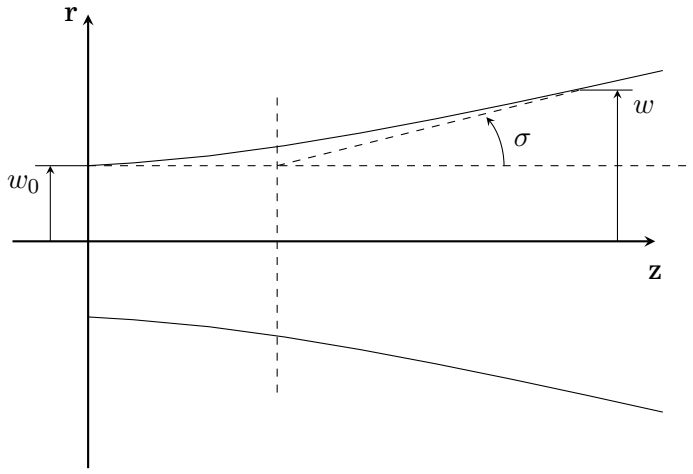

Figure 1.9: Schematic of the propagation in space of a Gaussian beam described by the divergence angle.

Eq. (1.10) can be generalized to any laser beam by means of the *beam propagation factor* M^2, defined as the ratio of the divergence of a beam to that of a perfectly coherent beam [26]:

$$\sigma = M^2 \frac{\lambda}{\pi w_0}. \tag{1.11}$$

M^2 is commonly used as a measure of the beam quality of a laser, since a higher beam divergence for a given beam radius is related to an inferior beam quality, and therefore to a lower potential for focusing the beam to a very small spot;

- *coherence*: laser light is coherent because there is a strong correlation (fixed phase relationship) between the electric field values at different locations (*spatial* coherence) and at different times (*temporal* coherence).

1.5 Industrial lasers

Since the development of the first lasers in the 1960s, hundreds of materials have been investigated as lasing active medium. However, only a limited number have found application in commercial laser systems (Fig. 1.10 and 1.11). A description of the main categories of laser media is given in the following.

- *Gas lasers* use a gas as active lasing medium: electric current is discharged through the gas to produce laser light. Laser gas sources have the advantages of using a high volume of a relative inexpensive, not damageable active material, but they are usually larger in size than solid-state laser, due to the low density of the gas medium. The most common example of gas laser is the CO_2 laser, which is widely used in material processing application.

- *Solid-state lasers* use a crystalline or glass rod which is doped with impurity ions, where the population inversion is generated and maintained. The doped materials are pumped optically by a radiation with shorter wavelength than the lasing wavelength. Nd:YAG laser are the most common example in the field of material processing.

- *Excimer lasers* are based on diatomic molecules that are stable in the excited state and unstable in the ground state (excimer). Highly inert noble gases are used: when in an excited state, they can form temporarily-bound molecules, which soon release the excess energy by undergoing spontaneous or stimulated emission. The resulting strongly-repulsive ground state molecule is unstable and therefore disassociates into two unbound atoms, creating a population inversion between the two states. Excimer laser are typically excited with electrical discharges.

- *Liquid dye lasers* use an organic dye as active lasing medium. Since the dye molecules efficiently absorb and emit radiation over a broad range of wavelengths, dye laser can be tuned to operate over a wide range of frequencies.

- *Semiconductor lasers* are electrically pumped diodes. Under an applied current, electrons and holes are forced into the depletion zone of a *p-n* junction. When electrons recombine with holes, they fall into a lower energy level and release energy in the form of photons. Under the right condition, stimulated emission may take place, resulting in optical gain. A resonator cavity around the active region completes the laser.

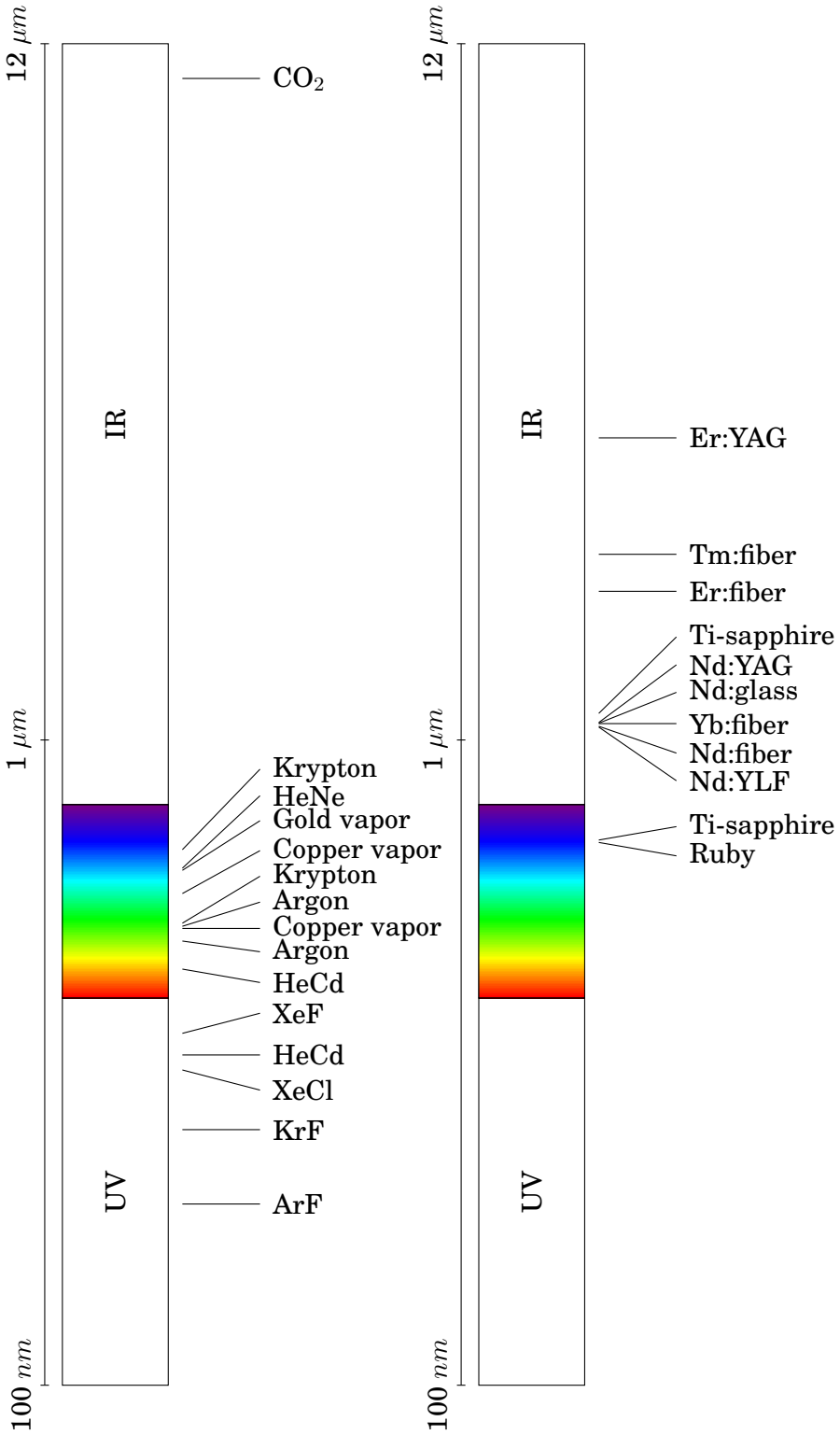

Figure 1.10: Typical wavelengths of common gas lasers (above) and solid-state lasers (below) [1, 2].

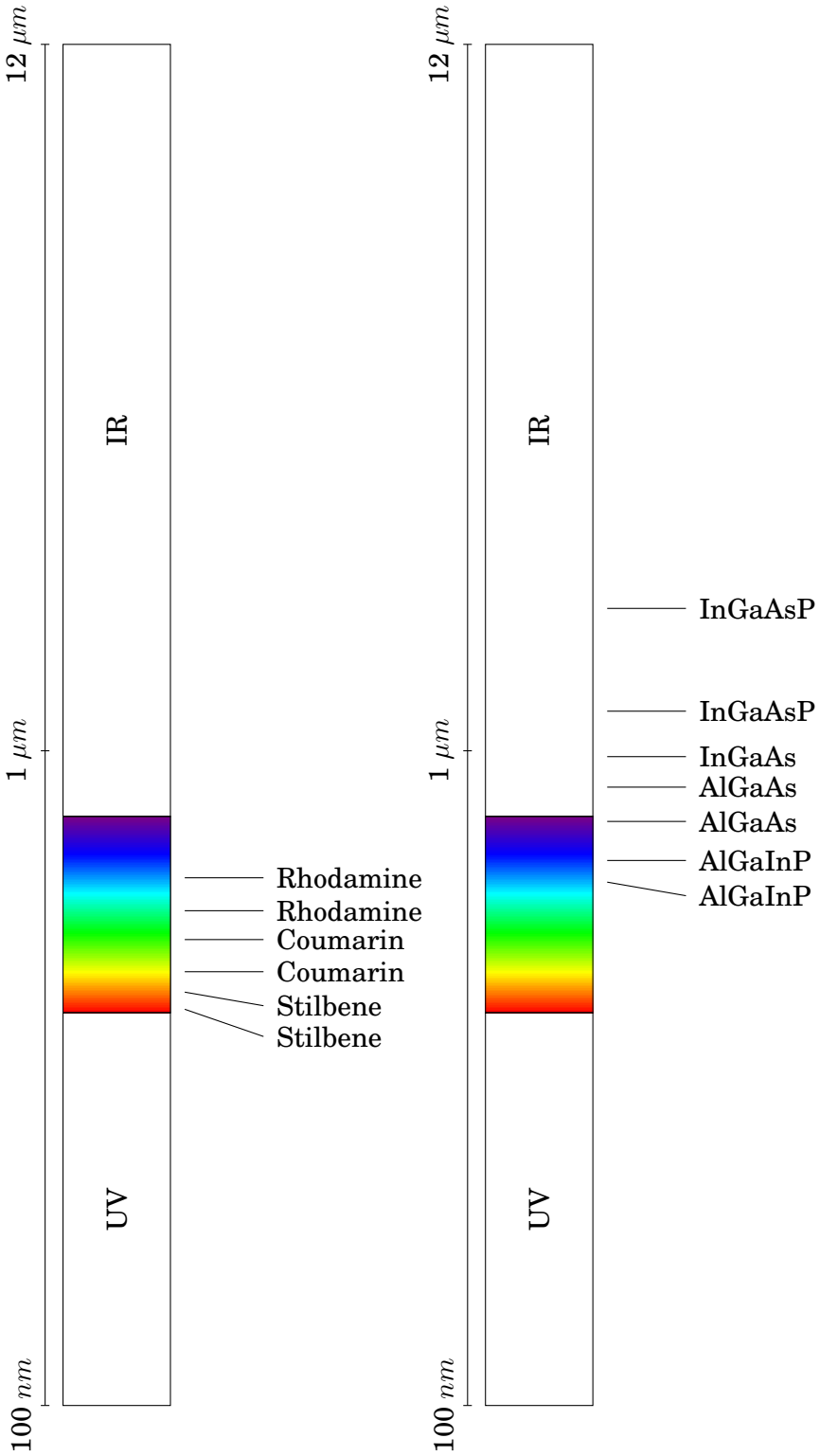

Figure 1.11: Typical wavelengths of common dye lasers (above) and semiconductor lasers (below) [1, 2].

1.6 Fiber laser

Fiber lasers are solid-state lasers which employ optical fibers as gain media (Fig. 1.12). The core of the fiber is doped with rare-earth elements, such as erbium (Er^{3+}), neodymium (Nd^{3+}), ytterbium (Yb^{3+}), thulium (Tm^{3+}).

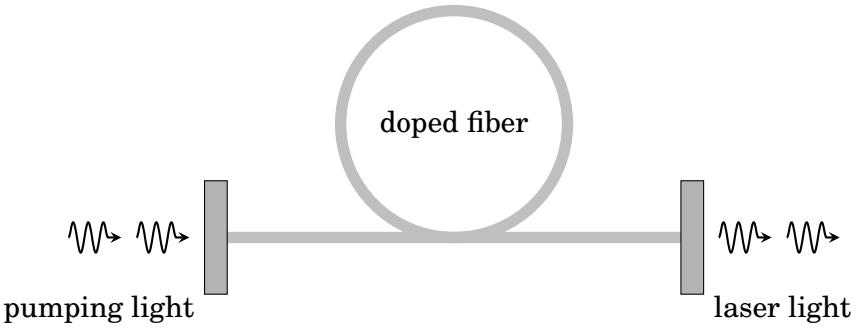

Figure 1.12: Schematics of a simple fiber laser.

The use of a doped optic fiber as lasing medium offers several advantages when compared to bulk solid-state laser [27]:

- rugged and compact setup: fiber lasers usually consist of a monolithic combination of fiber-based components, with no need for optical alignment and no potential for external contamination;
- simplified thermal management: the much larger surface-to-volume ratio of fiber-based lasing media, compared to the traditional bulk media used in solid-state laser, reduces issues related to over-heating of the cavity and material integrity. The low operating temperature also avoid optical distortions to the output beam due to thermal lensing and birefringence effects in the gain media, which may be produced by temperature gradients in the laser cavity because of the temperature-sensitive nature of the refractive index;
- high beam quality: fiber lasers can operate on the lowest-order transverse mode, leading to excellent output beam quality;

- no strict pump requirements: fiber laser are based on rare-earth ions, which exhibit broad spectral regions with good absorption, making the pump wavelength uncritical and thus enabling the use of high power low beam quality laser diodes for the pumping process.

- high efficiency of operation (up to 80%), due to the high gain efficiency of doped fibers.

Despite the many advantages, fiber lasers also have some limitations, due to the reduced size of the fiber core needed to generate high quality laser beams [27]:

- risk of optical damage: the high power density of fiber lasers may exceed the damage threshold of the fiber material in the small core area;

- nonlinear effects, such as stimulated Raman scattering (SRS), stimulated Brillouin scattering (SBS) and self focusing;

- reduced energy storage in the fiber: even long optic fibers lack the capability to store sufficient energy in the fiber core for the generation of high power laser radiation.

1.6.1 Rare-earth ions

Fiber lasers are based on glass fibers doped with laser-active rare earth ions. Although almost every rare earth ion has been researched for application to fiber laser, only a number are suitable to be employed as dopants in high-power laser system: these are neodymium, erbium, ytterbium, thulium, praseodymium and holmium.

The transition wavelengths of such ions are summarised in Tab. 1.1.

The ytterbium (Yb^{3+}) ion is the most commonly used ion in fiber lasers. The broad absorption spectrum of ytterbium permits wide flexibility in the choice of pump source wavelengths. Moreover, the absorption spectrum pecks

Table 1.1: Common rare-earth ions for fiber laser application [4].

Ion		Common wavelengths [μm]
Neodymium	Nd^{3+}	$1.03 - 1.1$
		$0.9 - 0.95$
		$1.32 - 1.35$
Ytterbium	Yb^{3+}	$1.0 - 1.1$
Erbium	Er^{3+}	0.55
		$1.5 - 1.6$
		2.7
Thulium	Tm^{3+}	$1.7 - 2.1$
		$1.45 - 1.53$
		0.48
		0.8
Praseodymium	Pr^{3+}	1.3
		0.635
		0.6
		0.52
		0.49
Holmium	Ho^{3+}	2.1
		2.9

at $915nm$ and $976nm$, very close to the peak of emission at $1030nm$ (Fig. 1.13). The small quantum defect allows efficient energy conversion from pump radiation to laser output; this also reduces heating in the laser crystal, improving prospects for power scaling. In comparison to ytterbium, both neodymium

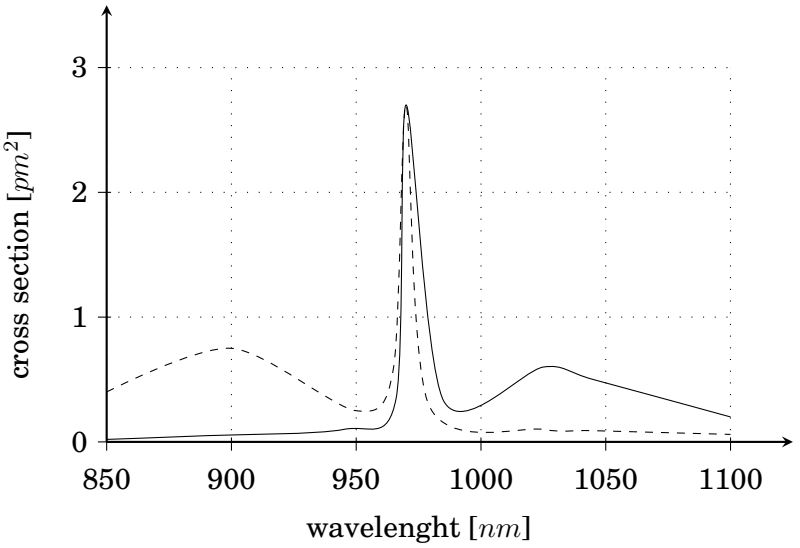

Figure 1.13: Absorption (dashed) and emission (solid) cross sections of Yb^{3+} ions in germanosilicate glass [3].

(Nd^{3+}) and erbium (Er^{3+}) ions have much larger quantum defects, coupled with inferior maximum dope levels into silica fibers. For these reasons, ytterbium is normally preferred in high power laser application, in spite of its quasi-three-level operation scheme, which leads to a higher laser thresholds than that of neodymium.

1.6.2 Doped fiber design

In the simplest case, an optical fiber consists of a transparent core surrounded by a transparent cladding material with a lower index of refraction (Fig. 1.14a). This structure causes the fiber to act as a waveguide, supporting a single propagation mode for a given wavelength (*single mode fiber*). Single mode fiber can generate laser output with diffraction-limited beam quality, but they require to be pumped by radiation with the same high beam quality, which can be generated only by low power pumping source. On the other hand, optical fiber with larger core diameter can support multiple propaga-

tion mode (*multi mode fiber*), thus enabling pumping radiation with lower beam quality to be employed. This is to the detriment of output beam quality, which is generally low. To overcome these issues, high-power fiber laser are normally based on *double-clad doped fiber*. The design of the double-clad optic fiber allows the medium to be pumped by relatively low brightness sources to generate a laser beam with brightness of orders of magnitude higher, effectively acting as brightness converters.

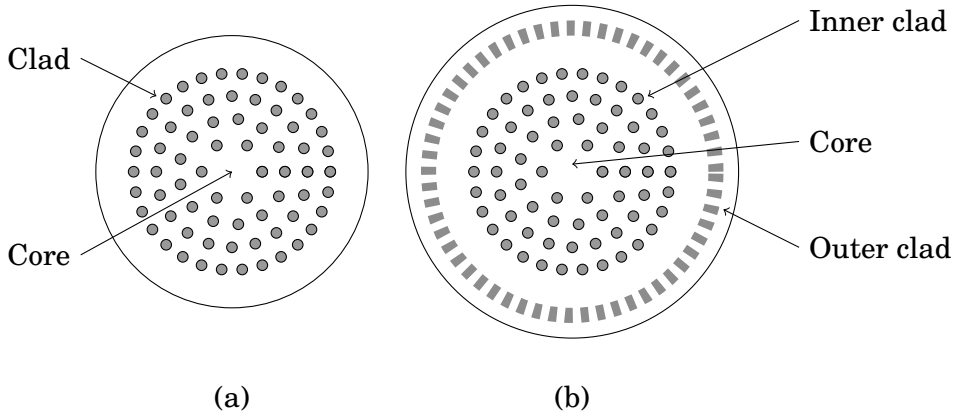

Figure 1.14: Single-clad (a) and double-clad (b) optic fiber.

The laser cavity in fiber lasers is constructed monolithically by welding (*fusion splicing*) different types of fibers, while the optical resonator based on mirrors is replaced by a reflective structures created within the core of the optical fiber, which determines a periodic or aperiodic perturbation of the effective refractive index of the medium (*Fiber Bragg grating*) [28]. When light propagates along the fiber, the refractive index perturbation cause the reflection of radiation in a narrow spectrum of wavelengths, while not affecting the light whose wavelength falls outside this range. For this reason, a fiber Bragg grating effectively acts as a high-reflectivity mirror for the laser light while being transparent to pump radiation.

Chapter 2

Laser material processing

Over the last decades, laser light has found several application in material processing, such as drilling, milling, grooving, welding, cladding and thermal treatments [29]. Laser offers several advantages over other material processing techniques: the ability to focus laser radiation on micron-sized spots enables the production of a wide variety of geometries with reduced Heat Affected Zone (HAZ). Moreover, being a non-contact technique, laser does not suffer from tool wear and no cutting forces are exerted, thus enabling the processing of traditionally hard-to-cut materials.

In particular, the high quality and high energy beam of fiber lasers operating in the nanosecond and femtosecond regimes makes such class of lasers an ideal tool for micromachining application [2].

2.1 Material removal mechanism

2.1.1 Energy transfer

Absorption of light can be explained as the interaction of the electromagnetic radiation with the electrons (either free or bound) of the material.

When light strikes the surface of a material, a portion will be reflected from the interface between the atmosphere and the material due to the dis-

continuity in the index of refraction. The fraction of the incident power that is reflected from the interface is given by the *reflectance coefficient* R. The reflection coefficient R can be calculated from the Fresnel equations

$$R_{\parallel} = \left(\frac{n_1 \cos\theta_i - n_2 \cos\theta_t}{n_1 \cos\theta_i + n_2 \cos\theta_t} \right)^2 \tag{2.1}$$

for light polarised in the incidence plane (Fig. 2.1a) and

$$R_{\perp} = \left(\frac{n_1 \cos\theta_t - n_2 \cos\theta_i}{n_1 \cos\theta_t + n_2 \cos\theta_i} \right)^2 \tag{2.2}$$

for light polarised in the plane perpendicular to the incidence plane (Fig. 2.1b). θ_i represents the angle of incidence of the light and n_1 and n_2 are the the indexes of refraction of atmosphere and of material, respectively.

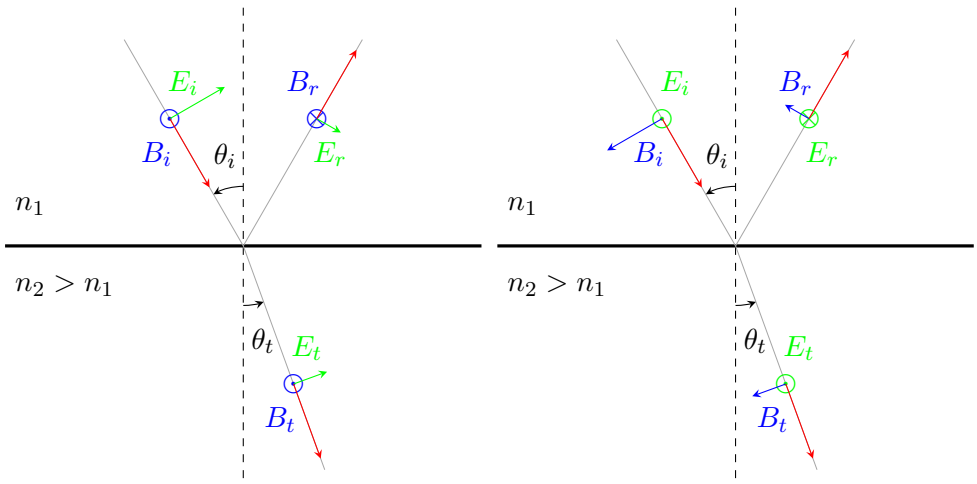

Figure 2.1: Fresnel law schematics for light polarised in the plane of incidence (a) and in a plane perpendicular to the plane of incidence (b).

The reflectivity depends on the wavelength of the incoming light through the relation of the wavelength with the index of refraction of the material. Since generally the reflectivity increases with increasing wavelength, materials are strong absorbers at shorter wavelengths. In addition, the reflectivity

of a surface decreases when the temperature increases. Hence, a material which is strongly reflective at low temperature may become strongly absorbing at high temperature.

During the propagation within the material, the intensity of the transmitted radiation is attenuated according to the Beer-Lambert law:

$$I(z) = I_0(1 - R)e^{\mu z}, \tag{2.3}$$

where $I(z)$ is the intensity at depth z, I_0 is the incident intensity and μ is the absorption coefficient of the material.

The reciprocal of the absorption coefficient $\delta = 1/\mu$ is defined *optical penetration* or *absorption depth* and it represents the depth at which the intensity of the transmitted light drops to $1/e$ of its value at the material-atmosphere interface. Since absorption depths at typical laser wavelengths are in the nanometer range, energy can be concentrated on the surface material without affecting the bulk material.

While the absorption coefficient describes the overall absorption behaviour of a material for a given wavelength, the specific mechanism of absorption depends on the type of material. In general, the incident laser beam excites electrons within the metal to states of higher energy. Such electrons then return to equilibrium, releasing energy to the material lattice (*thermalization*) on a time scale ranging from $10^{-12} - 10^{-10}\,s$ for metals to $10^{-6}\,s$ for non-metals.

When the electron excitation rate is low in comparison to the thermalization rate, the absorbed laser energy can be considered as being directly transformed into heat. Such processes are called *photothermal*. For metals, laser processing with laser pulse length above the nanosecond range is based on photothermal mechanisms. On the other hand, when the material thermalization rate is relatively low, a large amount of energy can accumulate in the intermediary states and directly breaks bonds, without a significant change in the temperature of the material. This non-thermal process is referred to

as *photochemical* and it is typical of irradiation of polymers with short wavelengths and of processing of metals with ultrafast pulsed lasers (femtosecond range).

2.1.2 Thermal laser processing

The generation of heat at the surface and its conduction into the material establishes the temperature distribution in the material.

The temperature profile for a homogeneous material with termo-physical properties independent of temperature heated by a uniform laser beam is described by the following equation (one-dimensional case):

$$\frac{\partial T(z,t)}{\partial t} = \alpha \left(\frac{\partial^2 T(z,t)}{\partial z^2} \right), \tag{2.4}$$

where T is the temperature at depth z and time t and α is the thermal diffusivity of the material.

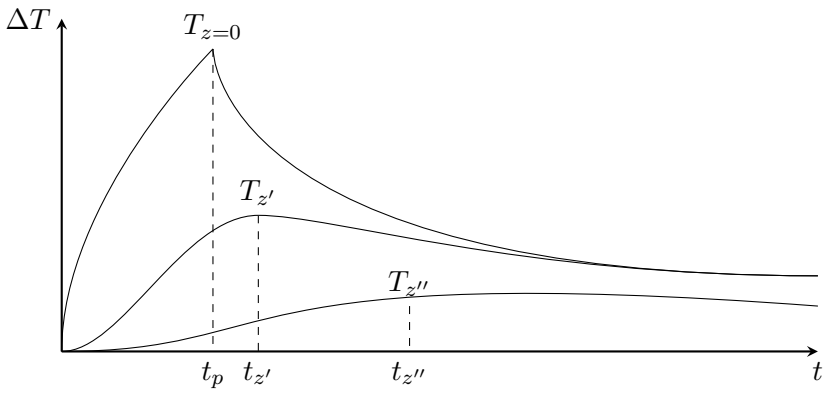

Figure 2.2: Variation of temperature increase as a function of time at various depths $z'' > z' > z_0 = 0$ in the material during laser irradiation [1].

Fig. 2.3 shows typical temperature variations at various depths during pulsed laser irradiation of metals. As one can see, at the surface ($z = 0$) the temperature increases with increasing irradiation time, reaching its maximum value at pulse time t_p. Once the irradiation ends, the surface material

rapidly cools down. Below the surface ($z > 0$), the temperature shows the same behaviour, but the maximum temperature is reached at a longer time $t_{z'} > t_p$. Such delay increases for increasing depths, whereas the maximum value reached by the temperature decreases.

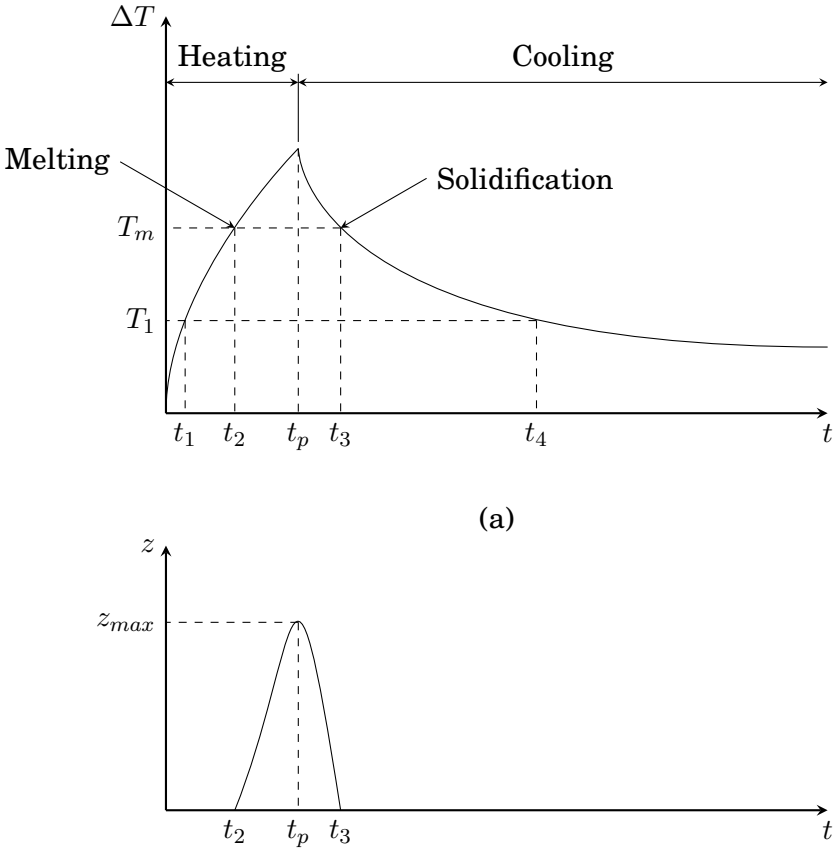

Figure 2.3: Evolution of phase change (a) and depth of the solid-liquid interface (b) in the material as a function of time during laser irradiation [1].

If the incident laser intensity is sufficiently high, the surface temperature can reach the melting or evaporation temperature. The absorption of laser energy can therefore result in phase transformations such as surface melting and evaporation. The corresponding minimum laser intensities are referred

to as melting (I_m) and evaporation (I_v) thresholds. When laser intensity equals I_m, the temperature of the surface ($z = 0$) increases with increasing irradiation time, reaching its maximum value at pulse time t_p and then decreasing. At time t_2, the temperature reaches the melting temperature of the material and the surface material starts to melt (Fig. 2.3a). For time $t > t_2$, the solid-liquid interface progresses within the material, reaching the maximum depth z_{max} (Fig. 2.3b).

At constant pulse time, the maximum depth of melting increases with increasing laser intensity. However, any increase in the intensity will determine a corresponding increase in the the maximum surface temperature: the maximum melting depth is therefore limited by the vaporisation temperature of the material. Further increases in the laser power intensity cause evaporative removal of material from the surface without any further increase in the depth of melting. Any increase in pulse duration causes similar effects. Once vaporization at the surface of the material has started, the irradiation causes the liquid-vapour interface to recess towards the solid bulk, effectively removing the material above the liquid-vapour interface.

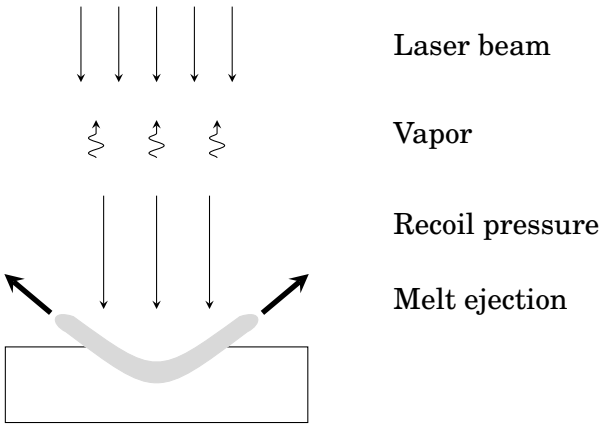

Figure 2.4: Schematic of surface evaporation and melt expulsion due to the recoil pressure during laser-material interaction.

The intensive evaporation of the material surface irradiated by the incident laser beam will induce a recoil momentum, which leads to the surface depression of the molten pool. Under typical materials processing conditions,

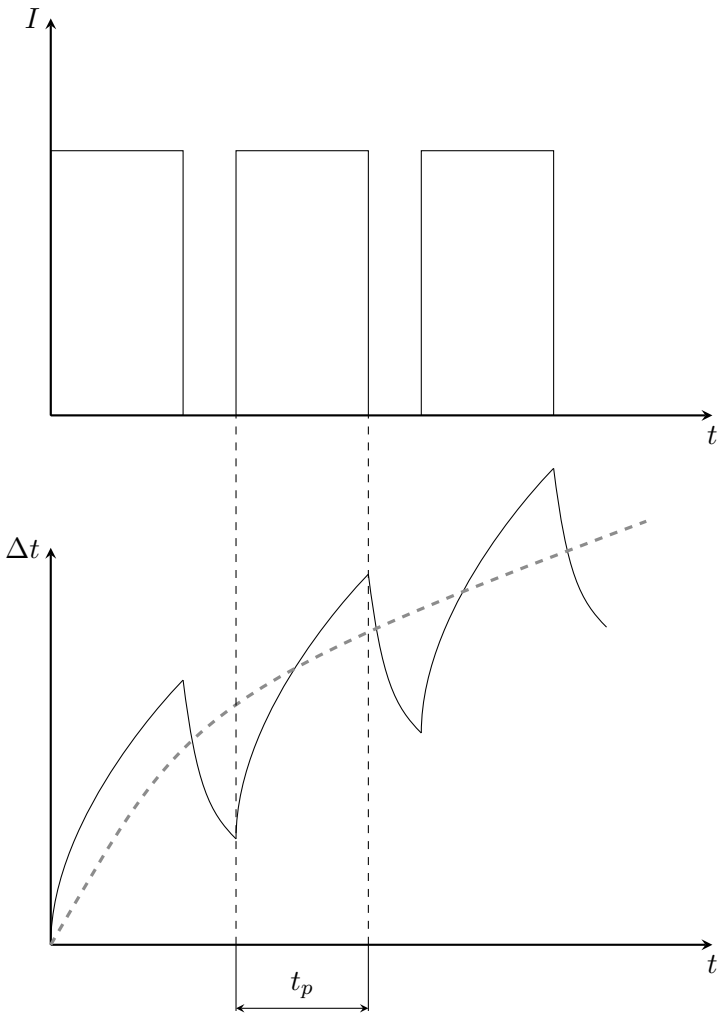

Figure 2.5: Variation of surface temperature as a function of time during multipulse laser irradiation [1].

the recoil pressure is in general sufficiently large to overcome the surface tension and to expel the molten material sideways (Fig. 2.4). The actual material removal process is therefore the combination of vaporisation and melt

ejection.

The discussion above was conducted under the hypothesis of uniform laser irradiation. However, the laser power generally shows more complex distribution, requiring the thermal analysis to be conducted in three dimensions. Moreover, the temperature distribution is influenced by the temporal shape and by the repetition rate of the pulses: the temperature of the material increases during each pulse and decreases during the time between adjacent pulses. Since such time is too short for the material to cool completely, the initial temperature during heating with the subsequent pulses is always higher than that during heating with preceding pulses. This results in temperature fluctuations (heating and cooling) during each pulse and time interval following the pulse (Fig. 2.5).

2.1.3 Photochemical material removal

In photoablation, the energy of the incident photon causes direct breaking of the molecular chains in organic materials. Material removal is obtained by molecular fragmentation, without any significant thermal damage. In order to perform photoablation without thermal damage, the laser radiation needs to be pulsed with pulse length shorter than

$$\tau = \frac{d^2}{4\alpha}, \tag{2.5}$$

where d is absorption depth and α is the thermal diffusivity of the material.

2.1.4 Plasma formation

In general, the vapour generated during the photothermal material removal process interacts with the incoming laser radiation. If the laser intensity reaches the ionisation threshold I_p, vapour breakdown occurs and plasma is formed. The presence of plasma can influence the interaction of laser radiation with the material in different ways. If laser intensity is just above I_p, the

plasma remains confined to the evaporating region during laser irradiation (*plasma coupling*, Fig. 2.6a).

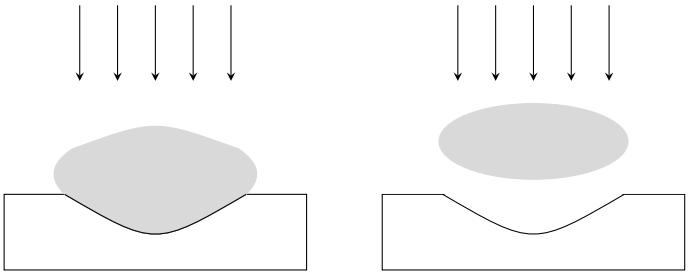

Figure 2.6: Schematic of plasma coupling (a) and plasma shielding (b).

In this case, the plasma presence contributes to the energy transfer from the laser beam to the surface, resulting in a significant increase in the absorptivity of laser radiation by the material. On the other hand, for laser intensity much larger than I_p, the plasma expands away towards the laser beam, losing contact with the evaporing surface and effectively obscuring the laser radiation (*plasma shielding*, Fig. 2.6b).

2.2 Laser beam micromachining

Laser micromachining is extensively used for manufacturing of features with micron and sub-micron resolution on components. A wide range of materials such as metals, ceramics and polymers have been successfully micromachined for microelectronics, MEMS, mechanical and other applications [19, 7].

The domain for different techniques for laser processing of metals as a function of laser power and pulse time is illustrated in Fig. 2.7. In general, the applications of laser to material processing can be grouped into two major categories, based on the energy density that is applied on the surface of the

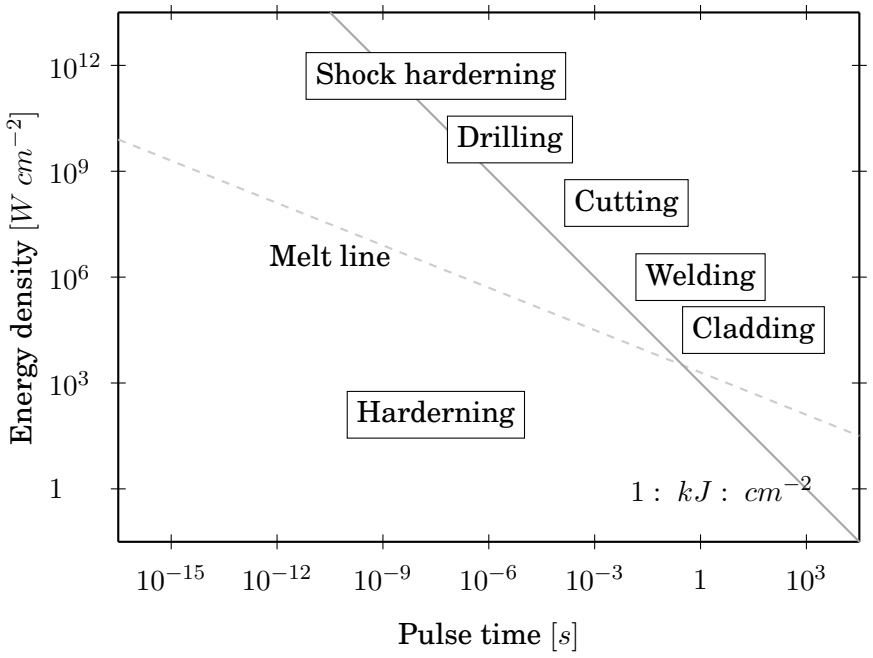

Figure 2.7: Typical laser power density and pulse time for different examples of laser material processing of metals.

material:

- processes causing no significant changes of phase (lower energy density, on the left of the melt line);
- applications inducing phase transformations (higher energy density, on the right of the melt line).

Laser micromachining is a complex dynamic process, which is influenced by numerous parameters. Traditionally, the selection of process parameters that generate the desired micromorphology is performed via a *trial and error* method. Such a technique is non-systematic, time-consuming and it is not guaranteed to output an optimum combination of the process parameters. These limitations can be overcome by means of more systematic studies, which allow for prediction of the interactive effects of the process input

parameters on the process outcome. Several statistical and numerical approaches have been applied in literature to predict and optimize laser micromachining processes, including theoretical modelling, Design of Experiments, Artificial Neural Networks (ANN), Response Surface Methodology (RSM) and Genetic Algorithms.

2.2.1 Microcutting

The laser microcutting process is used to cut thin sheets of material in various application, including medical devices, MEMS and solar panels. Laser microcutting is performing by removing the substrate material by scanning a laser beam over the workpiece surface. The interaction between laser radiation and material results in a strong temperature increase in the spot region, with the creation of a molten pool. If the heat flux absorbed from the laser beam into the material is sufficient, evaporation occurs from the molten state.

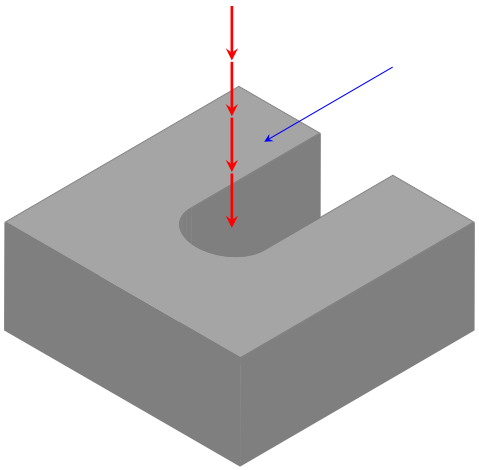

Figure 2.8: Schematic of laser microcutting.

Examples of laser microcutting of micrometric part were reported by Bednarczyk at al. [30]: several shapes were cut with repeatability and accuracy in the micrometer range for both metals and polymers.

Silicon wafer cutting was researched by Dauer et al. [31] for production of micromechanical devices: kerf shape and depth of the cutting edge were found to be strongly influenced by the position of the focal plane. A later investigation on silicon microcutting by Chen and Darling [32] showed that material removal efficiency decreases with increasing laser fluence above a certain value, due to strong plasma shielding effect.

Raval et al. [33] investigated laser microcutting of AISI 316LVM austenitic stainless steel for coronary stent manufacturing. Small kerf width and fine austenitic structure were obtained, even though electrochemical polishing was required to remove surface oxide produced by the laser cutting process.

Baumeister et al. [21] investigated laser microcutting of stainless steel foils using a single mode fiber laser source with the aid of assisting gases such as nitrogen and oxygen. Kerf widths of less than 20 μm were achieved when using oxygen as the assisting gas.

2.2.2 Microdrilling

Laser microdrilling is a technology capable of drilling holes with micron or sub-micron resolution with high flexibility, high processing speed and good accuracy. Laser drilling can be performed by single laser application, by trepanning or by percussion drilling techniques. In trepanning, the focal spot of the laser beam is rotated into a circular path and used to cut out the required area of the workpiece (Fig. 2.9a). This method is suitable for producing larger diameter holes, but it requires precise control of the movement of the laser beam, which may limit the drilling speed. On the other hand, percussion drilling performs material removal through a combination of melting and vaporization induced by a train of high intensity pulses (Fig. 2.9b). The higher speed of percussion drilling makes the latter technique generally favoured over trepanning.

Several investigations have been reported in recent years to study the ef-

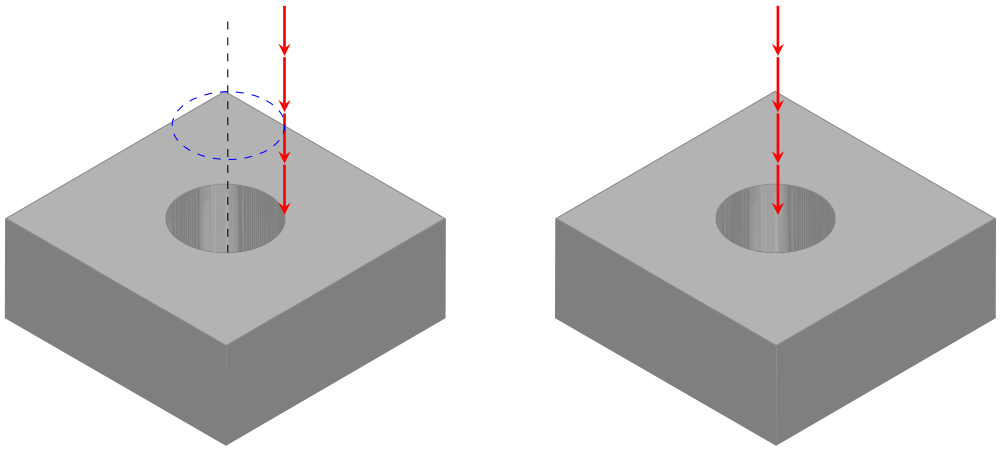

(a) (b)

Figure 2.9: Schematic of laser trepanning (a) and of laser percussion microdrilling (b).

fect of laser characteristics and parameters on geometrical and metallurgical hole quality during laser percussion drilling. Experimental investigations have been carried out by Yilbas et al. [34] to evaluate the effects of single pulse laser drilling parameters on hole characteristics such as recast, taper, barrelling, inlet cone, exit cone, surface debris and mean hole diameter. The experiment considered titanium, nickel and stainless steel, showing how the deviation from the ideal cylindrical morphology of the hole is dependent on the thermal properties of the particular material.

The influence on hole quality during titanium laser drilling of process parameters like pulse energy, pulse repetition rate, pulse duration, focal position, nozzle stand-off and assist gas was investigated by Bandyopadhyay et al. [35]. In this work, it was demonstrated that focal position, pulse energy, and pulse duration are the most significant parameters influencing hole quality. In particular, the lowest level of these parameters among those tested minimises the tapering effect in the geometry of the drilled holes.

Kacara et al. investigated laser drilling of alumina ceramic plates [36]:

the average hole diameters and the average taper angles were examined as a function of the laser pulse duration and the laser intensity. Nedialkov et al. [37] studied the material removal during the laser drilling of AlN ceramics and the resulting thermal damaged area (HAZ), whose diameter was found to increase with increasing laser intensity and frequency.

Laser drilled holes are inherently associated with spatter deposition due to the incomplete expulsion of the ejected material from the drilling site. Part of the ejected material resolidifies, adhering on the material surface around the hole. The effect of process parameters on spatter deposition during laser drilling of Nickel alloy was investigated by Low et al. [38], finding that short pulse widths, lower peak powers and higher pulse frequencies generally result in reduced spatter deposition.

Biffi et al. [20] investigated fiber laser percussion microdrilling of through holes performed on 0.5-mm-thick commercially pure titanium sheets. Pulsed fiber laser was found suitable to efficiently perform high aspect ratio microholes characterised by the presence of spatter in the entrance side only. In the study, the effects of pulse energy and pulse frequency on the resulting micromorphology were evaluated. In particular, the thermally altered zone was found to be limited to a region of the order of 20 μm on the entrance surface.

2.2.3 Microgrooving

The laser grooving process can be used to create blind cut geometries in various manufacturing applications, (assembly slots, micro channel for microfluidic devices, marking).

Chryssolouris [39] developed a theoretical model deriving a relation between groove depth and process parameters under the assumption of complete removal of the molten material, using the heat balance at the cutting front as the governing equation for the process. A similar approach was applied in [40], where the grooving depth was estimated through the for-

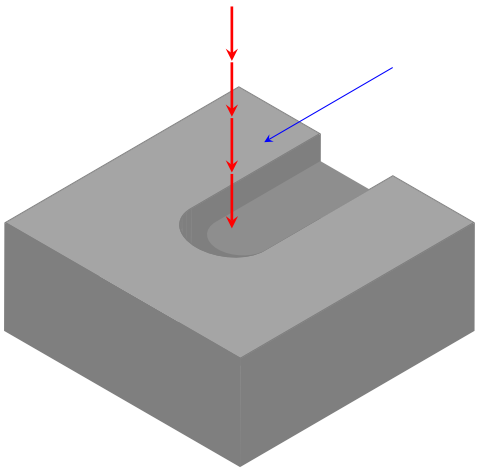

Figure 2.10: Schematic of laser microgrooving.

mulation of the energy equations. Measurements of the laser contours on the workpiece surface showed a close agreement with the theoretical predictions. Later, a theoretical model was developed for simulating the pulsed laser grooving process. The model predicts the maximum groove depth that can be achieved with a specified set of process parameters, such as laser power, pulsing frequency and scanning velocity [41].

Experimental studies on laser grooving of ceramic materials have been reported. Bai et al. [42] carried out laser grooving of alumina plates using a pulsed Nd:YAG laser, with emphasis on the effect of repetition frequency. Dhupal et al. investigated the grooving of both alumina [43] and aluminium titanate [44] to develop regression mathematical models to describe the effects of process parameters on the microgrooving operations. In [45], ANN and RSM has been employed to support modelling and optimization analysis for predicting parameter settings for a pulsed Nd:YAG laser during the microgrooving of Al_2TiO_5. Duphal et al. [46] applied DOE methodology to laser turning of microgroove on aluminium dioxide, combining multi-layered ANN with multi-objective GA optimization to minimise the deviation of the main

geometrical features of microgrooves.

Similar techniques have been applied to the microgrooving of metals [47] and glass [48].

A number of studies of the laser grooving process has been conducted on composite materials as well, both numerically [49] and experimentally [50, 51].

Chapter 3

Design and automation of a pulsed Fiber Laser micromachining system

This chapter is aimed at discussing the design and automation of an experimental setup for performing Fiber Laser micromachining processes. In the following sections, the design principles are discussed and the integration of the selected components is described. Subsequently, the software control system and its architecture are presented.

3.1 Design of the micromachining Fiber Laser system

Typically, a laser micromachining system consists of four main components: a laser source, a setup for part positioning, a system to focalise and deliver the laser beam to the working area and a controller for managing the laser beam emission and synchronising it with the relative motion between laser beam and workpiece.

In general, for any micromachining technique, the ability to generate microfeatures with high dimensional precision depends on two conditions being satisfied: a small *unit removal*, i.e. a small volume of material removed from the workpiece by one cycle of the micromachining process, and high *equipment precision* [5].

In the laser case, a small unit removal may be obtained by employing a low power laser source capable of emitting a high quality laser beam, composed by a train of short pulses with high energy density, coupled with a focusing system with the potential to focus the laser beam to a very small spot size. In this way, high instantaneous power is applied to the workpiece surface for a short time interval, resulting in the removal by melting and vaporisation of a small amount of material around the spot, with little or no disturbance to the bulk material. On the other hand, this is to the detriment of the overall material removal rate, and hence of productivity.

High equipment precision requires the use of a feed motion mechanism with high displacement accuracy and repetitivity. In general, feed motion system for laser micromachining setups are based on two different approaches:

- the use of a part-positioning system to achieve relative motion between the workpiece and a fixed laser spot [52]. This design provides accurate positioning, but it is limited to low scanning speeds due to the machine dynamics. The main advantage of this method is that the laser spot is positioned very accurately in the working area and the energy delivered to the workpiece surface is independent of the beam position, whereas the downside of this approach is in the lower feed rate achievable;

- the use of an active optical system to manipulate the direction of the laser beam, whereas the workpiece is fixed. The laser spot is translated in the horizontal plane by a pair of computer-controlled mirrors, scanning the surface to be machined. Focusing is achieved through a movable lens [53]. This design allows higher scanning speeds than the

part-positioning system, leading to increased productivity. The disadvantage of this method is that the amount of energy delivered to the workpiece depends on the angular deviation of the laser beam from the optical axis.

In this case, the setup is aimed to study and optimisation of laser micromachining processes. Therefore, accuracy requirements prevail on productivity considerations. For this reason, a 10 W infrared pulsed single-mode Fiber Laser is chosen as the laser source. For the feed motion generation, a part positioning system based on a *x-y* table with sub-micron accuracy is employed to translate the workpiece. The laser spot is kept fixed in the *x-y* plane, but it is motorised along the vertical *z* direction to enable automated variation of the focal plan. A schematic of the setup is reported in Fig. 3.1 and Fig. 3.2.

The entire setup is placed on a granite plate to provide vibration isolation and it is completely enclosed within a steel safety cabinet to prevent any reflected laser radiation from escaping the working area during the operation of the system. Microcontrollers for the translation stages and a personal computer serving as process controller and as user interface complete the setup (Fig. 3.3). During the operation of the system, a video feed is sent back to the controller for monitoring the machining process (Fig. 3.4).

3.1.1 Infrared pulsed Fiber Laser source

The laser micromachining system is based on an infrared, pulsed Yb-doped Fiber Laser source (YFLS, LaserPoint). The characteristics of the laser source are summarised in Tab. 3.1.

3.1.2 Laser delivery and focalisation system

The laser beam delivery system consists of an optic fiber, a collimation device and a focusing lens. The laser beam is collimated to a diameter $D_0 =$

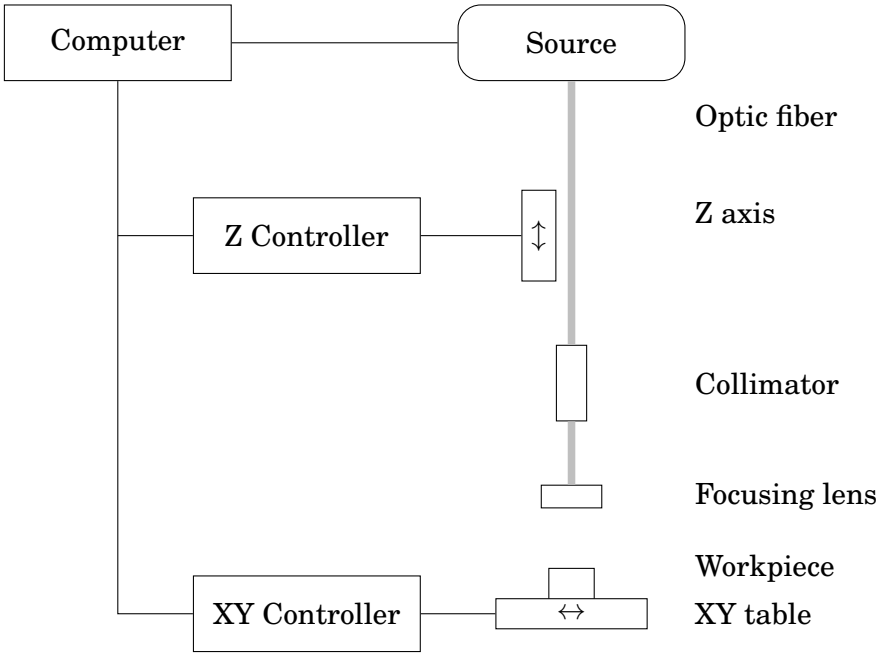

Figure 3.1: Schematic of the infrared pulsed Fiber Laser micromachining setup design.

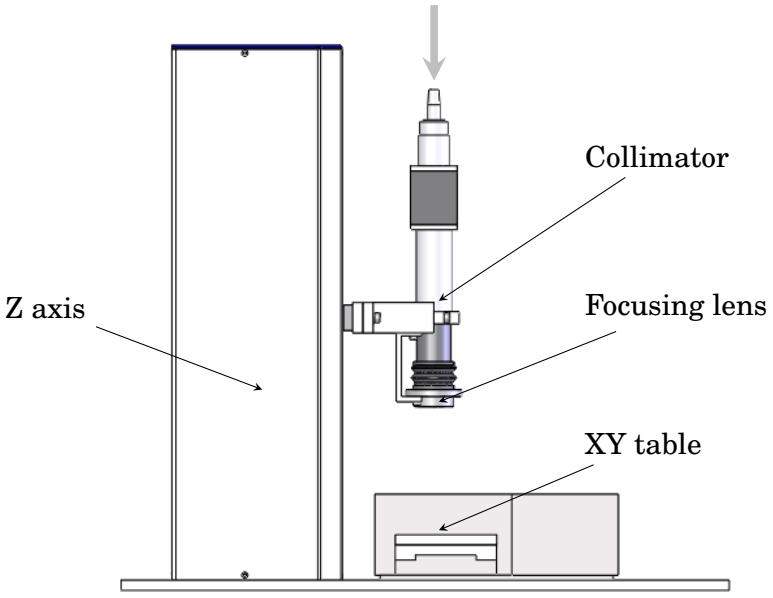

Figure 3.2: CAD rendering of the working area of the infrared pulsed Fiber Laser micromachining system.

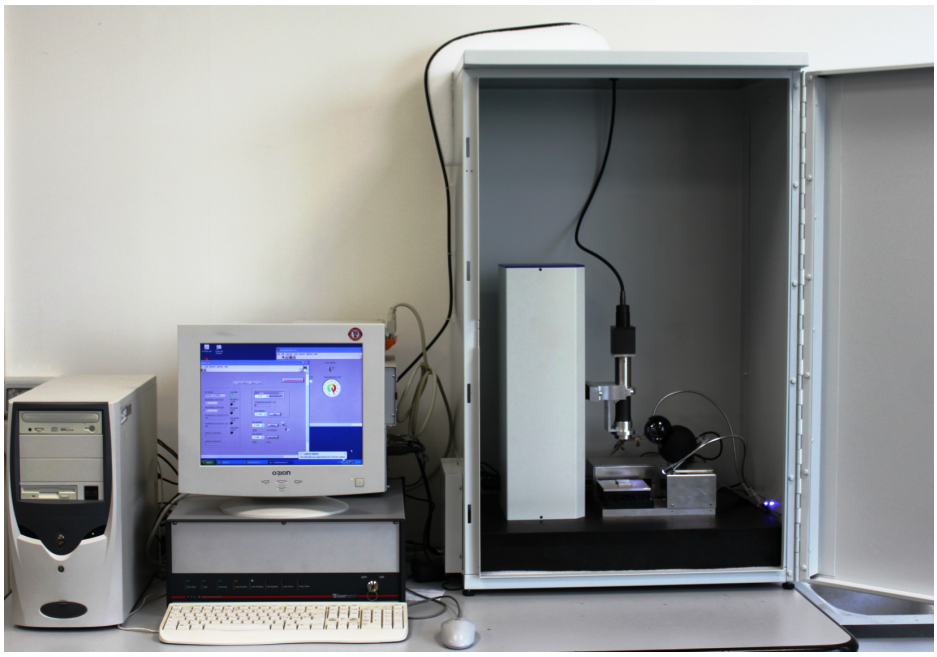

Figure 3.3: Picture of the infrared pulsed Fiber Laser micromachining setup.

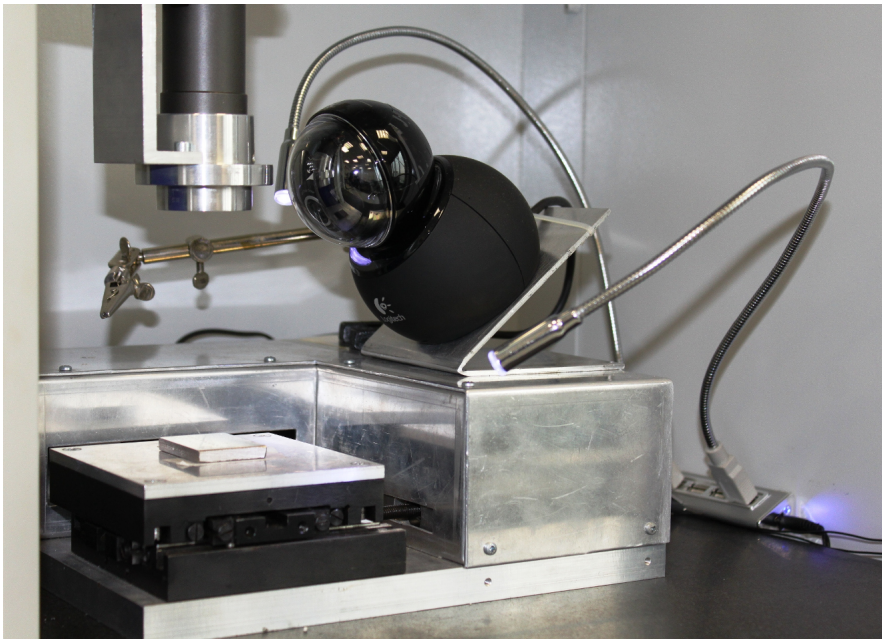

Figure 3.4: Close-up of the workpiece area of the infrared pulsed Fiber Laser micromachining setup.

Table 3.1: Characteristics of the the pulsed Yb-doped Fiber Laser source used in the laser micromachining setup.

Nominal maximum average power (W)	20
Emission wavelength (nm)	1064
Emission linewidth (nm)	< 10
Mode of operation	pulsed
Polarisation	not polarised
Pulse frequency range (kHz)	20-80
Minimum pulse width FWHM (ns)	120
Output power stability (%)	< 5
Beam quality factor, M^2	1.8
Output laser beam diameter (mm)	5.5
Laser beam mode	TEM_{00}

$7\,mm$ and then focused by a F-Theta lens with focal length $f = 100\,mm$. The spot size can be calculated as follows [54]:

$$d_{spot} = \frac{4}{\pi} M^2 \frac{\lambda f}{D_0} = 350\,\mu m. \tag{3.1}$$

The collimation and focusing devices are mounted on a linear translation stage to allow automated positioning of the focal plan. In this way, complex 3D microgeometries can be machined by moving the laser spot along the *z* direction in a coordinated way with the translation of the workpiece. The *z* stage is motorised by a microstepper motor, which can be easily controlled by computer.

The calibration of the stage returned a resolution of 2 μm, with unidirectional repeatability of 0.2 μm. The systematic error due to lost motion in the drive mechanism when changing direction amounts to 480 μm.

3.1.3 Workpiece translation stage

The setup for workpiece translation consists of a *x*-*y* table motorised by a pair of microstepper motors.

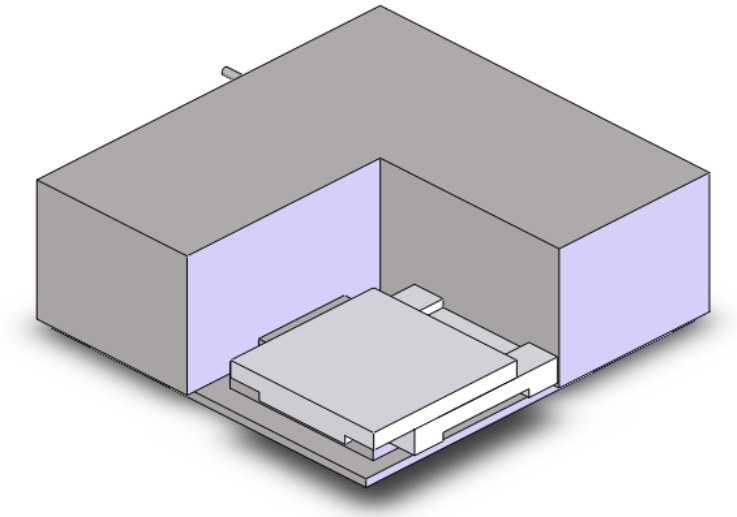

Figure 3.5: CAD renderings of the biaxial translation stage for part positioning in the infrared pulsed Fiber Laser setup.

The x and y stages contain rails on which a carriage is moved back and forth by microstepper motors through a translation screw. The x stage is placed at the bottom on the aluminium support plate, whereas the y stage is placed on top of the x stage carriage. An aluminium plate fixed on top of the y stage carriage hosts the workpiece.

The axes motions are controlled by the computer via a microcontroller (Fig. 3.5). Repetitive positioning accuracy and repetitivity values are reported in Table 3.2 [55].

Table 3.2: Repetitive positioning accuracy for the biaxial workpiece translation stage used in the Fiber Laser micromachining setup.

Property	Values [μm]	
	x axis	y axis
Accuracy	0.15	0.14
Linear repetitivity	0.035	0.039

3.2 Integration of the micromachining Fiber Laser system

The components described in the previous section were assembled and connected to a personal computer serving as process controller. The computer is equipped with a National Instruments NI 6014 board, acting as the interface toward the laser source. The pc board is connected via a 68-pin shielded cable to a connector block, where the electrical connections are wired. Table 3.3 summarises the tension signals used to control the laser emission.

Table 3.3: Communication protocol for the controller - laser interface.

Function	Channel	Signal characteristic
Laser enabling	Ch. 0 (analog)	> 5V
Laser power	Ch. 1 (analog)	0 - 10 V
Laser emission	Ch. 0 (digital, TTL)	1

The communication between the PC and the *x-y* table microcontroller is based on ASCII string commands sent and received through the RS232 interface. The data transfer is based on the following specifications:

- 9600 baud rate;
- 8 data bits per frame;

- 1 stop bit per frame;
- RTS/CTS handshaking.

Two types of message from computer to microcontroller are available:

- *command*, with the most significant bit equal to one and fixed length;
- *value*, with the most significant bit equal to zero and variable length.

If the value length exceeds the single data frame length, the data is split according to the little-endian convention (the least significant value in the sequence is stored first).

The microcontroller reply consists of a sequence of values (if any) followed by the repetition of the received command.

The PC - microcontroller interface for the z stage is based on the same logic.

3.3 Control of the Fiber Laser micromachining system

The control system for the Fiber Laser micromachining setup consists of a software implemented in LabVIEW 7 [56] and run on a personal computer.

3.3.1 The LabVIEW environment

LabVIEW (Laboratory Virtual Instrumentation Engineering Workbench) is a platform and development environment for a visual programming language from National Instruments: it is commonly used for data acquisition, instrument control and industrial automation.

LabVIEW is based on a dataflow programming language, named *G language*: the workflow of a program or subroutine is determined by the structure of the graphical block diagram, which the programmer specifies by con-

necting different function nodes. During execution, the variables are propagates along the connections and nodes are executed as soon as all their input data become available.

LabVIEW programs are called virtual instruments (*VI*) and consist of three different components: a *block diagram*, a *front panel* and a *connector panel*. Controls and indicators on the front panel allow the operator to input data into or extract data from a running virtual instrument. Since the front panel can also serve as a programmatic interface, a virtual instrument can either be run as a program, with the front panel serving as a user interface, or as a subroutine, when used as a node in a new block diagram. In this case, the front panel defines the inputs and outputs for the node through the connector panel.

Since the front and connector panel are essential to the definition of a VI, the user interfaces occupies a central role into the development cycle and a particular care must be taken in its design.

3.3.2 Architecture and user interface of the process controller software

The control system for the laser micromachining setup holds several responsibilities:

- setting the correct value of power to the laser source and controlling the radiation emission;
- setting the correct value of feed rate and controlling the motion of the translation axes;
- managing the synchronisation of the motion of the translation stage with the emission of the laser beam.

These functions are organised into three levels of visual instruments (Fig. 3.6): the lower layer includes the subroutines which perform the basic en-

coding and communication of data to and from the laser source and the axes microcontrollers; the VIs in the middle layer implement the basic functions which the system is required to provide in order to perform any micromachining task; the upper layers consists of higher-level routines capable of carrying out machining task in an automated way.

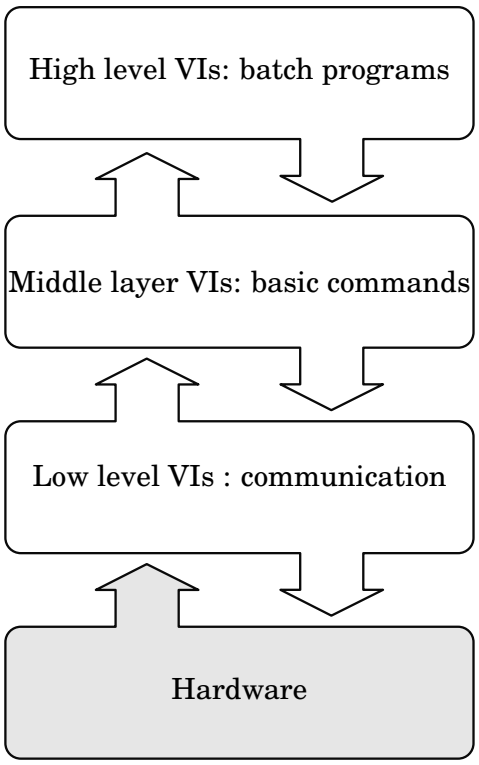

Figure 3.6: Schematic of the architecture of the process controller software.

Low level VIs: communication

The lower layer of the software control system provides the data transfer functions needed for low level communication between the process controller, the laser source and the axes microcontrollers. This requires the definition of visual instruments which implement the communication protocols described

in Section 3.2. These subroutines are essential to the transmission of commands and to the retrieval of data from the hardware components of the system.

The VIs *SendAnalogVolt.vi* and *SendDigitalPulse.vi* are used to send analog tension signals and TTL digital signals to the laser source, respectively.

StringEncoder.vi and *StringDecoder.vi* are responsible for the encoding and decoding of commands and parameters, according to the little-endian coding. The VI *ProcessSerialCommand.vi* handles all the communication through the RS-232 interface, invoking the two VIs described above as and when appropriate.

Middle layer: basic command

The middle layer is composed of visual instruments used to set parameter values, to send commands and to retrieve hardware status and any potential error code. These subroutines represent the building blocks for the visual instruments which constitute the upper layer.

The laser basic functionalities are provided by a number of VIs:

- *SetLaserPower.vi*, to set the value of average laser power;
- *EnableLaser.vi*, to enable the emission of the laser radiation;
- *SwitchLaserEmission.vi*, to switch on and off the emission of the laser beam;
- *SendLaserPulse.vi*, to impose the emission of the laser radiation for a given time interval.

The following VIs are used to control the z translation stage:

- *EnableMotor.vi*, to enable the microstepper motor;
- *GetControllerSwVersion.vi*, to find the version number of the microcontroller software;

- *SetPosition.vi* and *GetPosition.vi*: to set / retrieve the position of the stage;
- *SetVelocity.vi* and *GetVelocity.vi*: to set / retrieve the velocity of the stage;
- *SetRamp.vi* and *GetRamp.vi*: to set / retrieve the length of the acceleration ramp;
- *MoveZAxis.vi*: to impose a movement of the z stage;
- *GetZMovementStatus.vi*: to query whether the stage is moving;
- *GetStatus.vi*: to retrieve the full status of the translation stage, including whether the stage is moving, the status of the limit switches and the status of the thermal protection sensor of the motor.

The VIs used to control the x-y translation system are:

- *EnableController.vi*, to enable the microcontroller and switch on the microstepper motors;
- *ChannelSelector.vi*, to select which axis the following commands refers to;
- *GetAllarmStatus.vi*, to retrieve operator alerts;
- *SetAxisAcceleration.vi* and *GetAxisAcceleration.vi*, to set / get the acceleration value;
- *SetAxisMicroStepSetting.vi* and *GetAxisMicroStepSetting.vi*, to set / get the value of the microstep setting used in the control of the motor;
- *GetMovementStatus.vi*: to query whether the axes are moving;
- *SetAxisPosition.vi* and *GetPosition.vi*: to set / retrieve the position of the stage;

- *GetControllerSwVersion.vi*, to find the version number of the microcontroller software;
- *GetLimitSwitchStatus.vi*, to check the status of the limit switches;
- *MoveAxis.vi*, to move the stage incrementally of a number of steps;
- *MoveAxisToPoint.vi*, to impose an absolute movement to the stage;
- *SetFeedRateForInterpolation.vi*, to set the velocity of both axes in a coordinated way, in order to obtain a synchronous movement of the two axes;
- *SyncroMoveAxis.vi*, to impose a coordinated movement to the two axes, in order to obtain a synchronous motion of the two axes.

Upper layer: batch programs and user interface

The upper layer consists of two collections of VIs: the user interfaces for manual control of the laser micromachining system and the visual instruments for the automatic execution of batch tasks.

The first group comprehends the following VIs:

- *LaserInterface.vi*, which provides the user interface to the laser source, allowing the operator to manually control the emission of the laser beam (Fig. 3.7). The interface is equipped with rocker switches to enable the laser source and to switch on and off the emission of radiation. A slider control and a visual gauge are available to set and check the value of the average laser power.

- *ZAxisInterface.vi*, which represents the user interface for manual control of the z translation stage (Fig. 3.8). The interface shows the current status of the translation stage to the operator and allows the input of acceleration and velocity settings. The operator can move the stage

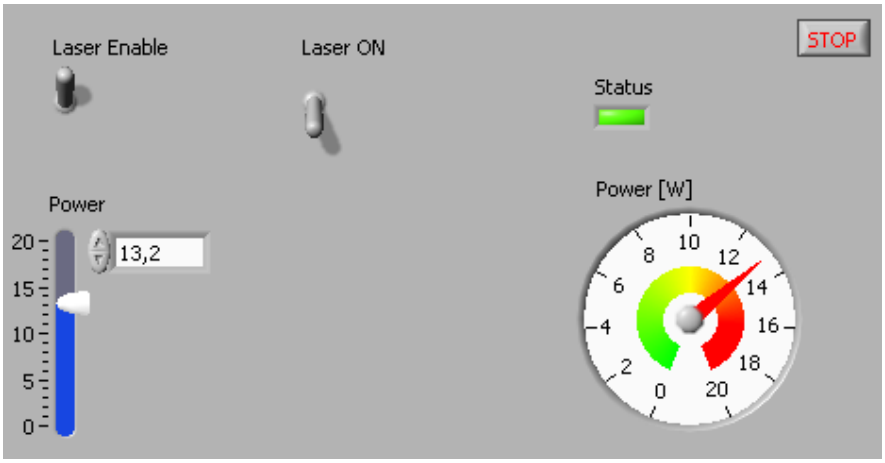

Figure 3.7: User interface for manual control of the laser source (front panel of *LaserInterface.vi*).

manually by pressing the buttons in the central part of the panel or by inputting the exact distance to be covered by the stage;

- *xyTableInterface.vi*, which constitutes the user interface to manually control the *x*-*y* translation table (Fig. 3.9). The left side of the visual instrument hosts a number of indicators which show the current settings and the status of the *x*-*y* table. The motion parameters can be set by inserting the relevant values in the controls located in the upper right corner of the front panel. The operator can then move the the table by the displacement and position controls located in the lower right side of the interface.

The laser micromachining system can be used in automatic batch mode by means of the following VIs:

- *BatchDrilling.vi*, which is used to perform drilling tasks, according to a part program memorised on a text file;
- *BatchCutting.vi*, which is used to carry out cutting and grooving operations, as indicated by a part program.

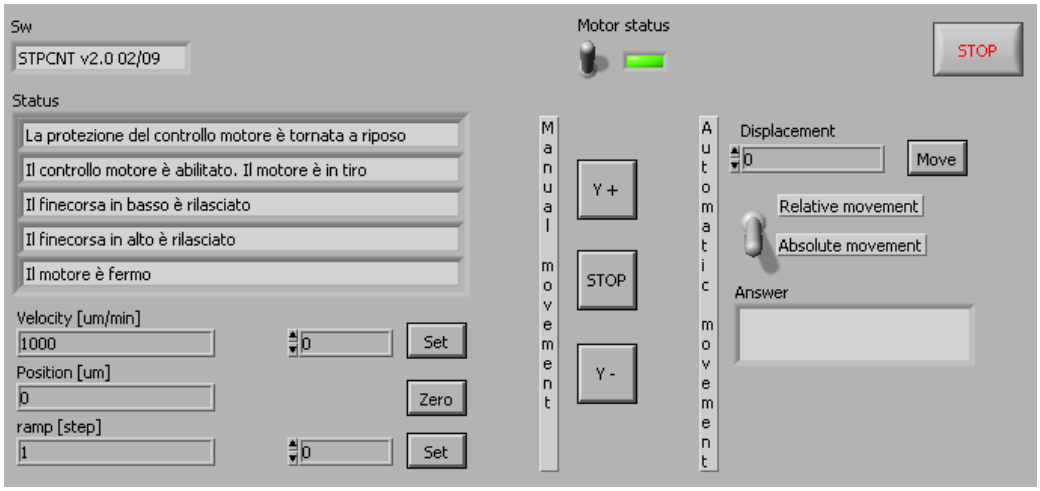

Figure 3.8: User interface for manual control of z translation stage (front panel of *ZAxisInterface.vi*).

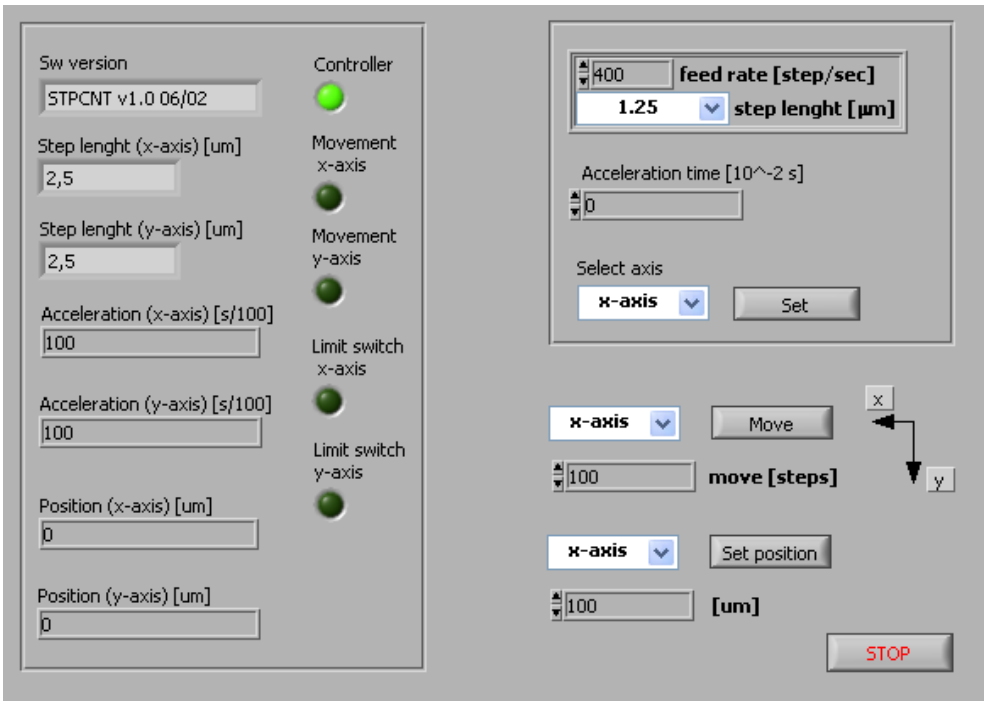

Figure 3.9: User interface for manual control of x-y table (front panel of *xyTableInterface.vi*).

The block diagrams of a number of VIs are reported in Appendix A.

Chapter 4

Planning and programming of laser micromachining processes

As discussed in the previous chapters, laser sources can be tuned in order to generate laser beam with particular characteristics. The irradiation of the surface of components with laser light allows the laser processing of technological materials for several different applications.

In order to perform a particular process on a part, several parameters needs to be defined (*process planning*) and the detailed sequence of operations to be carry out must be precisely planned (*part programming*).

In this chapter, an innovative approach to part programming based on non-structured text in natural language is presented. Before, an introduction to Computer-Aided Process Planning is given, together with the foundations of the stochastic approach to the problem of statistical text processing.

4.1 Laser micromachining process planning

4.1.1 Computer Aided Process Planning

Process planning is defined as “the systematic determination of methods by which a product is to be manufactured, economically and competitively" (American Society of Tool and Manufacturing Engineers). The tasks required by the planning process include the analysis of product/part design data and of shape, size, tolerance, location, orientation and mutual relationship of various geometric features, the selection of the appropriate machining processes, the allocation of the operations in the specific order, the identification of process parameters, the calculation of process times and costs and finally the documentation of the output in terms of process plan and CNC part program. To deliver economy and competitiveness, a process planner has to evaluate alternative process plans, within a limited time frame, and such a task requires manufacturing knowledge and experience.

Therefore, Computer Aided Process Planning (CAPP) has been introduced as a bridge between Computer Aided Design (CAD) and Computer Aided Machining (CAM), to take advantage of the speed and consistency of computers to automate process planning.

As known, the two general approaches to CAPP are the Variant Process Planning (VPP) and the Generative Process Planning (GPP) [57, 58, 59, 60, 61, 62, 63].

VPP relies on Group Technology and on the basic principle that similar parts require similar process plans: it involves classification and coding of new parts in order to retrieve an existing process plan for a similar part in a part database and to vary it to the requirements of a new part. The variant approach can increase the efficiency of the planning operation, but it requires the co-operation of the human planner.

On the other hand, GPP is mainly based on Feature Technology and it

defines new process plans to convert raw materials into the finished part by applying manufacturing rules and decision logic to product design data. Even though the generative approach aims for a full independent generation of the process plan, several issues still remain to be addressed by researchers in this field. At present, a number of systems have been proposed in the literature, but they are still mainly limited to academic discussion. At this time, even the most efficient CAPP systems are still dependent on human input, evaluation and decision.

A large amount of research concentrates on the integration of CAD and CAM modules into the CAPP architecture [64], with particular reference to the problem of information exchange among the different modules. Since a 3D CAD model contains enough information for CNC path programming, the geometric information in the model has been generally considered sufficient for the needs of the integration. For this reason, recognition of features within the CAD model has been the most active topic in the research towards the integration of CAD and CAM since the 1980s [65]. On the other hand, the importance of non-geometric feature information, such as dimensional and geometric tolerances, surface hardness and roughness, and other process specific data, has been somehow disregarded, resulting in even more human intervention required in the CAPP process [66, 67].

The interface between the CAPP/CAM system and the Computer Numerical Control (CNC) machine has long been based on the well known ISO 6983 *G code* language [68]. The ISO 6983 standard represents a weak link in the architecture of a modern integrated CAD/CAPP/CAM system because of several limitations [69]. Namely, it is based on the tool path and machine status description, rather than on the machining tasks with respect to the part. Moreover, it requires fixed-syntax procedural programming and it is practically dependent on proprietary vendor extensions.

Over the years, several new standards for data exchange have been pro-

posed, such as SET, VDA and IGES. Although partially successful, these proposals have failed to meet the needs of the CAD/CAPP/CAM industry [70].

The recent ISO 13303 (STEP) and ISO 14649 (STEP-NC) [71] standards provide a neutral mechanism to describe the entire product data throughout the life cycle of a product, independent of any particular system. STEP-NC is based on the idea of programming the machine operations in terms of manufacturing features, instead of direct coding sequences of axis motions and tool functions as defined in a ISO 6983 part program [72]. Although very promising, a large amount of research is still required for its implementation and no really commercial system has yet been established [73].

4.1.2 Natural language text input for part programming

For the reasons discussed above, even thought a large part of the data can automatically flow along the modules in the process, at present each module of a CAD/CAPP/CAM system for manufacturing of parts by CNC machines requires a certain amount of input from the planner (Fig. 4.1). Such amount of interaction is still performed via specialised interfaces (CAD and CAM software) and through rigid-syntax procedural languages (ISO code, APT code) at the CNC level.

Such a solution is not optimal, since it requires the planner to be familiar with:

- the interface paradigm employed by modern CAD/CAM applications (i.e. to be able to manipulate virtual geometry features and to access relevant command menus);
- the specific internal representation of the particular application (i.e. to be able to organise the solid model in the optimal way);
- part programming in general and with the particular set of commands of the chosen CNC language.

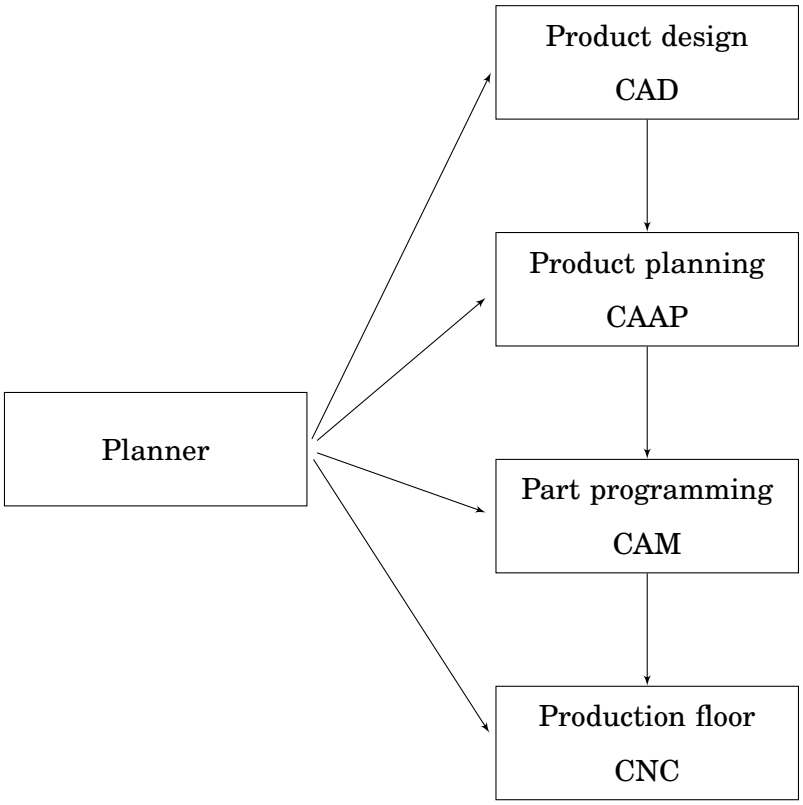

Figure 4.1: Information flow in a CAD/CAPP/CAM system.

The use of a high-level syntax-free language for the input of information to CAD/CAPP/CAM systems has the potential to overcome these issues. According to this approach, the planner/programmer is able to enter data and commands using natural language, i.e. the English language, into a system capable of interpreting the received input and translating it into a specific meta-language, which can be used as an internal representation of the information required for the definition of the design/manufacturing task. The internal details of the task are abstracted away, thus enabling the users to focus on the conceptual issues of problems without the burden of managing the operational details of the input phase.

Using this approach, the planner and programmer face less complication,

since they still need to:

- be familiar with the task of entering sequences of instructions, but they do not need to be concerned with the details of a specific syntax, or structured procedural language, or user interface;
- be able to recognise the meaning of instructions in the particular context, but they do not need to be able to generate these instructions on their own;
- know what sorts of functions are available in the system, but they do not need to know their exact names and locations.

A similar approach was applied in [74] to automatically elaborate assembly process sheets written in a chosen subset of the English language for the automotive industry. Similarly, Shi et al. [75] investigated how to apply natural language understanding to 3D reconstruction from process sheets.

In the following sections, an approach for the use of natural language for the generation of part programs for pulsed Fiber Laser micromachining is proposed. Traditionally, according to ISO G code, part program is an ordered list of program blocks in an ASCII formatted computer file. Every block identifies a machine operation and defines its parameters, following a predefined syntax. Under the new approach, such a file is replaced with almost free syntax, non procedural sentence commands, expressed in natural language, without any particular syntax constraints.

4.2 Stochastic models

Stochastic models describe the evolution of systems that are characterised by inherent randomness or operate in an unpredictable environment. Instead of predicting how the process might evolve over time on the base of deterministic rules or equations, a stochastic model allows random variations in its

inputs to occur over time, as described by probability distributions [76].

A stochastic model Λ can be expressed by a family of probability distributions $P(\theta)$:

$$\Lambda = \{P(\theta) | \theta \in \Theta\}, \tag{4.1}$$

where θ is a parameter vector in the parameter space Θ, which models the evolution of the system over time. $P(\theta)$ represents the joint probability distribution over all the random variables $\{X(t),\ t \in \mathbb{Z}_+\}$ which describe the entities to be modelled.

The joint probability can be factored as a product of conditional probabilities: since each variable can potentially depend on every other variable, the joint probability distribution may require a number of parameters that grows exponentially with the number of random variables in the model. For this reason, in order to maintain the complexity affordable, it becomes necessary to make assumptions of independence between variables.

4.2.1 The Markov property

A great potential for simplification is available when there is the need of modelling discrete processes in which the future evolution of the system depends only on the actual state (or last n states) of the system itself and it is independent of older conditions (*Markov property*):

$$P(X_{t+1} \in U | X_0, X_1, \ldots, X_t) = P(X_{t+1} \in U | X_t, X_{t-1}, \ldots, X_{t-n}), \tag{4.2}$$

where U is a discrete uniform distribution and $n < t$.

A sequence X_t of random variables indexed by discrete time t which satisfies the Markov condition is said to form a *Markov chain* of order n.

For $n = 0$, considering a sequence S of N distinct states, $S = s_1, s_2, \ldots, s_N$ and assuming that the probability of going from a states to another does not depend on time (*stationarity property*), Eq. (4.2) can be rewritten as

$$P(X_{t+1} = s_j | X_t, X_{t-1}, \ldots, X_{t-n}) = P(X_{t+1} = s_j | X_t = s_i). \tag{4.3}$$

If the state space has finite dimension N, the conditional probabilities describing the transitions between the states can be combined into a matrix of *state transition probabilities*:

$$A = \{a_{ij}\} = \left[P\left(X_{t+1} = s_j | X_t = s_i\right)\right]_{N \times N} \qquad 1 \leq i,j \leq N, \tag{4.4}$$

with

$$\begin{aligned} & a_{ij} > 0, \\ & \sum_{i=1}^{N} a_{ij} = 1. \end{aligned} \tag{4.5}$$

Similarly, the initial state of the system is described by a vector of *start probabilities*:

$$\Pi = \{\pi_i\} = P\left(X_0 = s_i\right) \qquad 1 \leq i \leq N, \tag{4.6}$$

where

$$\begin{aligned} & \pi_i > 0, \\ & \sum_{i=1}^{N} \pi_i = 1. \end{aligned} \tag{4.7}$$

Together, the transition probability table A and the start probability vector Π fully describe a first-order observable Markov Model, where the output of the process is a set of states, corresponding to physical (observable) events at each time instant. Such class of stochastic models are generally represented as graphs whose nodes represent the state space and whose edges represent the transition probabilities (Fig. 4.2).

4.2.2 Hidden Markov Models

As previously discussed, each state of a discrete observable Markov model corresponds to an observable event: if the event is not visible, the model is called a *Hidden Markov Model (HMM)* [77]. Such behaviour can be described by a doubly embedded stochastic process (Fig. 4.3): the first layer consists of

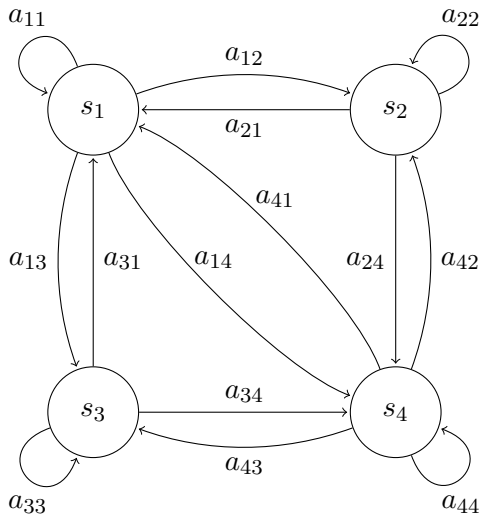

Figure 4.2: A discrete Markov chain (4 states) with state transitions.

a discrete, stationary stochastic process with a finite state space (first-order Markov chain); in the second stage, at every time t an output or emission is generated according to a new probability distribution.

Formally, a Hidden Markov Model is a bivariate discrete time process $\{X_t, Y_t,\ t \in \mathbb{Z}_+\}$, where X_t is a Markov chain as discussed above and Y_t is a sequence of independent random variables such that the conditional distribution of Y_t only depends on X_t.

Assuming that the independent random variables Y_t can generate a set of M distinct events $V = \{v_1, v_2, \ldots, v_M\}$, the emission probability distribution can be represented by a matrix B such that:

$$B = \{b_{ik}\} = \{P(Y_t = v_k | X_t = s_i)\}_{N \times M} \qquad 1 \leq i \leq N,\ 1 \leq k \leq M, \tag{4.8}$$

where the emission coefficient b_{ik} defines the probability of observing the event v_k when the process is in the state s_i.

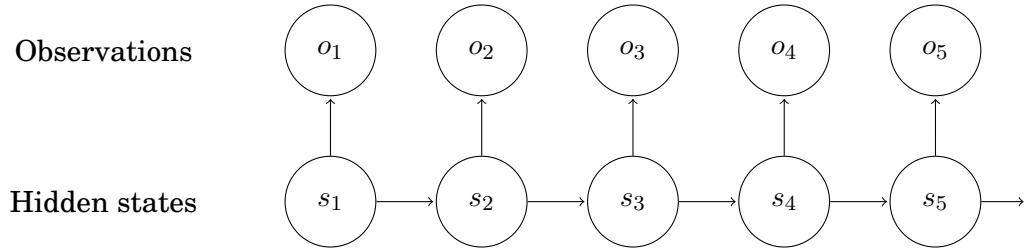

Figure 4.3: Schematic of the layers of a Hidden Markov Model.

As before, the standard stochastic constraints must be satisfied:

$$\begin{aligned} & b_{ik} > 0, \\ & \sum_{k=1}^{M} b_{ik} = 1. \end{aligned} \tag{4.9}$$

To summarise, a HMM of first order is completely described by:

- a finite set of N states $S = \{s_1, s_2, \ldots, s_N\}$;
- a finite set of M observation symbols $V = \{v_1, v_2, \ldots, v_M\}$;
- a matrix of transition probabilities A, defining the probability distribution which governs the transition from one state to another:

$$A = \{a_{ij}\} = \left[P\left(s_j(t+1)|s_i(t)\right)\right]_{N\times N} \quad 1 \leq i,j \leq N; \tag{4.10}$$

- a vector of start probabilities Π, representing the probability that a state s_i is the initial state of the sequence of hidden states:

$$\Pi = \{\pi_i\} = P\left(s_i(t)|t=1\right) \quad 1 \leq i \leq N; \tag{4.11}$$

- a matrix of emission probabilities B, defining the probability distribution which governs the emission of observations from hidden states:

$$B = \{b_{ik}\} = \{P(v_k(t)|s_i(t))\}_{N\times M} \quad 1 \leq i \leq N,\ 1 \leq k \leq M \tag{4.12}$$

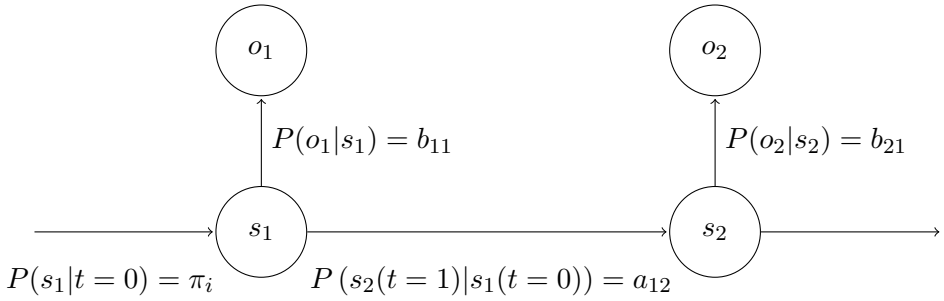

Figure 4.4: Probability distributions in Hidden Markov Models.

where the conditions expressed by Eq. (4.5), (4.7) and (4.9) are satisfied. A similar HMM can be denoted by

$$\lambda = \langle A, B, \Pi, S, V \rangle \,. \tag{4.13}$$

4.2.3 Evaluation of Hidden Markov Models

The joint probability of observing a sequence $O = \{o_1, o_2, \ldots, o_T\}$ generated by a sequence of states $S = \{s_1, s_2, \ldots, s_T\}$ in the HMM λ can be expressed as:

$$P\left(O, S|\lambda\right) = P\left(O|S, \lambda\right)\ P\left(S|\lambda\right), \tag{4.14}$$

where

$$P\left(O|S, \lambda\right) = \prod_{t=1}^{T} P\left(o_t|s_{i_t}, \lambda\right) = \prod_{t=1}^{T} b_{i_t}\left(o_t\right) \tag{4.15}$$

and

$$P\left(S|\lambda\right) = \pi_{s_1} b_{i_1}\left(o_1\right) \prod_{t=2}^{T} a_{s_{i_{t-1}}, s_{i_t}} b_{i_t}\left(o_t\right). \tag{4.16}$$

By combining Eq. (4.15) and Eq. (4.16) into Eq. (4.14), the probability for the observation sequence O to be generated by the given model λ along the state sequence S can be calculated as:

$$P\left(O, S|\lambda\right) = \pi_{s_1} \prod_{t=1}^{T} a_{s_{t-1}, s_t} b_{s_t}\left(o_t\right). \tag{4.17}$$

Eq. (4.17) expresses the probability of generating the observation sequence O from the state sequence S. However, the same sequence O can be generated along any arbitrary sequence of states. Therefore, the overall probability of observing the sequence O must be evaluated over any possible state path:

$$P(O|\lambda) = \sum_S P(O, S|\lambda) = \sum_S P(O|S, \lambda)\, P(S|\lambda)\,. \tag{4.18}$$

The number of possible paths grows exponentially with the length of the sequence, making Eq. (4.18) useless in practical application.

However, by taking advantage of the Markov property, it is possible to develop dynamic programming algorithm to compute the probability of observing O given all the possible paths (*forward algorithm* and *backward algorithm*) or to find the most probable sequence of states S^* that generates a sequence O (*Viterbi algorithm*).

Forward algorithm

As discussed before, because of the Markov property, the probability of a transition to a state is dependent on the previous state only. This property can be used to simplify the calculation of the probability of observing a sequence O: in fact, at time $t+1$ it is sufficient to consider only the N possible states at time t. Thus the calculation can be carried out along the time axis in parallel for all model states.

The *forward variable* $\alpha_t(i)$ represents the probability that the first part of the observation sequence up to o_t is emitted by hidden state sequences which end with the state s_i:

$$\alpha_i(t) = P(o_1, o_2, \ldots, o_t, s_i(t)|\lambda)\,. \tag{4.19}$$

A recursive procedure for the calculation of the probability of the entire sequence can be formulated based on this quantity. For the initiation of the

computation the forward variable value at time $t+1$ is determined as:

$$\alpha_i(1) = \pi_i b_i(o_1) \qquad 1 \le i \le N. \tag{4.20}$$

The calculation then proceeds according to the induction principle. It is therefore sufficient to specify a rule to compute the quantity $\alpha_j(t)$ from $\alpha_i(t-1)$.

The probability of the observation element o_t must consider all the possible partial paths to that element, so it is obtained as the sum of $\alpha_i(t)$ over all the possible predecessor states:

$$\alpha_j(t) = \left[\sum_{i=1}^{N} \alpha_i(t-1)\, a_{ij}\right] b_j(o_t) \qquad 2 \le t \le T, 1 \le j \le N. \tag{4.21}$$

At time T, a set of N probabilities for the observation sequence O and final state $s_i(T)$ are obtained. The overall probability of the sequence O is therefore:

$$P(O|\lambda) = \sum_{i=1}^{N} \alpha_i(T). \tag{4.22}$$

The procedure described above is not the only possible one. The inclusion of all the possible paths in the calculation of the probability can be replaced with an arbitrary *optimal probability*, depending on the particular problem. A common choice is the probability calculated by maximisation over all the individual probabilities, as given by the expression:

$$P^*(O|\lambda) = P(O, s^*|\lambda) = \max_s P(O, s|\lambda). \tag{4.23}$$

The forward variable is therefore replaced with:

$$\delta_i(t) = \max_{s_1,\ldots,s_{t-1}} P(o_1, o_2, \ldots o_t, s_1, s_2, \ldots, s_i(t)|\lambda) \qquad 1 \le i \le N \tag{4.24}$$

and the recursion scheme takes the form:

$$\delta_i(1) = \pi_i b_i(o_1), \tag{4.25}$$

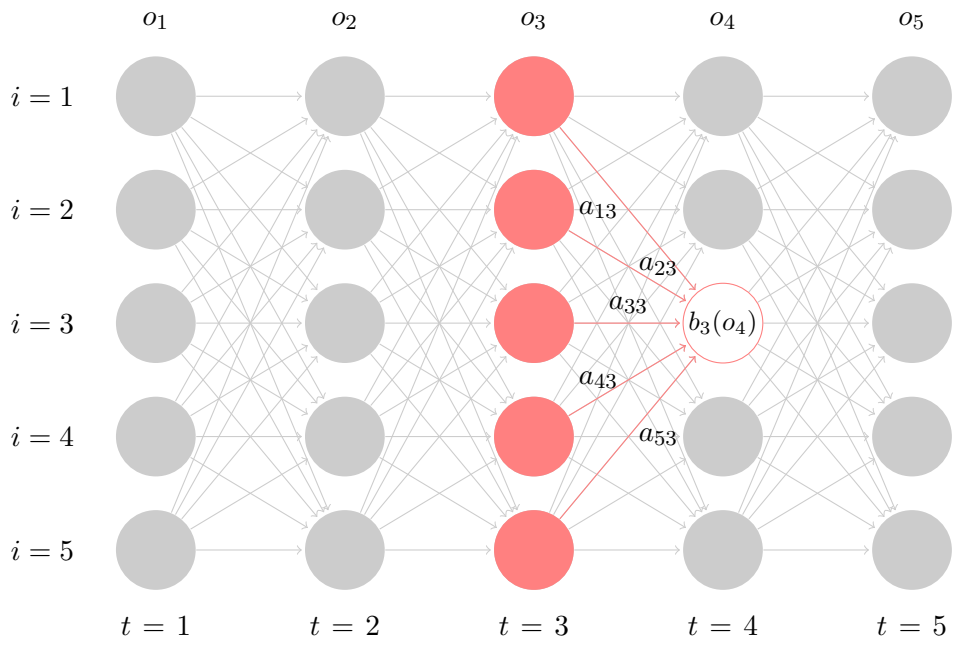

Figure 4.5: Schematic of the *forward* algorithm: probabilities to be evaluated on computing $\alpha_3(t = 4)$.

$$\delta_j(t) = \max_i \left[\delta_i(t-1)\, a_{ij}\right] b_j(o(t)) \qquad 2 \leq t \leq T, 1 \leq j \leq N. \tag{4.26}$$

The optimum probability for the observation sequence O is then obtained as the maximum over all the optimal possible states $s_i(T)$

$$P^*(O|\lambda) = P(O, s^*|\lambda) = \max_i \delta_i(T). \tag{4.27}$$

Backward algorithm

In a similar manner, the probability of an observation sequence O can be calculated by defining a symmetrical backward variable $\beta_i(t)$ as the conditional probability for the partial observation sequence from $o(t+1)$ to the end of being generated by all the state sequences starting at the state s_i:

$$\beta_i(t) = P(o_{t+1}, o_{t+2}, \ldots, o_T, s_i(t)|\lambda.). \tag{4.28}$$

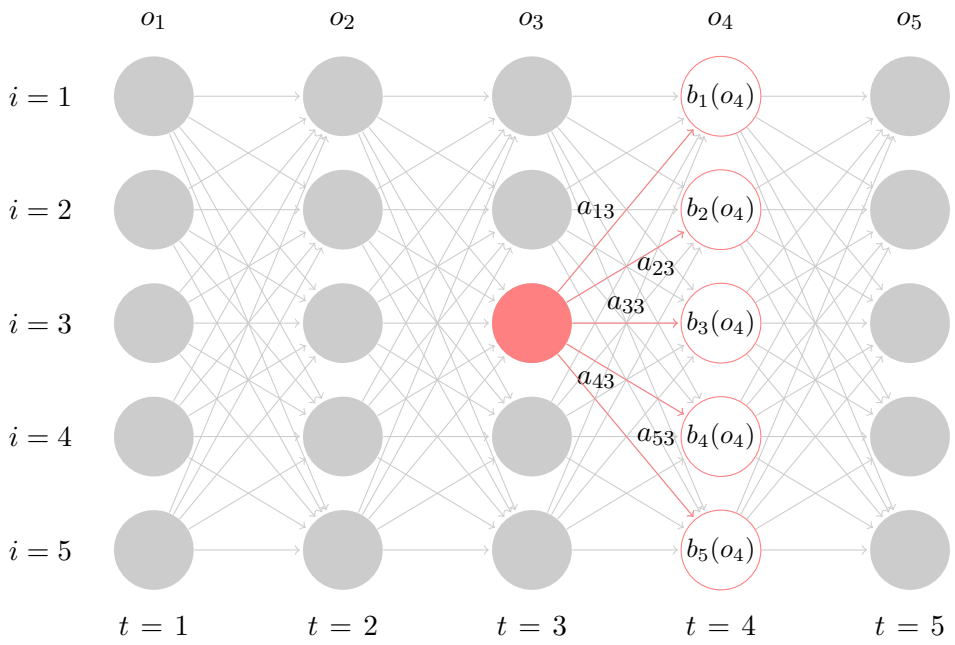

Figure 4.6: Schematic of the *backward* algorithm: probabilities to be evaluated on computing $\beta_3(t = 3)$.

The calculation then proceeds according to the induction principle, as summarised by the following expressions.

1. Initialisation

$$\beta_i(T) = 1 \quad 1 \leq i \leq N. \tag{4.29}$$

2. Recursion

$$\beta_i(t) = \sum_{j=1}^{N} \beta_j(t+1) a_{ij} b_j(o_{t+1}) \quad 1 \leq t \leq T-1, 1 \leq i \leq N. \tag{4.30}$$

3. Termination

$$P(O|\lambda) = \sum_{i=1}^{N} \beta_i(1) \pi_i b_i(o_1). \tag{4.31}$$

Either the forward or the backward algorithm can be used to compute the probability of a sequence of observation events O.

4.2.4 Decoding of Hidden Markov Models

A different problem is how to find the optimal hidden state sequence S^* for a given observation sequence O.

$$S^* = \underset{S}{\operatorname{argmax}} P\left(S|O, \lambda\right) \tag{4.32}$$

As before, the brute force approach is not useful: after enumerating all the possible state sequences of length T, the state sequence with the maximum probability is chosen, with a complexity $O\left(TN^T\right)$.

Viterbi algorithm

The Viterbi algorithm is an efficient way of computing the optimal state sequence using a recursive procedure based as above on the Markov property [77].

The probability of a partial optimal path $Q_{S^*}(t)$, which generates the initial segment of the sequence O up to o_t with the maximum probability and which ends in state s_i, is:

$$\delta_j\left(t\right) = \max_i \left[\delta_i\left(t-1\right) a_{ij}\right] b_j\left(o_t\right). \tag{4.33}$$

Since the maximisation is performed at every time step t, every decision in the computation of $\delta_i(t)$ is only locally optimal. The globally optimal probability of the optimal state sequence is unknown until the evaluation of the sequence on its complete length. At that point, only the last state that maximises the sequence probability is known. The remaining elements of the hidden sequence need to be determined based on the decisions made during the computation of the previous $\delta_i(t)$ values.

Defining with $\delta_j(t+1)$ the probability of the most probable path ending in state s_j at time $t+1$ and with $\psi_j(t+1)$ the index of the state s_i from which the best path leading to s_j comes, the algorithm is defined as follows.

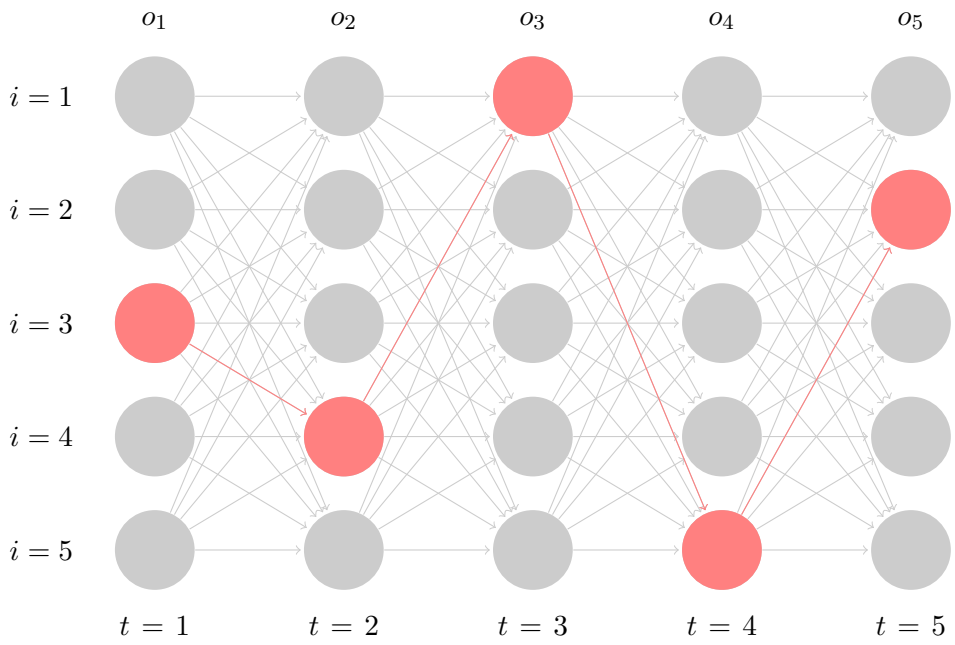

Figure 4.7: Trellis diagram showing the optimal state sequence at $t = 5$ for a HMM with 5 states.

1. Initialisation

$$\delta_i(1) = \pi_i b_i(o_1) \qquad 1 \leq i \leq N, \tag{4.34}$$

$$\psi_i(1) = 0. \tag{4.35}$$

2. Recursion

$$\delta_j(t) = \max_{1 \leq i \leq N} \left[\delta_i(t-1) a_{ij}\right] b_j(o_t) \qquad 2 \leq t \leq T, 1 \leq j \leq N, \tag{4.36}$$

$$\psi_j(t) = \operatorname*{argmax}_{1 \leq i \leq N} \left[\delta_i(t-1) a_{ij}\right] \qquad 2 \leq t \leq T, 1 \leq j \leq N. \tag{4.37}$$

3. Termination

$$P(S^*) = \max_{1 \leq i \leq N} \left[\delta_i(T)\right], \tag{4.38}$$

$$Q_{S^*}(T) = \operatorname*{argmax}_{1 \leq i \leq N} \left[\delta_i(T)\right]. \tag{4.39}$$

4. Backtracking

$$Q_{S^*}(t) = \psi_{Q_{S^*}{}_{t+1}}(t+1)\,. \tag{4.40}$$

4.2.5 Estimation of Hidden Markov Models

In order to setup a Hidden Markov Model, the transition probability and emission probability distributions need to be estimated.

Starting from a set of examples, the Maximum Likelihood Estimation (MLE) for the transition probability distribution can be obtained by evaluating the expression

$$a_{ij} = P(s_j|s_i) = \frac{C(s_i \to s_j)}{\sum_{j'}\left(s_i \to s'_j\right)}. \tag{4.41}$$

Similarly, the emission probability distribution can be estimates using the expression

$$b_{ik} = P(o_k|s_i) = \frac{C(s_i \to o_k)}{\sum_{k'}\left(s_i \to o'_k\right)}. \tag{4.42}$$

This approach is practical but it suffers from a main drawback: if no emission from a particular state appears in the training set, its emission probability distribution remains uncertain at the end of the estimation process. The issue can be overcome by adding fixed quantities to the MLE values; this, however, is far from ideal since the resulting probability distributions are slightly biased.

The *Baum-Welch algorithm* provides a more robust solution the the parameter estimation problem for HMMs. Such algorithm is based on the expectation - maximisation method: at first it assigns initial values to the parameters, by random or informed guess. Then, the probabilities of the parameters are adjusted at every iteration in order to increase the probabilities that the model assigns to the training set, until the method converges to a local maximum. An in-depth discussion of such technique can be found in [78].

4.3 Statistical modelling of part programming for laser micromachining

Formally, the problem of natural language understanding in order to program a laser micromachining process (Section 4.1.2) can be stated as follows: given an input sentence n composed of a sequence of words and numbers in a natural language N, i.e. the English language, the machine controller is required to automatically extract the information from the input sentence to produce an output sentence o in a meta-language O, specific to the machine job description context. Such an operation is defined as a *linguistic translation* and requires the development of a transducer capable of understanding instructions in a syntax-free natural languages [79].

4.3.1 The Noisy Channel model

The Noisy Channel model [80] is a probabilistic model widely used in virtual any field of Natural Language Processing (Part-of-Speech tagging, Machine Translation, Spell Checking, etc.) [81]. The model can be employed whenever a received signal does not uniquely identify the message being sent: it assumes that random noise has affected the message X transmitted by the sender to the receiver, modifying it into Y, as shown in Fig. 4.8.

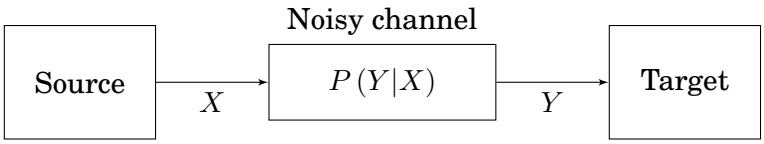

Figure 4.8: The Noisy Channel model.

Following this approach, we think of sources and target backwards: a noisy channel is setup to receive the O (input) sentence o, which is then corrupted by the process to produce an N (output) sentence n. A decoder is em-

ployed to recover the original sentence according to its probability [82] (Fig. 4.9).

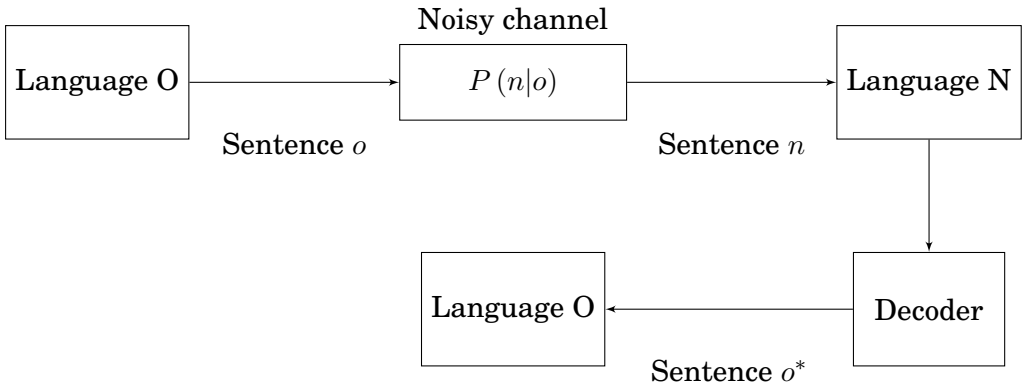

Figure 4.9: The Statistical Machine translation process.

In a probabilistic model, the best O sentence o^* is the one whose probability $P(n|o)$ is the highest among all the possible O sentences o:

$$o^* = \underset{o}{\operatorname{argmax}} P(o|n). \tag{4.43}$$

The expression above can be rewritten according to the Baynes rule, obtaining:

$$o^* = \underset{o}{\operatorname{argmax}} P(o|n) = \underset{o}{\operatorname{argmax}} \frac{P(o)\,P(n|o)}{P(n)}. \tag{4.44}$$

Since the probability of the input sentence n is a constant in the decoding problem, the denominator $P(n)$ can be omitted in the $argmax$ evaluation.

The resulting Noisy Channel equation shows the need for two distinct probabilistic models: a *language model* $P(o)$, to maximise “fluency" of the output, and a *translation model* $P(o|n)$ to incorporate “faithfulness" in the decoding process (Fig 4.10).

$$o^* = \underbrace{\operatorname{argmax}}_{\text{decoder}} \quad \underbrace{P(o)}_{\text{language model}} \quad \underbrace{P(n|o)}_{\text{translation model}} \tag{4.45}$$

Thus, the Noisy Channel model requires three components to be defined:

- a language model to compute $P(o)$;
- a translation model to compute $P(n|o)$;
- a decoder to retrieve the sequence o^* with the maximum probability, given n.

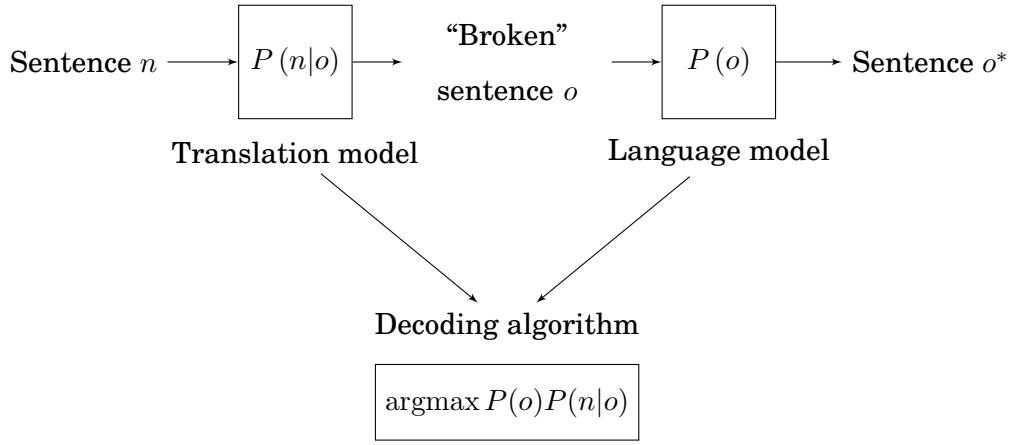

Figure 4.10: The decoding process.

The language can be model can be expressed as:

$$P(o) = P(o_1, \ldots, o_n) = \prod_i (o_i|o_{i-1}, .., o_1)\,. \tag{4.46}$$

Under the Markov's assumption (Section 4.2.1), the probability of a word depends only on the previous word in the sequence, therefore the above expression becomes:

$$P(o) = P(o_1, \ldots, o_n) = \prod_i (o_i|o_{i-1}) \tag{4.47}$$

The simplest choice for the translation model is a word-word model, which represents the likelihood that two words n and o are a mutual translation:

$$P(n|o) = P(n_1|o_1)\, P(n_2|o_2) \ldots P(n_n|o_n) = \prod_i P(n_i|o_i) \tag{4.48}$$

The decoder identifies the sentence which maximises the translation and language model probabilities (*search problem*). By replacing Eq. (4.47) and Eq. (4.48) into (4.45), the final expression is obtained:

$$o^* = \underset{o}{\operatorname{argmax}}\, P\left(o|n\right) = \underset{o}{\operatorname{argmax}} \prod_i \left(o_i|o_{i-1}\right) P\left(n_i|o_i\right). \tag{4.49}$$

Equation (4.49) is formally equivalent to a Hidden Markov Model. The solution can therefore be retrieved by a standard Viterbi algorithm for bigrams (Section 4.2.4).

A way of enhancing translation accuracy is by considering phrases (i.e. sequences of words) instead of single words as units of translation [83]. This approach involves three steps: first, the sentence is split into phrases; second, each phrase is translated according to the technique shown above; and third, the resulting phrases are reordered. The model requires the definition of a *translation probability* and a *distortion probability* for the second and third phases, respectively. In this context, distortion refers to a word occupying different positions in the sentences for language N and O.

4.3.2 Training of the model

A training phase is required to estimate the probabilistic distributions which describe the language and translation models. The language model parameters are estimated by counting word transitions in a text corpus according to the following procedure: first, the text in the corpus is converted into a stream of words; second, the number of transitions from one word to another is counted, as well as the number of occurrences of each word; third,the Maximum Likelihood Estimates for the transition probability distributions are calculated according to Eq. (4.50) [84]:

$$P\left(o_i|o_{i-1}\right) = \frac{C\left(o_{i-1} \rightarrow o_i\right)}{C\left(o_{i-1}\right)} \tag{4.50}$$

The translation parameters can be estimated using a large bilingual training set, in which sentences in the two languages are paired. Knowing the

pairs of words (phrases) it is possible to map the two languages into a word (phrase) alignment and obtaining MLE values by counting pair occurrences and normalising the results according to Eq. (4.51) [83]:

$$P(n|o) = \frac{C(n \rightarrow o)}{C(o)} \tag{4.51}$$

Distortion probability can be modelled in different ways. A simple model which penalises large distortions by assigning lower probability to larger distortions is usually employed [83].

4.4 Input system for natural language part programming

In Section 4.3, a statistical model for interpreting part programs expressed in natural language was presented. On the that basis, a software was implemented in the Python programming language to translate the natural language input into a structured language which can be directly executed by the process controller.

The software consists of two main modules: the *training* module, which is devolved to the estimation of the probabilistic distributions which describe the language and translation models, and the *decoding* module, which is used to recover the most probable expression in the process controller language for a given input command expressed in natural language.

The estimation of the language model is based on Eq. (4.50): a number of part programs in the controller language constitute the training corpus, which is parsed in order to count word transitions. For the estimation of the translation model, a bilingual corpus consisting of paired expressions in the two languages is employed. The pairs of words are extracted and counted to compute the MLE estimates (Eq. (4.51)).

The decoding module implements the Viterbi decoding algorithm (Sec. 4.2.4): the sequence of expressions in the natural language sentence repre-

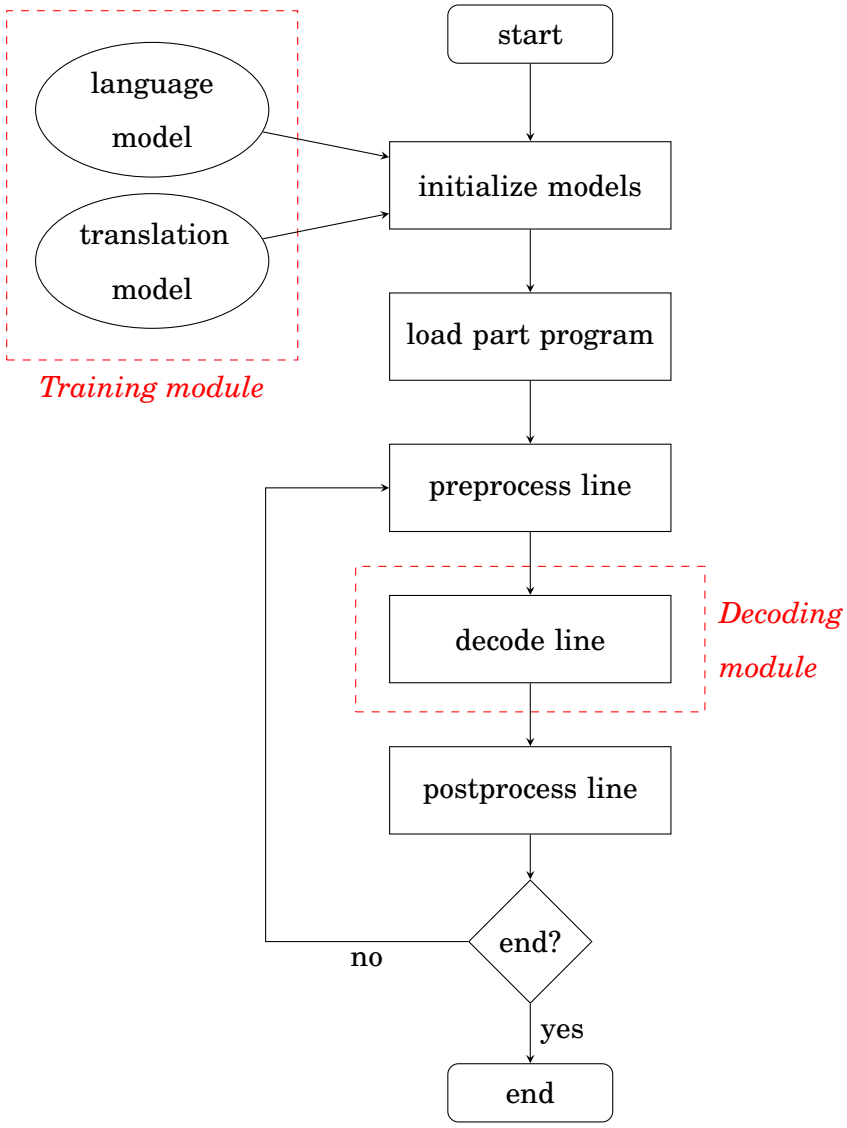

Figure 4.11: Workflow of the software for inputting of part programs expressed in natural language.

sents the observation symbol sequence of a Hidden Markov Model, whose hidden state sequence is the sentence in the controller language that needs to be recovered.

The workflow of the program is reported in Fig. 4.11. At the start of the execution the statistical models estimated by the training module are

initialised. Then, the input part program is loaded and split into a series of command lines. Each line is preliminarily processed before undergoing the decoding procedure: numbers are removed, replaced by a standard placeholder and stored for later reinsertion in the translated code, while the text part of the command is converted to lower case. The optimum sentence in the destination language is then recovered by the decoding module. Finally, numerical values are restored in their original positions and the translated line is ready to be executed by the process controller. The complete source code of the system is reported in Appendix B.

Chapter 5

Experimental investigations

The previous chapter described the design, integration and automation of a laser micromachining system based on a infrared, pulsed, Yb-doped Fiber Laser.

Micromachining experiments were conducted with the laser system to study the effects of the various parameters on the micromorphologies resulting from the process. Both metals and non-metals material were investigated in different micromachining processes. This chapter describes in detail the experimental work conducted.

5.1 Experimental procedure

In all the experimental work reported in this chapter, the following procedure was followed:

1. identification of the optimal focus condition. Preliminary experiments are conducted to find the correct position of the focal plan on the workpiece surface. A number of microfeatures are machined, while at the same time measurements of the effective distance between the lens and the workpiece are taken using a custom-built mechanical comparator with micrometer accuracy. The morphology of the resulting microfea-

tures are then analysed by means of an optic microscope to identify the optimal focus condition. The chosen focal plane position is then used for the experiment;

2. identification of the optimal range of parameters. Preliminary experiments with several levels of the parameters under investigation are conducted and the resulting microfeatures are analysed by optical microscopy, in order to restrict the parameter values to their most interesting ranges;

3. the experimental plan and the relative part program are elaborated;

4. the actual experiment is performed by the Fiber Laser micromachining system in an automated way;

5. the resulting microfeatures are measured by confocal microscopy and then analysed.

5.2 Microgrooving of AISI 304 stainless steel

Experiments were conducted by means of the Fiber Laser micromachining setup in order to study the microgrooving of AISI 304 austenitic stainless steel (UNI EN 10088-3:2005). The nominal composition of the material is reported in Table 5.1.

An experimental approach was applied to study the influence of the main process parameters on the microgroove geometric features. Strips were cut from a 5 mm thick rolled sheet of AISI 304 austenitic stainless steel and lapped to smoothen their surface. Before and after the laser grooving operations, the samples were ultrasonically cleaned in acetone and dried in air.

Experiments were carried out according to a plan based on a full factor design, consisting of three levels for laser power P ($1.5\,W$, $2.5\,W$ and $3.5\,W$) and four levels for feed rate v ($0.5\,mm\,s^{-1}$, $1\,mm\,s^{-1}$, $2\,mm\,s^{-1}$ and $4\,mm\,s^{-1}$).

Table 5.1: Chemical composition of AISI 304 stainless steel (UNI EN 10088-3:2005).

Element	%
C	0.018
Mn	1.720
Si	0.360
P	0.027
S	0.029
Cr	18.300
Ni	8.010
N	0.077
Co	0.180

The resulting microfeatures were then measured by confocal microscopy (Olympus LEXT OLS 3000 [85]), to evaluate the effect of process parameters on properties such groove depth, groove width and piled-up material (amount of molten material from the microgroove region which resolidifies and accumulates around the microgrooved region). The laser focal plan was kept constant during the execution of the experiment.

Fig. 5.1 shows the digital reconstructions of the three-dimensional microtopographies of the microgrooves obtained with $P = 1.5\,W$. The visual reconstruction is the result of merging a height map of 768 x 768 points (192 μm x 192 μm size) obtained by confocal laser scanning and a RGB colour map of the same size obtained by traditional imaging. Both images were acquired simultaneously.

The depth of the microgrooves decreases with increasing feed rate. The width of the features follows a similar trend. The reconstruction of the microfeature machined at lower feed rate (Fig. 5.1a and 5.1b) shows the presence of debris within the microgroove area, due to the resolidification of melted ma-

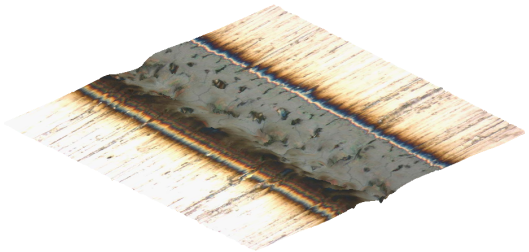

(a) $v = 0.5\,mm\,s^{-1}$

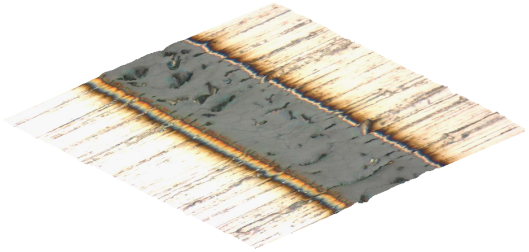

(b) $v = 1\,mm\,s^{-1}$

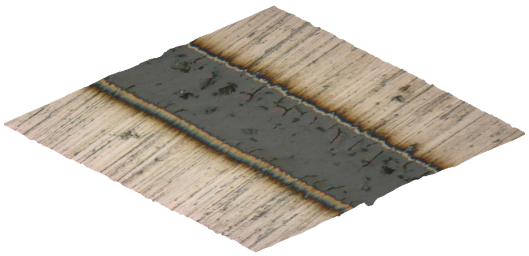

(c) $v = 2\,mm\,s^{-1}$

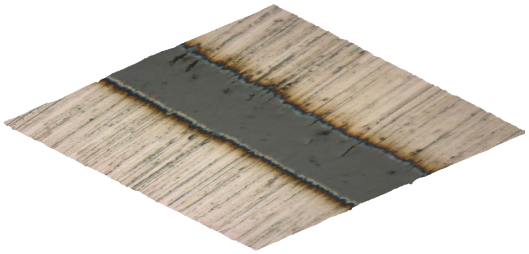

(d) $v = 4\,mm\,s^{-1}$

Figure 5.1: 3D reconstruction with overimposed pictures (height magnified) of microgrooves generated by laser scanning on AISI 304 stainless steel with power $P = 1.5\,W$.

terial. This effect is attenuated by the increase in feed rate and disappears completely for $v = 4\ mm\ s^{-1}$ (Fig. 5.1d).

Fig. 5.2 shows the visual renderings of the microgrooves obtained with $P = 2.5\ W$. Like before, depth and width of the microgroove decrease with increasing feed rate. The splatter patterns are still present, with a stronger effect at the lowest feed rate.

Finally, the geometries obtained with $P = 3.5\ W$ are represented in Fig. 5.3. As it can be seen, the surfaces machined with a feed rate $v < 1\ mm\ s^{-}1$ are heavily affected by resolidification, to the extend that no clean grooving morphology can be identified. At higher feed rate the microgrooves present micromorphologies similar to the ones obtained at lower speed.

In the experiment, the incidence of resolidification increased with decreasing feed rate and increasing average power. This is consistent with findings in previous studies of laser microgrooving [86].

The 3D raster data acquired by means of the confocal microscope can be used to quantify the average values of the properties of interest of the microgroove.

The Abbott-Firestone surface curve (*areal material ratio curve*), which is represented on Fig. 5.4, allows to characterise the bearing of an area according to the height distributions obtained by a raster scanning. Formally, the curve represents the sample probability density function of the height $Z(x, y)$ within the evaluation area, but it can be defined as well as the probability of contact between the measured surface and a perfect flat surface.

A number of useful parameters can be defined through a particular geometric construction that takes place on the Abbott-Firestone curve (Fig. 5.4, right): the *core roughness depth* (*Sk*), the *reduced peak height* (*Spk*) and the *reduced valley depth* (*Svk*) [87]. The core roughness depth describes the area of the surface spanning about 40% of the material ration curve, while the *Spk* and *Svk* parameters define areas respectively upper and under the *Sk*

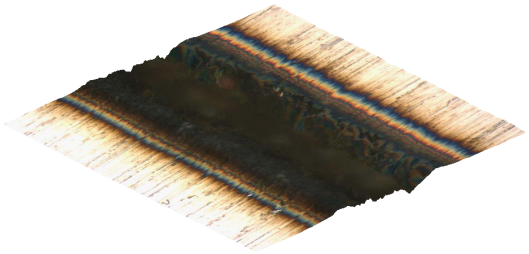

(a) $v = 0.5\,mm\,s^{-1}$

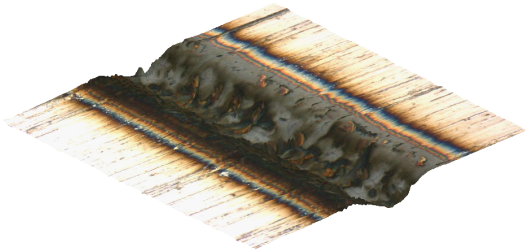

(b) $v = 1\,mm\,s^{-1}$

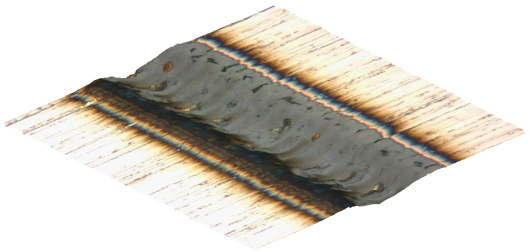

(c) $v = 2\,mm\,s^{-1}$

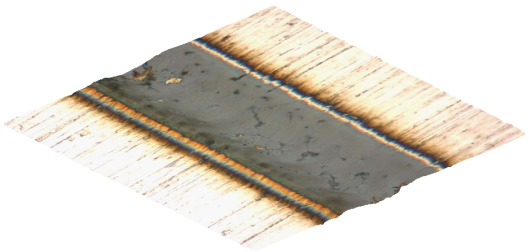

(d) $v = 4\,mm\,s^{-1}$

Figure 5.2: 3D reconstruction with overimposed pictures (height magnified) of microgrooves generated by laser scanning on AISI 304 stainless steel with power $P = 2.5\,W$.

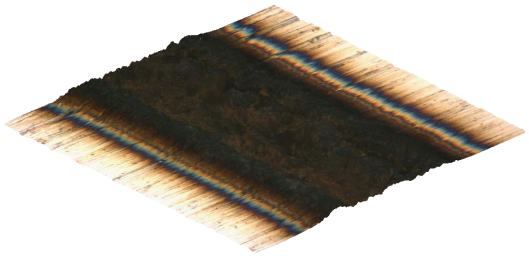

(a) $v = 0.5\,mm\,s^{-1}$

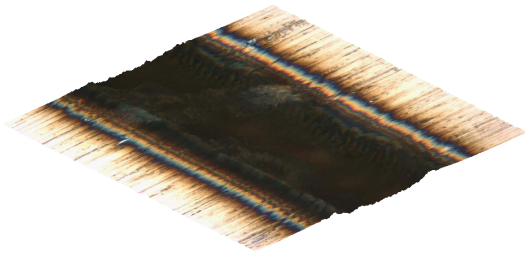

(b) $v = 1\,mm\,s^{-1}$

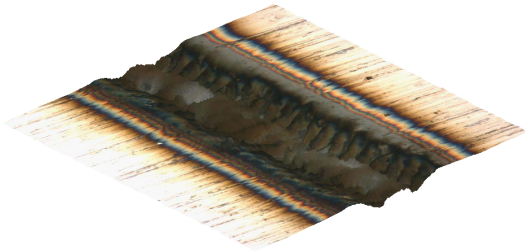

(c) $v = 2\,mm\,s^{-1}$

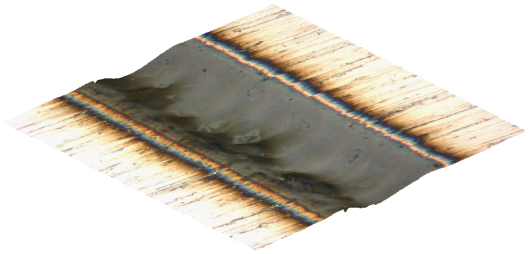

(d) $v = 4\,mm\,s^{-1}$

Figure 5.3: 3D reconstruction with overimposed pictures (height magnified) of microgrooves generated by laser scanning on AISI 304 stainless steel with power $P = 3.5\,W$.

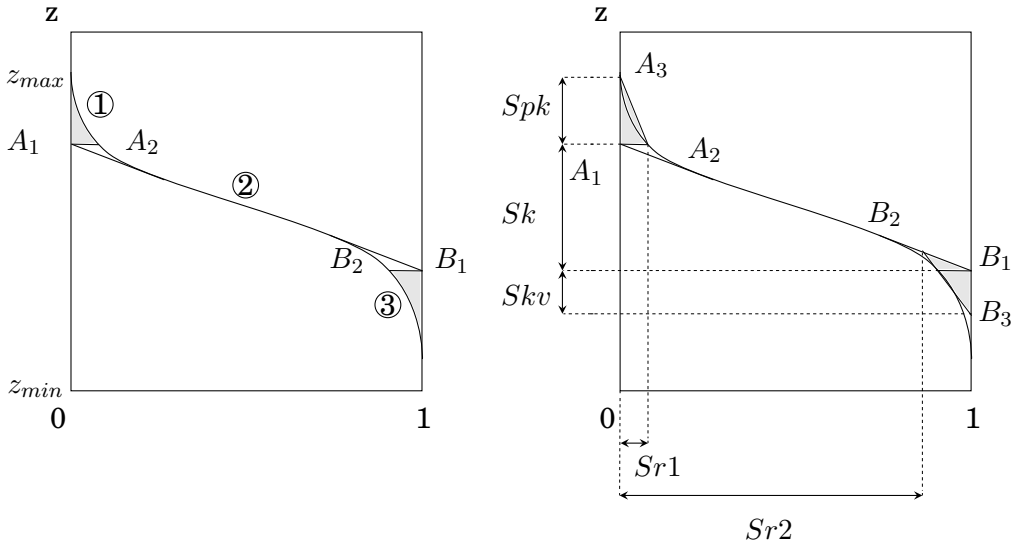

Curve area	corresponds to:
1	piled-up material
2	undisturbed material
3	microgroove

Parameter	quantifies:
Svk	piled-up material height
Spk	microgroove depth
$Sr1$	piled-up material width
$1 - Sr2$	groove width

Figure 5.4: Application of the Abbott-Firestone curve to the estimation of the microgroove and of piled-up material size.

area. Finally, the parameter *Mr1* represents the percentage of surface material that constitutes the peaks associated with *Spk* and the quantity *1 - Sr2* the percentage of surface that comprises the valleys associated with *Svk*. The parameters derived from the Abbott-Firestone curve are generally referred to as *Sk parameters*.

In the microgrooving case, the core surface corresponds to the undisturbed material on the sides of the microgroove, while the peaks are due to the piled-up material and the only valley to the removal of material from the microgroove region. The *Svk* and *Spk* parameters can therefore be used as average measures of the microgroove depth and of the piled-up material height, respectively. The quantities *Sr1* and 1 - *Sr2* represents the average width of the piled-up material and of the microgroove.

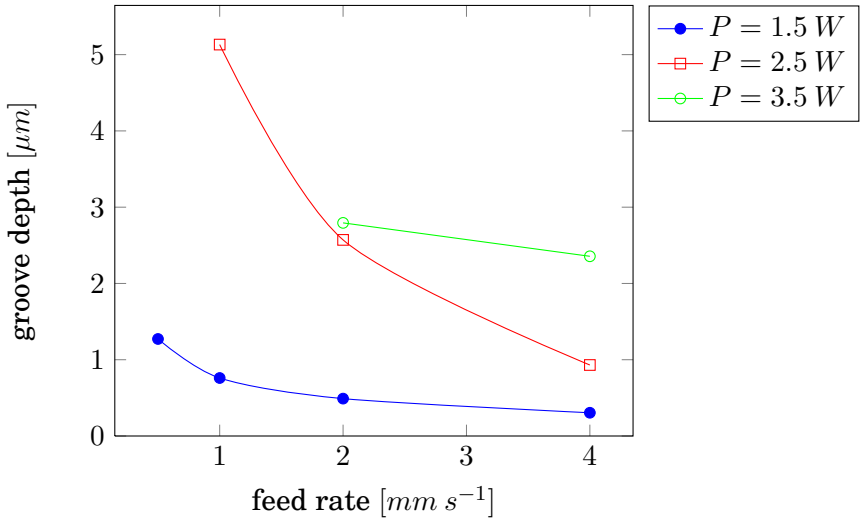

Figure 5.5: The variation curve of the average depth with feed rate for microgrooving of AISI 304 stainless steel.

The values of the parameters discussed above were calculated for the microgrooves generated in the experiment, without considering the microfeatures affected to a large extend by the resolidification defects, and are fully reported in Appendix C. Fig. 5.5 shows the variation of the average depth of the microgroove with the feed rate. The *Svk* values confirm the trend already observed in the qualitative analysis: the removal of material increases with increasing power and decreases with increasing feed rate. The variation with feed rate is stronger at the higher power.

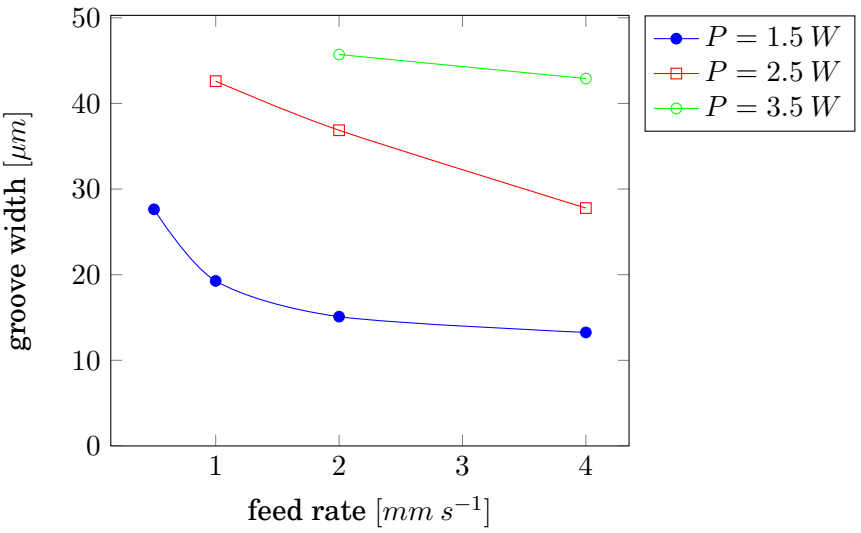

Figure 5.6: The variation curve of the average width with feed rate for microgrooving of AISI 304 stainless steel.

The same pattern is repeated in Fig. 5.6 where the microgroove width is plotted against the feed rate. It can be noted that at all the considered power levels the width of the microgroove is inferior to the laser beam spot diameter (Section 3.1.2). This can be explained by the Gaussian distribution of the laser power within the beam: the radiation intensity exceed the vaporisation threshold only in the central part of the beam.

Figures 5.8 and 5.7 show the variation of average width and height of the piled-up material on the side of the microgroove, respectively. The two plots present conflicting trends: for power up to $2.5\ W$ the piled-up material width initially strongly decreases with the feed rate down to a minimum for $v = 2\ mm\ s^{-1}$, and then increases again. The only two data points available for the higher power level indicates a tendency for slightly lower widths of the piled-up material at that power. On the other hand, the average pile-up height plot shows an overall tendency to decrease with increasing feed rate values.

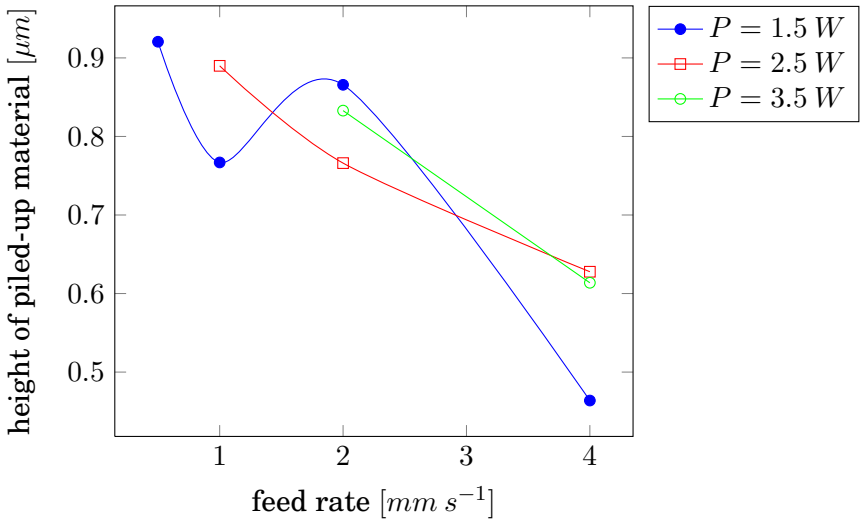

Figure 5.7: The variation curve of the average height of the piled-up material with feed rate for microgrooving of AISI 304 stainless steel.

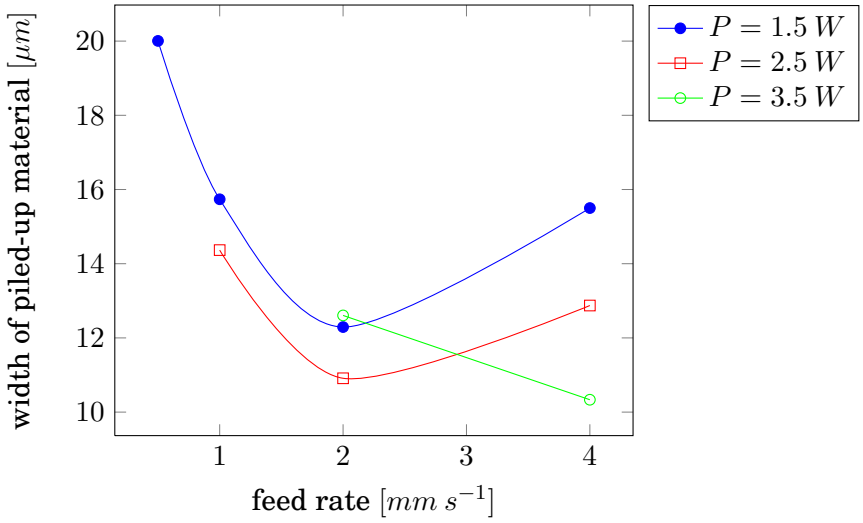

Figure 5.8: The variation curve of the average width of the piled-up material with feed rate for microgrooving of AISI 304 stainless steel.

The two graphs suggest that, for high power applied to the specimen surface (low feed rate and high power), the total amount of resolidification on the

side of the microgroove is larger. When applied power decreases (higher feed rate), the intensity of resolidification decreases as well. The spread of the piled-up material depends on the feed rate: at lower speed the piling-up is concentrated on the immediate area outside the microgroove, with the width showing an increase with a corresponding reduction of the piled-up material height at higher feed rate.

5.3 Microgrooving of Diamond-Like Carbon coatings on AISI 440 stainless steel

A microgrooving experiments similar to the one discussed above was performed on AISI 440 stainless steel strips coated with Diamond-Like Carbon (DLC) for surgical instruments.

The experiment have been carried out according to a plan based on a full factor design, consisting of three levels for laser power P ($1.5\ W$, $2\ W$ and $2.5\ W$) and of four levels for feed rate v ($1\ mm\ s^{-1}$, $1.5\ mm\ s^{-1}$, $2\ mm\ s^{-1}$ and $2.5\ mm\ s^{-1}$). Like before, the resulting microfeatures were measured by confocal microscopy to obtaine 3D height maps for the analysis.

Fig. 5.9 - 5.11 report digital reconstructions of the three-dimensional topographies of the microgrooves for all the three levels of laser power. Once again, some of the resulting microfeatures present a good groove profile, while others suffer the presence of debris and defects due to resolidification of the material removed from the working region. In general, surfaces where larger amounts of energy were applied due to the combination of low feed rate and high laser power present more intense resolidification phenomena.

A quantitative analysis was conducted by means of the *Sk* parameters to evaluate the effect of process parameters on average microogroove depth, microgroove width and piled-up material.

Fig. 5.12 shows the variation of the average microgroove depth with the

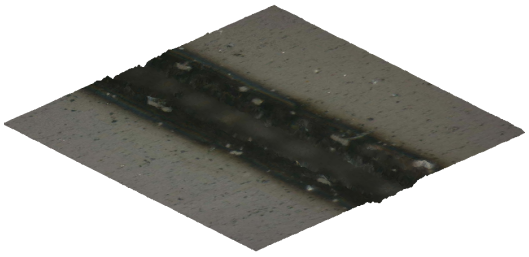

(a) $v = 1\,mm\,s^{-1}$

(b) $v = 1.5\,mm\,s^{-1}$

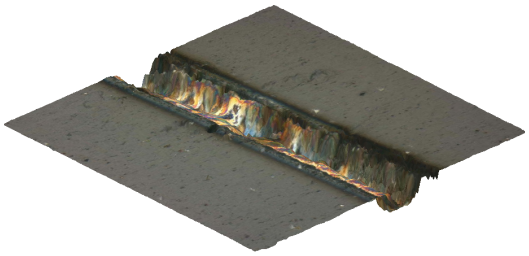

(c) $v = 2\,mm\,s^{-1}$

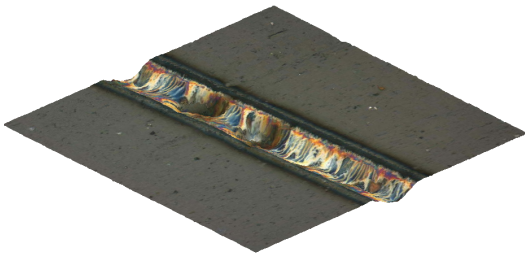

(d) $v = 2.5\,mm\,s^{-1}$

Figure 5.9: 3D reconstruction with overimposed pictures (height magnified) of microgrooves generated by laser scanning on DLC-coated AISI 440 stainless steel with power $P = 1.5\,W$.

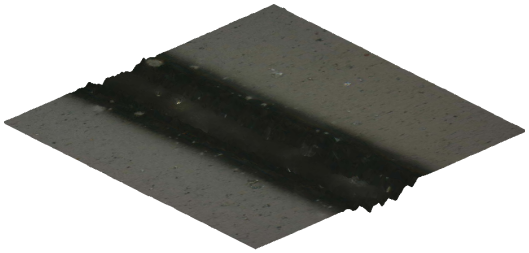

(a) $v = 1\,mm\,s^{-1}$

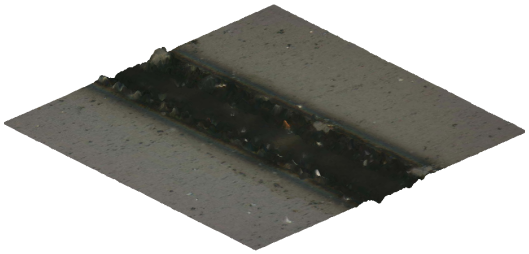

(b) $v = 1.5\,mm\,s^{-1}$

(c) $v = 2\,mm\,s^{-1}$

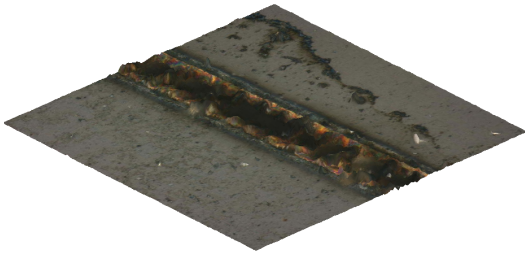

(d) $v = 2.5\,mm\,s^{-1}$

Figure 5.10: 3D reconstruction with overimposed pictures (height magnified) of microgrooves generated by laser scanning on DLC-coated AISI 440 stainless steel with power $P = 2\,W$.

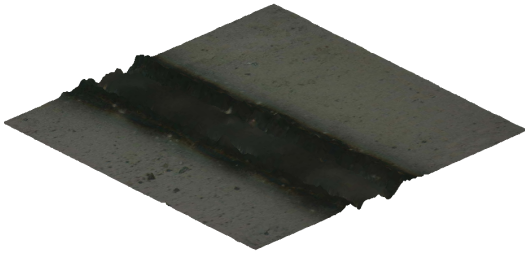

(a) $v = 1\,mm\,s^{-1}$

(b) $v = 1.5\,mm\,s^{-1}$

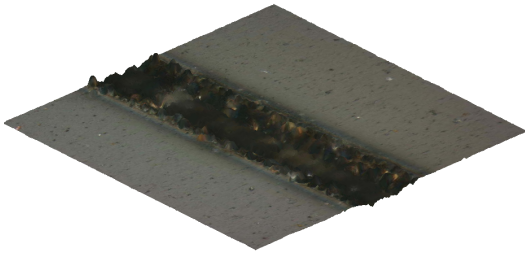

(c) $v = 2\,mm\,s^{-1}$

(d) $v = 2.5\,mm\,s^{-1}$

Figure 5.11: 3D reconstruction with overimposed pictures (height magnified) of microgrooves generated by laser scanning on DLC-coated AISI 404 stainless steel with power $P = 2.5\,W$.

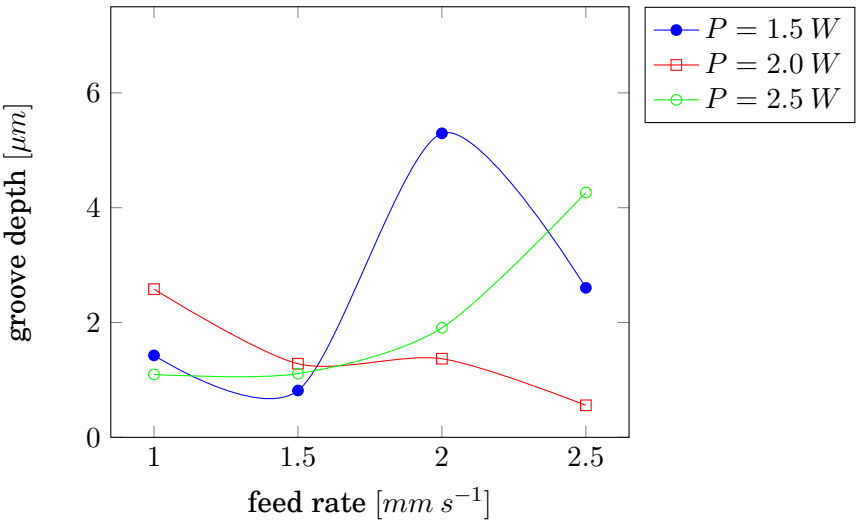

Figure 5.12: The variation curve of the average depth with feed rate for microgrooving on DLC-coated AISI 440 stainless steel.

feed rate. No clear trend can be identified: at the intermediate level of power, the average depth of the microgrooves decreases slightly with increasing feed rate, as expected; at the other power levels, efficient material removal only took place at the higher feed rate, when the intensity of resolidification was limited. A similar pattern is followed by the average microgroove width, as reported in Fig. 5.13.

Fig. 5.14 reports the variation of the average height of the piled-up material on the sides of the microgroove. The curves for power of $1.5\ W$ and $2.5 W$ are similar: in both cases, the average height of the piled-up material is larger at lower velocities, when strong resolidification occurs. The data points for the middle level of power show an opposite tendency. Overall, the height of the piled-up material seems to be mainly dependent on the laser power.

The average width of the piled-up material does not present strong variations (Fig. 5.15).

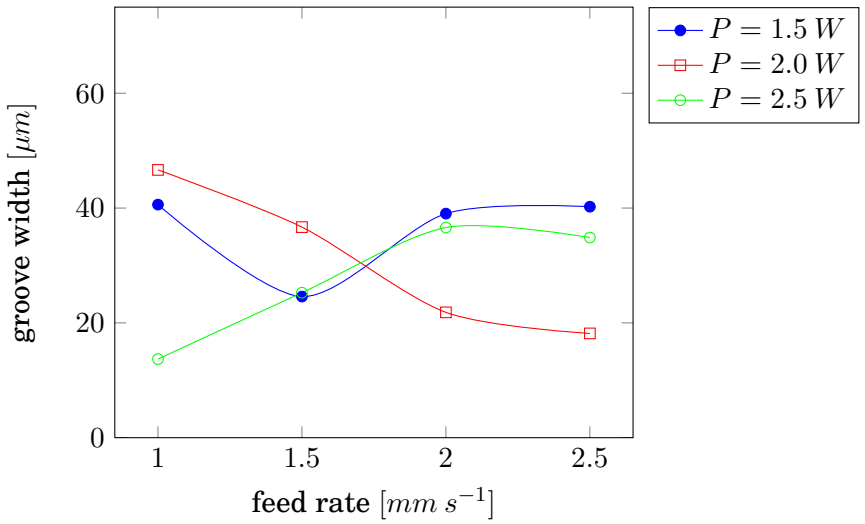

Figure 5.13: The variation curve of the average width with feed rate for microgrooving on DLC-coated AISI 440 stainless steel.

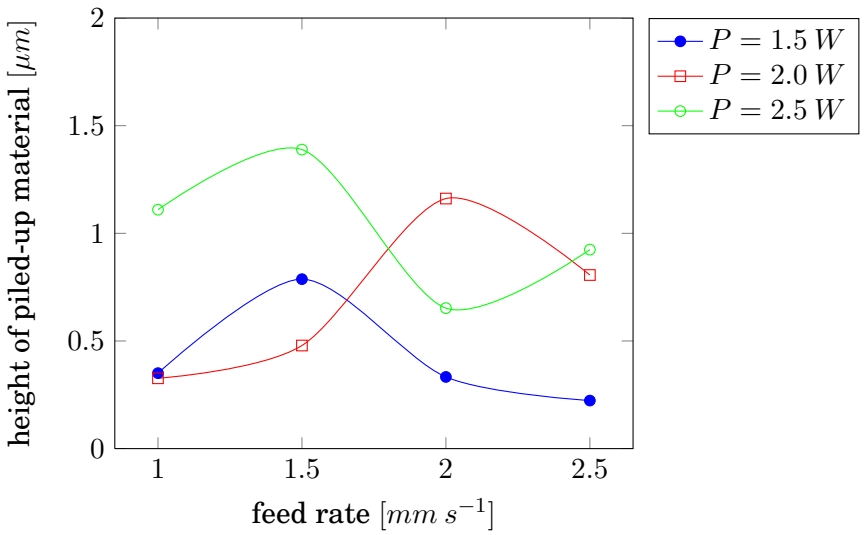

Figure 5.14: The variation curve of the average width of the piled-up material with feed rate for microgrooving on DLC-coated AISI 440 stainless steel.

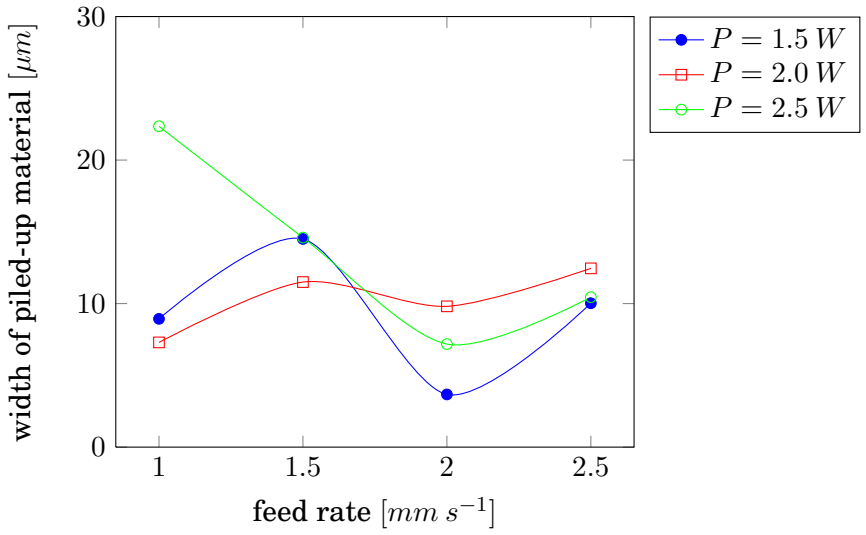

Figure 5.15: The variation curve of the average height of the piled-up material with feed rate for microgrooving on DLC-coated AISI 440 stainless steel.

5.4 Micromilling of pockets on AISI 304 stainless steel

The Fiber Laser setup was applied to the micromachining of an L-shaped pocket on an AISI 304 stainless steel surface. This experiment was conducted in order to verify the capability of the laser setup to perform micromachining processes based on arbitrary part programs.

The part program was defined by non-structured text listing expressed in natural language, according to the part programming approach proposed in Section 4.3.

Listing 5.1: Excerpts from the part program for the micromachining of an L-shaped pocket expressed in natural language.

```
1 Set power 4 Watts
  set feedrate 500 micron/sec
  mill 900 microns along x
  move -900 microns along x
```

```
move 50 microns along y
milling 900 microns along x
moving -900 microns along x
moving 50 microns along y
        (...)
mill 900 microns on x
move -900 microns along x
move 50 microns along y
set power 6 Watts
set velocity 700 micron/s
mill 300 microns along x
        (...)
mill 300 microns along x
move -300 microns along x
move 50 microns along y
```

Listing B.4.1 reports excerpts from the input file which describes the task in English language. The first lines contain commands to set laser power and feed rate, whereas the following sentences describe the pattern of overlaps responsible for the material removal.

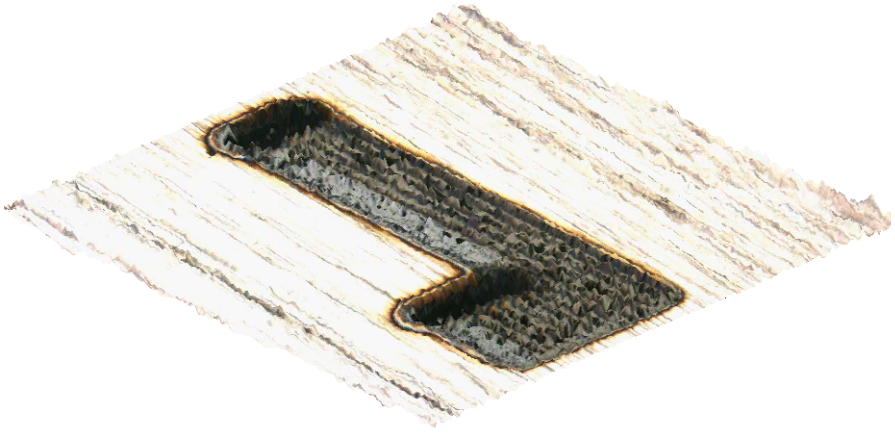

Figure 5.16: 3D microtopography of the L-shaped pocket obtained by Fiber Laser micromachining on the surface of an AISI 304 stainless steel specimen.

As it can be seen, similar commands are expressed with different choices of English words, i.e. the words “movement", “move", or “moving" are used without distinction to describe movements of one of the translation stage axes. This is to highlight how the planner does not need to be consistent in their use of the language when elaborating the part program.

The microtopography generated by the execution of the part program is shown in the reconstruction of Fig. 5.16. As it can be seen, the part program file was correctly interpreted and resulted in the desired shape being generated.

Conclusion

Industrial products with small feature sizes are becoming increasingly important in a large number of industries. The structures of microparts are getting more and more complex, while their sizes are becoming smaller, which imposes a critical challenge to their manufacturing issues.

Micromanufacturing encompasses several different material process techniques. Among those based on the selective removal of material from the workpiece surface, laser micromachining has gained an increasingly wide popularity.

In particular, short-pulsed Fiber Lasers represent an ideal solution to many micromachining tasks: their high quality laser beam allows precise energy deposition on a micrometer scale at high processing speeds. Excess material is removed from the workpiece by fast melting and evaporation, with minimal or no thermally induced damage to the structure of the microcomponent, making Fiber Laser an important tool for several industrial applications, such as microdrilling and microcutting. Moreover, the possibility to accurately shape the high quality laser beam in time and space makes Fiber Lasers an ideal tools for microwelding and microcladding application, as well.

The problem of accurately planning pulsed Fiber Laser micromachining processes is not trivial. Several process parameters need to be selected in order to delivery an efficient and effective process. Moreover, micromanufacturing of three-dimensional microparts requires the elaboration of complex

part programs. The traditional approach based on the use of rigid-syntax, toolpath-based procedural languages for part programming is a substantial cause of impediment to the quick development of new laser micromachining processes, since it is slow and requires high expertise in part programming with the CNC language of choice.

In this thesis, micromachining processes based on infrared pulsed Fiber laser were investigated. A laser micromachining setup based on a 10 W Yb-doped pulsed Fiber laser source was designed, integrated and automated in order to conduct experimental activity. A part-positioning system based on a *x-y* stage is adopted for the generation of feed motion between laser beam and micropart surface, in order to obtain high accuracy in the workpiece positioning. The focusing device is mounted on a precise translation stage to enable processing of 3D shapes. The laser micromachining process is run by a PC-based process control software, implemented in LabVIEW environment.

A new approach to part programming for laser micromachining was proposed. The concept is based on the use of natural language for the generation of part programs: the traditional ordered list of program blocks in a ASCII formatted file is replaced with almost free syntax, non procedural sentence commands, expressed in natural language and elaborated without any particular syntax constraints. A statistical model for the translation of the input commands into a language specific to the process controller based on Hidden Markov Models was developed.

Based on the proposed approach, an input processor system for the pulsed Fiber Laser micromachining setup was implemented as a Python program. The software implements the Viterbi algorithm for the interpretation of natural language commands according to a statistical knowledge base, learnt from real-world examples.

Experimental work was conducted by means of the pulsed Fiber Laser micromachining setup on metal and non-metal surfaces. In particular, mi-

crogrooving was performed on AISI 304 stainless steel to investigate the effects of the various parameters on the micromorphologies resulting from the process. An experimental plan based on a full factor design with three levels of power in the $2.5 - 3.5\,W$ range and four levels of feed rate ranging from 0.5 to $4 mm\,s^{-1}$ was elaborated and executed. The specimens were then measured by confocal microscopy (Olympus LEXT).

The resulting microfeatures were found to be subject to resolidification effects: part of the material removed from the groove region undergoes a solidification and accumulates in form of splats on the periphery of the microgroove (piling-up). In some cases, the intensity of resolidification was strong enough to affect all the section of the microgroove, reducing the depth of the morphology and and the finish of the region.

The average size of all the microgrooves was analysed from the height map measured by the confocal microscope, together with the average dimensions of the piled-up material. *Sk* parameters (ISO 13565) were used to quantifies such dimensions: in particular, the *Svk parameter* and the *Spk* parameter were used to estimate the average depth of the microgrooves and the average height of the piled-up material, respectively, whereas the quantities 1 - *Sr2* and *Sr1* were used as estimation of the average width of the microgroove region and of the width of the material accumulated on the sides of the region, respectively.

Both average depth and width of the microgroove were found to generally increase with decreasing feed rate and increasing laser power. However, when the combination of the two parameters resulted in the total amount of energy transmitted to the material exceeding a certain threshold, the surge in resolidification prevented any depth increase.

The accumulation of piled-up material seems to be dependent mainly on the value of feed rate. Average pile-up height presents a clear decreasing trend with increasing feed rate, whereas average piled-up material width de-

creases down to a minimum (feed rate $v = 2mms^{-1}$) and then increases again. Variations in laser power only slightly affect the accumulation of piled-up material.

A similar microgrooving experiment was conducted on strips of AISI 440 stainless steel coated with a layer of Diamond-Like Carbon (DLC): a full factor design with three levels of power in the $1.5 - 2.5\,W$ range and four levels of feed rate ranging from 1 to $2.5\,mm\,s^{-1}$ was elaborated.

As in the previous case, the morphology of the obtained microfeatures was largely dependent on whether or not resolidification of the removed material had taken place. No clear trend in the variation of average microgroove depth against feed rate and laser power was identified: microgroovings machined at the intermediate setting of power showed a slight depth decrease with increasing feed rate, as expected; at the other power levels, microgroove depth presented an opposite tendency. The same pattern is followed by the average microgroove width, but with less dispersion of the data points.

As for the piled-up material, its average width increases with increasing power, while not showing any systematic variations when plotted against the feed rate. The average piled-up material height remained approximately constant in the experiment.

Finally, micromachining of an L-shaped pocket on the surface of an AISI 304 specimen was performed to validate the input system based on natural language. A part program expressed in English was elaborated, processed by the input software system and then successfully executed by the process controller.

In conclusion, the laser micromachining system based on infrared pulsed Fiber Laser was successfully applied to micromachining of metallic and ceramic surfaces, proving to be well suited to micromachining tasks.

More extensive investigations need to be carried out in future to increase the amount of data available. Statistical techniques such *Design of Experi-*

ments and *Response Surface Methodology* may be employed to develop semiempirical model of the machining processes, which could constitute the basis for a full CAPP system for Fiber Laser micromachining.

Future work on the natural language system for part programming may be aimed at the integration of the translation module with a toolpath calculator system. In this way, higher level instructions could be used in part programs and automatically executed by the controller.

Bibliography

[1] N. Dahotre and S. Harimkar. *Laser Fabrication and Machining of Material*. Springer, 2008.

[2] J. Canning. Fibre lasers and related technologies. *Optics and Lasers in Engineering*, 44(7):647 – 676, 2006.

[3] R. Paschotta, J. Nilsson, A. C. Tropper, and D. C. Hanna. Ytterbium-doped fiber amplifiers. *IEEE Journal of Quantum Electronics*, 33(7):1049 – 1056, 2002.

[4] R. Paschotta. *Encyclopedia of Laser Physics and Technology*. Wiley-VCH, 2008.

[5] T. Masuzawa. State of the Art of Micromachining. *CIRP Annals - Manufacturing Technology*, 49(2):473 – 488, 2000.

[6] K. F. Ehmann. A Synopsis of U. S. micro-manufacturing research and development activities and trends. In *Proc. of the Third International conference on Multi-Material Micro-Manufacture*, 2007.

[7] L. Alting, F. Kimura, H. N. Hansen, and G. Bissacco. Micro Engineering. *CIRP Annals - Manufacturing Technology*, 52(2):635 – 657, 2003.

[8] Y. Qin, A. Brockett, Y. Ma, A. Razali, J. Zhao, C. Harrison, W. Pan, X. Dai, and D. Loziak. Micro-manufacturing: research, technology outcomes and

development issues. *The International Journal of Advanced Manufacturing Technology*, 47:821–837, 2010. 10.1007/s00170-009-2411-2.

[9] X. Zhang, X. N. Jiang, and C. Sun. Micro-stereolithography of polymeric and ceramic microstructures. *Sensors and Actuators A: Physical*, 77(2):149 – 156, 1999.

[10] C. Malek and V. Saile. Applications of LIGA technology to precision manufacturing of high-aspect-ratio micro-components and -systems: a review. *Microelectronics Journal*, 35(2):131 – 143, 2004.

[11] B. Sha, S. Dimov, C. Griffiths, and M.S. Packianather. Investigation of micro-injection moulding: Factors affecting the replication quality. *Journal of Materials Processing Technology*, 183(2-3):284 – 296, 2007.

[12] M. Geiger, M. Kleiner, R. Eckstein, N. Tiesler, and U. Engel. Microforming. *CIRP Annals - Manufacturing Technology*, 50(2):445 – 462, 2001.

[13] F. Vollertsen, H. Schulze Niehoff, and Z. Hu. State of the art in micro forming. *International Journal of Machine Tools and Manufacture*, 46(11):1172 – 1179, 2006. 1st International Conference on New Forming Technology.

[14] X. Luo, K. Cheng, D. Webb, and F. Wardle. Design of ultraprecision machine tools with applications to manufacture of miniature and micro components. *Journal of Materials Processing Technology*, 167(2-3):515 – 528, 2005. 2005 International Forum on the Advances in Materials Processing Technology.

[15] G.M. Robinson and M.J. Jackson. A review of micro and nanomachining from a materials perspective. *Journal of Materials Processing Technology*, 167(2-3):316 – 337, 2005. 2005 International Forum on the Advances in Materials Processing Technology.

[16] A. Dhanorker and T. Ozel. Meso / micro scale milling for micro-manufacturing. *International Journal of Mechatronics and Manufacturing Systems*, 1:23–42(20), 2008.

[17] D. T. Pham, S. S. Dimov, S. Bigot, A. Ivanov, and K. Popov. Micro-EDM–recent developments and research issues. *Journal of Materials Processing Technology*, 149(1-3):50 – 57, 2004. 14th Interntaional Symposium on Electromachining (ISEM XIV).

[18] E. Uhlmann, S. Piltz, and U. Doll. Machining of micro/miniature dies and moulds by electrical discharge machining–Recent development. *Journal of Materials Processing Technology*, 167(2-3):488 – 493, 2005. 2005 International Forum on the Advances in Materials Processing Technology.

[19] L. De Chiffre, H. Kunzmann, G.N. Peggs, and D.A. Lucca. Surfaces in Precision Engineering, Microengineering and Nanotechnology. *CIRP Annals - Manufacturing Technology*, 52(2):561 – 577, 2003.

[20] C. Biffi, N. Lecis, B. Previtali, M. Vedani, and G. Vimercati. Fiber laser microdrilling of titanium and its effect on material microstructure. *The International Journal of Advanced Manufacturing Technology*, pages 1–12, 2010. 10.1007/s00170-010-2918-6.

[21] M. Baumeister, K. Dickmann, and T. Hoult. Fiber laser micro-cutting of stainless steel sheets. *Applied Physics A: Materials Science; Processing*, 85:121–124, 2006. 10.1007/s00339-006-3687-9.

[22] K. F. Kleine, W. J. Fox, and K. G. Watkins. Micro welding with pulsed single mode fiber lasers. In *Proceedings of ICALEO 2004*, volume 97, 2004.

[23] A.G. Paleocrassas and J.F. Tu. Inherent instability investigation for low speed laser welding of aluminum using a single-mode fiber laser. *Journal of Materials Processing Technology*, 210(10):1411 – 1418, 2010.

[24] F. Lusquiños, R. Comesaña, A. Riveiro, F. Quintero, and J. Pou. Fibre laser micro-cladding of co-based alloys on stainless steel. *Surface and Coatings Technology*, 203(14):1933 – 1940, 2009.

[25] A. Einstein. Zur Quantentheorie der Strahlung. *Physika Zeitschrift*, 18:121–128, 1917.

[26] ISO Standard 11146:2005. *Lasers and laser-related equipment - Test methods for laser beam widths, divergence angles and beam propagation ratios*. International Standard Organisation, Geneva, Switzerland, 2005.

[27] M. Bass, C. MacDonald, G. Li, C. DeCusatis, and V. Mahajan. *Handbook of Optics, Third Edition Volume V: Atmospheric Optics, Modulators, Fiber Optics, X-Ray and Neutron Optics*. McGraw-Hill Professional, 2009.

[28] A. Boudrioua. *Photonic Waveguides: Theory and Applications*. Wiley, 2009.

[29] A. Dubey and V. Yadava. Laser beam machining–A review. *International Journal of Machine Tools and Manufacture*, 48(6):609 – 628, 2008.

[30] S. Bednarczyk, R. Bechir, and P. Baclet. Laser micro-machining of small objects for high-energy laser experiments. *Applied Physics A: Materials Science and Processing*, 69(7):495 – 500, 1999.

[31] S. Dauer, S. Büttgenbach, and A. Ehlert. Rapid Prototyping of Micromechanical Devices Using a Q-Switched Nd:YAG Laser with Optional Frequency Doubling. *Sensors and Actuators A: Physical*, 76(1-3):381–385, 1999.

[32] T. Chen and R. Darling. Parametric studies on pulsed near ultraviolet frequency tripled Nd:YAG laser micromachining of sapphire and silicon. *Journal of Materials Processing Technology*, 169(2):214 – 218, 2005.

[33] A. Raval, A. Choubey, C. Engineer, and D. Kothwala. Development and assessment of 316LVM cardiovascular stents. *Materials Science and Engineering A*, 386(1-2):331 – 343, 2004.

[34] B. S. Yilbas. Parametric study to improve laser hole drilling process. *Journal of Materials Processing Technology*, 70(1-3):264 – 273, 1997.

[35] S. Bandyopadhyay, H. Gokhale, J.K. Sarin Sundar, G. Sundararajan, and S.V. Joshi. A statistical approach to determine process parameter impact in Nd:YAG laser drilling of IN718 and Ti-6Al-4V sheets. *Optics and Lasers in Engineering*, 43(2):163 – 182, 2005.

[36] E. Kacar, M. Mutlu, E. Akman, A. Demir, L. Candan, T. Canel, V. Gunay, and T. SInmazcelik. Characterization of the drilling alumina ceramic using Nd:YAG pulsed laser. *Journal of Materials Processing Technology*, 209(4):2008 – 2014, 2009.

[37] N. Nedialkov, M. Sawczak, R. Jendrzejewski, P. Atanasov, M. Martin, and G. Sliwinski. Analysis of surface and material modifications caused by laser drilling of AlN ceramics. *Applied Surface Science*, 254(4):893 – 897, 2007. Laser synthesis and processing of advanced materials - E-MRS-P Symposium.

[38] D. K. Y. Low, L. Li, and P. J. Byrd. The effects of process parameters on spatter deposition in laser percussion drilling. *Optics and Laser Technology*, 32(5):347 – 354, 2000.

[39] W. Choi and G. Chryssolouris. Analysis of the laser grooving and cutting processes. *Journal of Physics D: Applied Physics*, 28(5):873, 1995.

[40] C. Mai and J. Lin. An investigation of the surface contours in laser grooving. *The International Journal of Advanced Manufacturing Technology*, 28:76–81, 2006. 10.1007/s00170-004-2342-x.

[41] A. Stournaras, K. Salonitis, P. Stavropoulos, and G. Chryssolouris. Theoretical and experimental investigation of pulsed laser grooving process. *The International Journal of Advanced Manufacturing Technology*, 44:114–124, 2009. 10.1007/s00170-008-1818-5.

[42] Z. Bai, A. Wang, and C. Xie. Laser grooving of Al2O3 plate by a pulsed Nd:YAG laser: Characteristics and application to the manufacture of gas sensors array heater. *Materials Science and Engineering: A*, 435-436:418 – 424, 2006.

[43] D. Dhupal, B. Doloi, and B. Bhattacharyya. Pulsed Nd:YAG laser turning of micro-groove on aluminum oxide ceramic (Al2O3). *International Journal of Machine Tools and Manufacture*, 48(2):236 – 248, 2008.

[44] D. Dhupal, B. Doloi, and B. Bhattacharyya. Parametric analysis and optimization of Nd:YAG laser micro-grooving of aluminum titanate (Al2TiO5) ceramics. *The International Journal of Advanced Manufacturing Technology*, 36:883–893(11), April 2008.

[45] D. Dhupal, B. Doloi, and B. Bhattacharyya. Optimization of process parameters of Nd:YAG laser microgrooving of Al2TiO5 ceramic material by response surface methodology and artificial neural network algorithm. *Proceedings of the Institution of Mechanical Engineers, Part B: Journal of Engineering Manufacture*, 221(8):1341–1350, 2007.

[46] D. Dhupal, B. Doloi, and B. Bhattacharyya. Modeling and optimization on Nd:YAG laser turned micro-grooving of cylindrical ceramic material. *Optics and Lasers in Engineering*, 47(9):917 – 925, 2009.

[47] B. Yousef, G. Knopf, E. Bordatchev, and S. Nikumb. Neural network modeling and analysis of the material removal process during laser machining. *The International Journal of Advanced Manufacturing Technology*, 22:41–53, 2003. 10.1007/s00170-002-1441-9.

[48] S.M. Karazi, A. Issa, and D. Brabazon. Comparison of ANN and DoE for the prediction of laser-machined micro-channel dimensions. *Optics and Lasers in Engineering*, 47(9):956 – 964, 2009.

[49] Negaestani R., Sundar M., Sheikh M., Mativenga P., Li L, Li ZL, and et al. Numerical simulation of laser machining of carbon-fibre-reinforced composites. *Proceedings of the Institution of Mechanical Engineers, Part B: Journal of Engineering Manufacture*, 224(7):1017–1027, 2010.

[50] C. T. Pan and H. Hocheng. The anisotropic heat-affected zone in the laser grooving of fiber-reinforced composite material. *Journal of Materials Processing Technology*, 62(1-3):54 – 60, 1996.

[51] Z.L. Li, H.Y. Zheng, G.C. Lim, P.L. Chu, and L. Li. Study on UV laser machining quality of carbon fibre reinforced composites. *Composites Part A: Applied Science and Manufacturing*, 41(10):1403 – 1408, 2010.

[52] P. Heyl, T. Olschewski, and R. Wijnaendts. Manufacturing of 3D structures for micro-tools using laser ablation. *Microelectronic Engineering*, 57-58:775 – 780, 2001. Micro- and Nano-Engineering 2000.

[53] D. T. Pham, S. S. Dimov, C. Ji, P. V. Petkov, and T. Dobrev. Laser milling as a 'rapid' micromanufacturing process. *Proceedings of the Institution of Mechanical Engineers, Part B: Journal of Engineering Manufacture*, 218:1–7, 2004.

[54] E.Kubacki and L. Abbott. Optics for Fiber Laser Applications. Technical report, CVI Laser, 2009.

[55] M. Pettenati. Contributo allo sviluppo e validazione di un sistema di misura e di analisi microtopografico tridimensionale senza contatto per applicazioni nell'ambito delle scienze forensi. Master's thesis, University of Parma, 2001.

[56] National Instruments. LabVIEW User Manual, 2003.

[57] T. Chang and R. Wysk. *Computer-Aided Manufacturing*. Prentice Hall PTR, Upper Saddle River, NJ, USA, 1997.

[58] A. Nafis, A. Haque, and A. Hasin. Current trends in Computer Aided Process Planning. In *Proc. 7th Annual Paper Meet and 2nd International Conference*, volume 25-27 of *Mechanical Engineering Division*, pages 81–82. The Institution of Engineers, 2001.

[59] H. B. Marri, A. Gunasekaran, and R. J. Grieve. Computer-aided Process Planning: A state of art. *The International Journal of Advanced Manufacturing Technology*, 14:261–268, 1998. 10.1007/BF01199881.

[60] W. Eversheim and J. Schneewind. Computer-aided Process Planning–State of the art and future development. *Robotics and Computer-Integrated Manufacturing*, 10(1-2):65 – 70, 1993.

[61] L. Alting and H. Zhang. Computer Aided Process Planning: the state-of-the-art survey. *International Journal of Production Research*, 27(4), 1989.

[62] R. Groppetti and Q. Semeraro. Computer Aided Process Planning: the generative approach. In *Proceedings of the 4th International Symposium on Production Control in the Metalworking Industry*, 1986.

[63] R. Groppetti and Q. Semeraro. CAPP - Computer Aided Process Planning using Relational Data Bases. In *Proceedings of the 15th ISATA*

International Symposium on Automotive Technology and Automation, 1986.

[64] X. Zhou, Y. Qiu, G. Hua, H. Wang, and X. Ruan. A feasible approach to the integration of CAD and CAPP. *Computer-Aided Design*, 39(4):324 – 338, 2007.

[65] J. Han, I. Han, E. Lee, and J. Yi. Manufacturing feature recognition toward integration with process planning. *Systems, Man, and Cybernetics, Part B: Cybernetics, IEEE Transactions on*, 31(3):373 –380, jun. 2001.

[66] M. Kang, J. Han, and J. G. Moon. An approach for interlinking design and process planning. *Journal of Materials Processing Technology*, 139(1-3):589 – 595, 2003. IMCC2000 Vol. 2 S.I.

[67] B. S. Prabhu, S. Biswas, and S. S. Pande. Intelligent system for extraction of product data from CADD models. *Computers in Industry*, 44(1):79 – 95, 2001.

[68] ISO Standard 6983-1:1982. *Numeric control of machines - Program format and definition of address words - Part 1: Data format for positioning, line motion and contouring control systems*. International Standard Organisation, Geneva, Switzerland, 1982.

[69] X. W. Xu and Q. He. Striving for a total integration of CAD, CAPP, CAM and CNC. *Robotics and Computer-Integrated Manufacturing*, 20(2):101 – 109, 2004.

[70] Kemmerer S. J., editor. *STEP, the grand experience*. National Institute of Standards and Technology, 1999.

[71] ISO Standard 14649-1:2003. *Industrial automation systems and integration - Physical device control - Data model for computerized numerical*

controllers - Part 1: Overview and fundamental principles. International Standard Organisation, Geneva, Switzerland, 2003.

[72] X. W. Xu, H. Wang, J. Mao, S. T. Newman, T. R. Kramer, F. M. Proctor, and J. L. Michaloski. STEP-compliant NC research: the search for intelligent CAD/CAPP/CAM/CNC integration. *International Journal of Production Research*, 43:3703–3743(41), 1 September 2005.

[73] Y. Yusof, N. Tan, and N. Kasim. Exploring the ISO14649 (STEP-NC) for Intelligent Manufacturing System. *European Journal of Scientific Research*, 36(3):445–457, 2009.

[74] N. Rychtyckyj, E. Klampfl, O. Gusikhin, and G. Rossi. Application of intelligent methods to automotive assembly planning. In *Systems, Man and Cybernetics, 2007. ISIC. IEEE International Conference on*, pages 2479 –2483, oct. 2007.

[75] Y. Shi, S. Zhang, H. Fan, J. Cao, and Y. Yang. Process Information-Driven 3D Working Procedure Model Construction. *International Symposiums on Information Processing*, 0:477–481, 2008.

[76] S. M. Ross. *Stochastic Processes*. Wiley, 1995.

[77] L. R. Rabiner. A Tutorial on Hidden Markov Models and Selected Applications in Speech Recognition. In *Proceedings of the IEEE*, pages 257–286, 1989.

[78] L. Baum, T. Petrie, G. Soules, and N. Weiss. A Maximization Technique Occurring in the Statistical Analysis of Probabilistic Functions of Markov Chains. *The Annals of Mathematical Statistics*, 41(1):164–171, 1970.

[79] G. N. Saridis, G. C. S. Lee, and J. Graham. An integrated syntactic approach and suboptimal control for manipulators and prosthetic arms. In

Decision and Control including the Symposium on Adaptive Processes, 1979 18th IEEE Conference on, volume 18, pages 257 –262, dec. 1979.

[80] C. E. Shannon. A mathematical theory of communication. *SIGMOBILE Mob. Comput. Commun. Rev.*, 5(1):3–55, 2001.

[81] D. Jurafsky and J. H. Martin. *Speech and Language Processing: An Introduction to Natural Language Processing*. Prentice Hall, 2000.

[82] P. Brown, J. Cocke, S. Della Pietra, V. Della Pietra, F. Jelinek, J. Lafferty, R. Mercer, and P. Roossin. A statistical approach to machine translation. *Comput. Linguist.*, 16(2):79–85, 1990.

[83] P. Koehn, F. Och, and D. Marcu. Statistical phrase-based translation. In *NAACL '03: Proceedings of the 2003 Conference of the North American Chapter of the Association for Computational Linguistics on Human Language Technology*, pages 48–54, Morristown, NJ, USA, 2003. Association for Computational Linguistics.

[84] S. Pini, S. Han, and D. R. Wallace. Text entry for mobile devices using ad-hoc abbreviation. In *AVI '10: Proceedings of the International Conference on Advanced Visual Interfaces*, pages 181–188, New York, NY, USA, 2010. ACM.

[85] Olympus Corp. www.microscopy.olympus.eu, 2010.

[86] A.Y. Fasasi, S. Mwenifumbo, N. Rahbar, J. Chen, M. Li, A.C. Beye, C.B. Arnold, and W.O. Soboyejo. Nano-second UV laser processed micro-grooves on Ti6Al4V for biomedical applications. *Materials Science and Engineering: C*, 29(1):5 – 13, 2009.

[87] ISO Standard 13565-2:1996. *Geometrical Product Specification (GPS) - surface texture: profile method; surfaced having stratified functional properties. Part 2: Height Characterization Using the Linear Material*

Ratio Curve. International Standard Organisation, Geneva, Switzerland, 1996.

Appendix A

Implementation of the process control software

The process control software consists of the series of LabVIEW VIs enumerated in Section 3.3.2. In the following, the implementations (diagram blocks) of a number of VIs are reported.

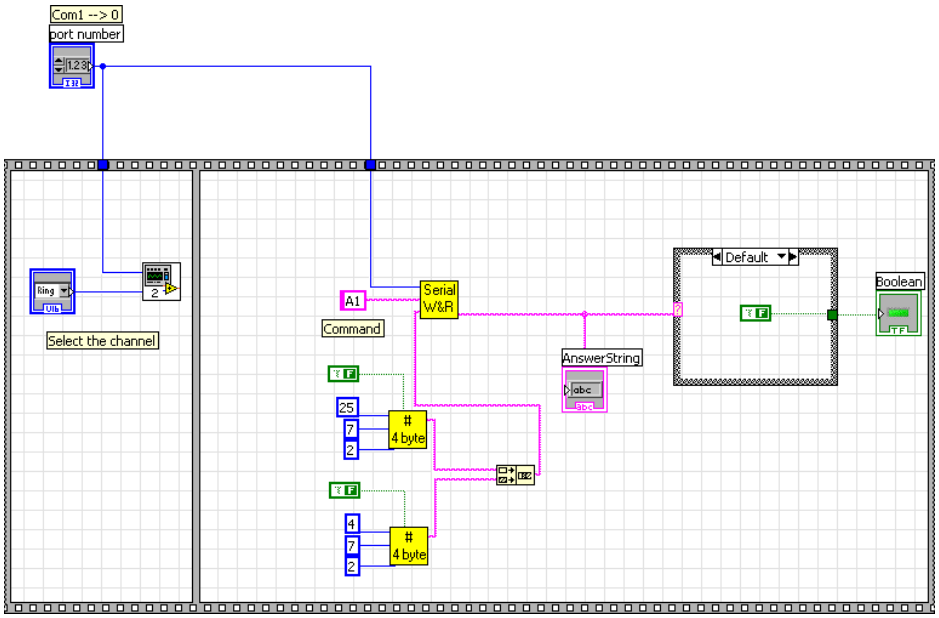

Figure A.1: Diagram block of *SetAxisVelocity.vi*.

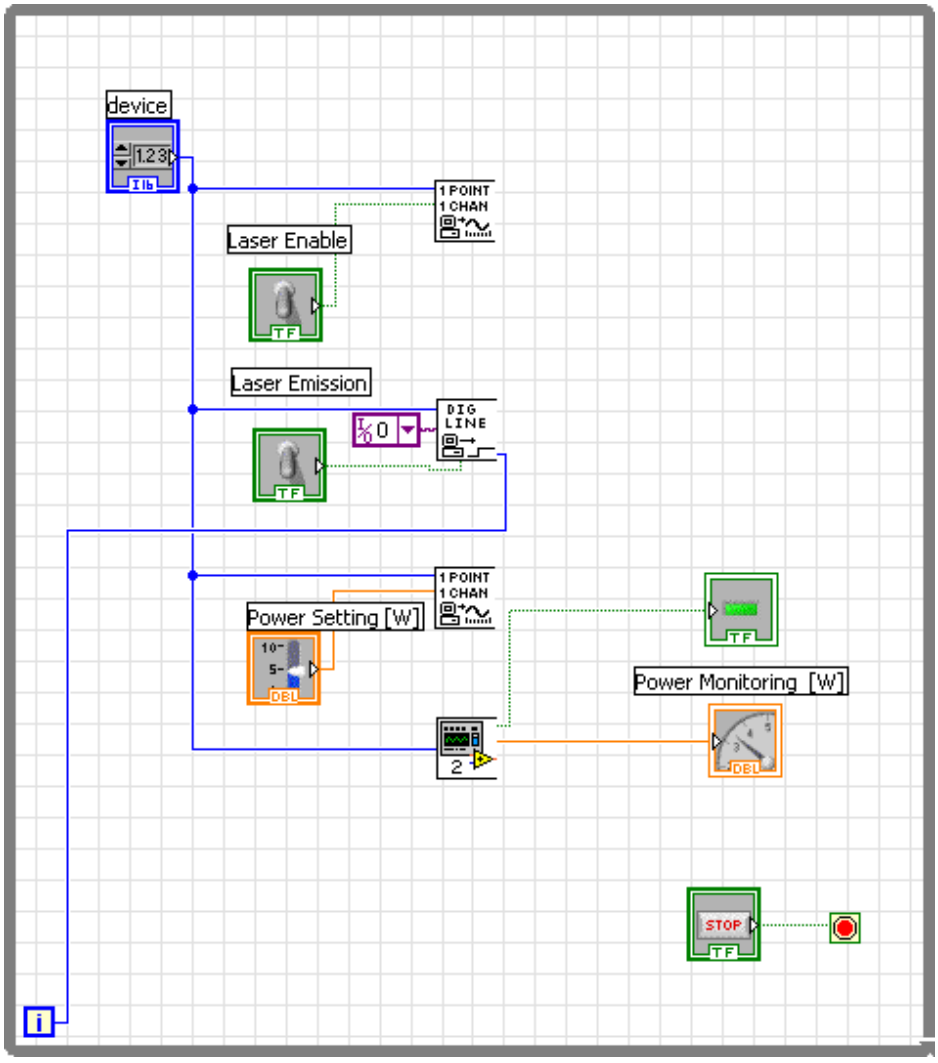

Figure A.2: Diagram block of *LaserInterface.vi*.

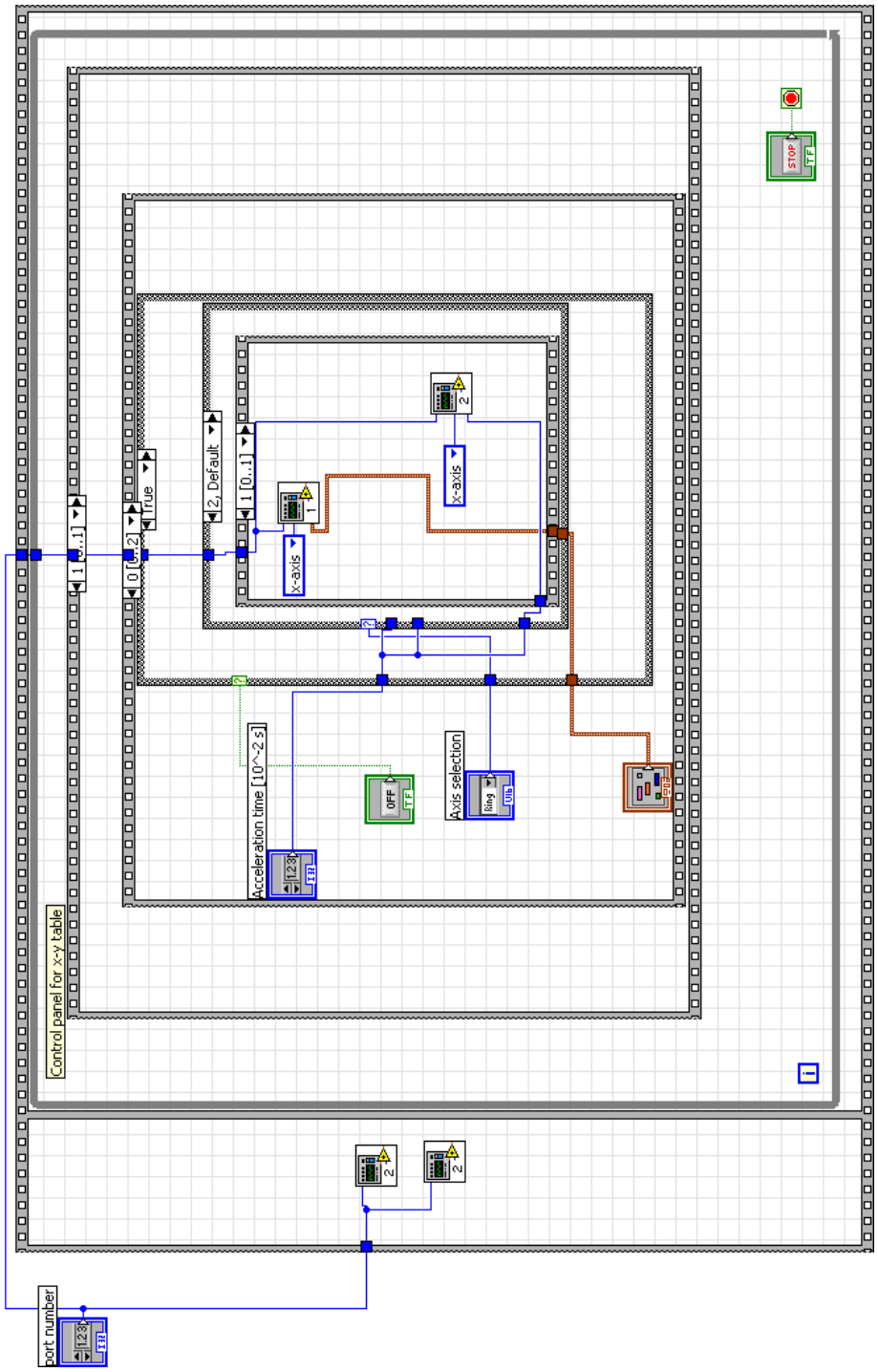

Figure A.3: Diagram block of *xyTableInterface.vi*.

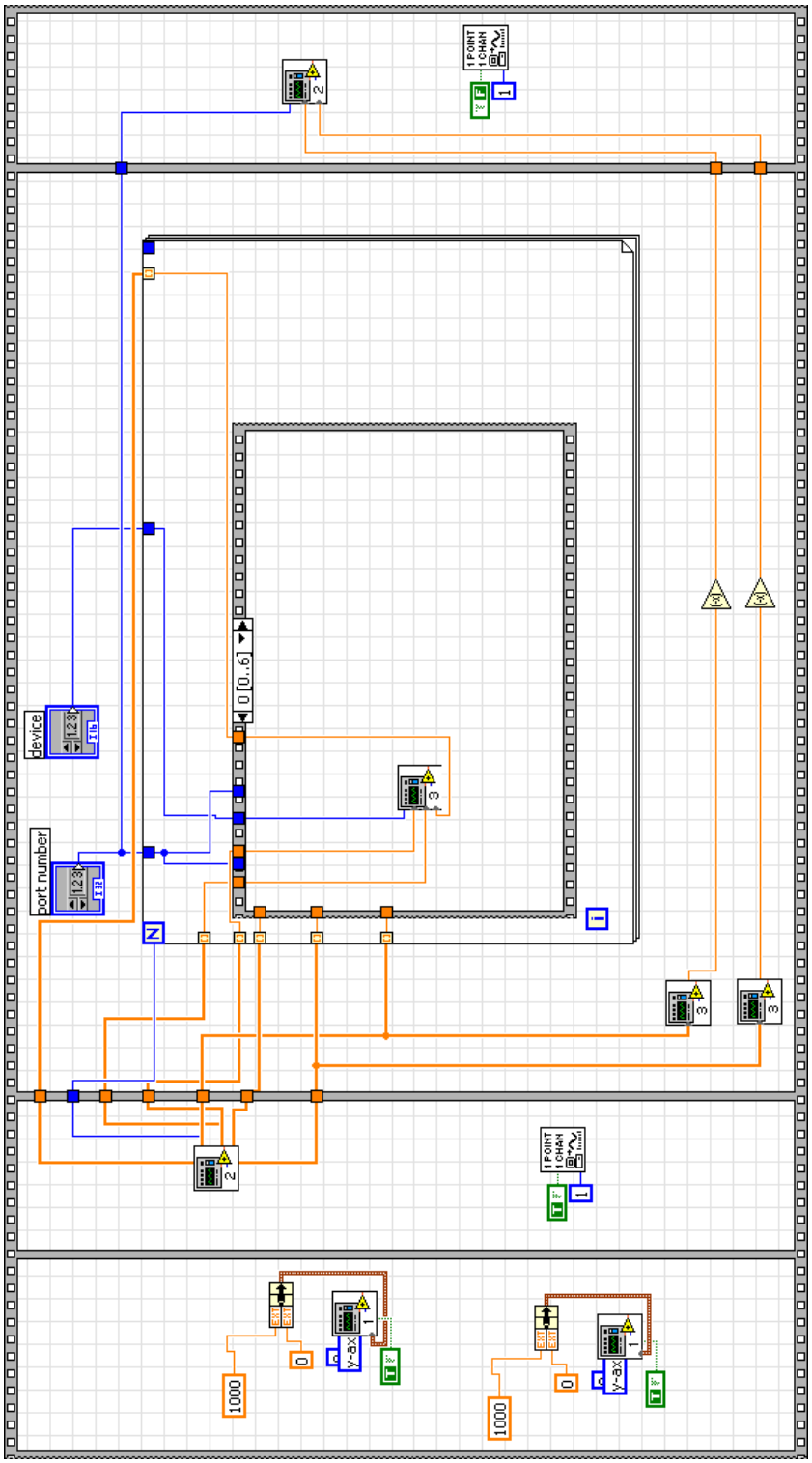

Figure A.4: Diagram block of *BatchDrilling.vi*.

Appendix B

Implementation of the system for part programming input in natural language

The full source code of the software for the translation of part programs expressed in natural language is reported in the following.

Listing B.1: Source code of the *training* module of the software for part programming in natural language.

```
def trainLanguageModel(languageModelTrainingSet):

    print('################\nBuilding start
                        probability vector...\n')

    start_probability = {}

    transition_probability = {}

    for line in languageModelTrainingSet:
        for w in line.split():
            start_probability.update( { w : line.count(w) } )
```

```
    count = 0
    for word, freq in start_probability.iteritems():
16      count = count + freq

    for word, freq in start_probability.iteritems():
        start_probability[word] = freq / count

21  print('...done\n################\n')

    print('################\nBuilding transition
                        probability matrix...\n')

26  transitions = []
    allWords = []

    for line in languageModelTrainingSet:
        wordList = line.split()
31      counter = 0
        for word in wordList:
            allWords.append(word)
            dest = counter +1;
            if dest < len(wordList):
36              transitions.append(
                        (word, wordList[dest]) )
            counter = counter +1

    # delete duplicates in word list
41  uniqueWordList = unique(allWords)

    for word1 in uniqueWordList:
        transition_probability.update( {word1 : {} })

46  for word1 in uniqueWordList:
        # fill the matrix (transition occurances)
        for word2 in uniqueWordList:
```

```
            (transition_probability[word1])
                .update( { word2 : transitions
                        .count( (word1, word2) ) } )

        # count along the rows
        count = 0
        for word2 in uniqueWordList:
            if (transition_probability[word1][word2] == 0):
                (transition_probability[word1])
                        .update( { word2 : 0.000000001 } )

            count = count + transition_probability[word1][word2]

        # normalize the rows (from occurances to frequencies)
        for word2 in uniqueWordList:
            (transition_probability[word1])
                .update( { word2 :
                transition_probability[word1][word2] / count } )

        states = tuple(uniqueWordList)

    print('...done\n################\n')

    return [states, start_probability, transition_probability]


def trainTranslationModel(translationAlignments):

    print('################\nBuilding translation matrix...\n')

    wordList1 = []
    wordList2 = []

    for word1, word2 in translationAlignments:
        wordList1.append(word1)
        wordList2.append(word2)
```

```
86      # delete duplicates in word list
        uniqueWordList1 = unique(wordList1)
        uniqueWordList2 = unique(wordList2)

        translation_probability = {}
91
        # create a empty translation matrix
        for word1 in uniqueWordList1:
            translation_probability.update( {word1 : {} })

96      for word1 in uniqueWordList1:
            # fill the matrix (transition occurances)
            for word2 in uniqueWordList2:
                occurences = translationAlignments
                                    .count( [word1, word2] )
101             (translation_probability[word1])
                                    .update( { word2: occurences } )
            # count along the rows
            count = 0
            for word2 in uniqueWordList2:
106             if (translation_probability[word1][word2] == 0):
                    (translation_probability[word1])
                                    .update( { word2 : 0.000000001 } )

                count = count + translation_probability[word1][word2]
111
            # normalize the rows (from occurances to frequencies)
            for word2 in uniqueWordList2:
                (translation_probability[word1])
                                    .update( { word2 :
116                 translation_probability[word1][word2] / count } )

        print('...done\n################\n')

        return translation_probability
```

Listing B.2: Source code of the *decode* module of the software for part programming in natural language.

```
# retrieve the most probable state sequence
# given an observation sequence
def decode(obs, states, start_p, trans_p, emit_p):
    V = [{}]
    path = {}

    # step at t = 0
    for y in states:
        V[0][y] = start_p[y] * emit_p[y][obs[0]]
        path[y] = [y]

    # step at t > 0
    for t in range(1,len(obs)):
        V.append({})
        newpath = {}

        for y in states:
            (prob, state) = max([(V[t-1][y0] * trans_p[y0][y]
                        * emit_p[y][obs[t]], y0) for y0 in states])
            V[t][y] = prob
            newpath[y] = path[state] + [y]

        path = newpath

    trellis(V)
    (prob, state) = max([(V[len(obs) - 1][y], y) for y in states])
    return (prob, path[state])
```

Listing B.3: Source code of the main function of the software for part programming in natural language.

```
# main function
def processNaturalLanguageInput
                (parallelCorpusFilename,
                inputFilename,
                outputFilename):

    [languageModelTrainingSet,
        translationAlignments] = getAlignmentsFromFile(
                                        parallelCorpusFilename)

    [states, start_probability,
        transition_probability] = trainLanguageModel(
                                        languageModelTrainingSet)

    emission_probability = trainTranslationModel(
                                        translationAlignments)

    inputFile = open(inputFilename)
    outputFile = open(outputFilename, "wt")

    observations = []
    items = []
    observationList = []
    stateChain = []

    while 1:
        line = inputFile.readline()
        line = line.lower()
        if line:
            items = line.split()
            numbers = []
            counter = 0
            for item in items:
                if not is_number(item):
```

```
                observationList.append(item)
            else:
                numbers.append(item)
                observationList.append('num')

            counter = counter +1

        observations = tuple(observationList)

        observationList = []

        [prob, path] = decode(observations,
                              states,
                              start_probability,
                              transition_probability,
                              emission_probability)

        numbers.reverse()

        stateChain = []

        for item in path:
            if item == '<num>':
                number = numbers.pop()
                stateChain.append(number)
            else:
                stateChain.append(item)

        outputFile.write(' '.join(stateChain) + '\n')

    if not line:
        break
    pass

inputFile.close()
outputFile.close()
```

Listing B.4: Source code of the utility functions of the software for part programming in natural language.

```
# extract translation alignments
def getAlignmentsFromFile(filename):

    file = open(filename)

    translationAlignments = []
    wordList = []
    lines = []

    while 1:
        line = file.readline()
        for word in line.split():
            word = word.lower()
            currentPair = word.split(':')
            wordList.append(currentPair[0])
            translationAlignments.append(currentPair)

        if line:
            lines.append(' ' + ' '.join(wordList) + ' ')
            wordList = []
        if not line:
            break
        pass

    file.close()

    return [lines, translationAlignments]


# delete duplicates in word list
def unique(a):
    if len(a) == 0:
        return []
    else:
```

```
        return [a[0]] + unique([x for x in a if x != a[0]])


# check whether the input is a number
def is_number(s):
    try:
        float(s)
        return True
    except ValueError:
        return False

# print Viterbi trellis
def trellis(V):
    print "    ",
    for i in range(len(V)): print "%7s" % ("%d" % i),
    print

    for y in V[0].keys():
        print "%.5s: " % y,
        for t in range(len(V)):
            print "%.7s" % ("%f" % V[t][y]),
        print
```

Appendix C

Main experimental data

In this appendix the main experiment data obtained in the microogrooving experiments (Sections 5.2 and 5.2) are reported.

Table C.1: Average depth and width measurements of microgrooves obtained by Fiber Laser micromachining of AISI 304 specimens.

#	Power $[W]$	Feed rate $[mm\ s^{-1}]$	Depth $[\mu m]$	Width $[\mu m]$
1	1.5	2	0.49	15.10
2	1.5	4	0.30	13.26
3	2.5	0.5	1.68	35.02
4	2.5	4	0.93	27.78
5	1.5	0.5	1.27	27.63
6	3.5	1	1.33	43.22
7	1.5	1	0.76	19.27
8	2.5	2	2.57	36.87
9	3.5	0.5	0.47	6.70
10	2.5	1	5.13	42.60
11	3.5	4	2.36	42.90
12	3.5	2	2.79	45.71

Table C.2: Average depth and width measurements of the piled-up material on the sides of microogroves obtained by Fiber Laser micromachining of AISI 304 specimens.

#	Power $[W]$	Feed rate $[mm\ s^{-1}]$	Height $[\mu m]$	Width $[\mu m]$
1	1.5	2	0.87	12.29
2	1.5	4	0.46	15.50
3	2.5	0.5	1.50	19.46
4	2.5	4	0.63	12.87
5	1.5	0.5	0.92	20.01
6	3.5	1	0.97	12.49
7	1.5	1	0.77	15.74
8	2.5	2	0.77	10.91
9	3.5	0.5	2.18	31.07
10	2.5	1	0.89	14.37
11	3.5	4	0.61	10.33
12	3.5	2	0.83	12.61

Table C.3: Average depth and width measurements of microgrooves obtained by Fiber Laser micromachining of DLC-coated AISI 440 specimens.

#	Power $[W]$	Feed rate $[mm\ s^{-1}]$	Depth $[\mu m]$	Width $[\mu m]$
1	2	1	2.58	46.65
2	2.5	2	1.91	36.61
3	1.5	1.5	0.82	24.58
4	2	2	1.37	21.83
5	1.5	2	5.30	39.03
6	1.5	2.5	2.60	40.24
7	1.5	1	1.43	40.60
8	2	1.5	1.28	36.68
9	2.5	2.5	4.27	34.86
10	2	2.5	0.56	18.16
11	2.5	1.5	1.11	25.26
12	2.5	1	1.09	13.70

Table C.4: Average depth and width measurements of the piled-up material on the sides of microogroves obtained by Fiber Laser micromachining of DLC-coated AISI 440 specimens.

#	Power $[W]$	Feed rate $[mm\ s^{-1}]$	Height $[\mu m]$	Width $[\mu m]$
1	2	1	0.33	7.30
2	2.5	2	0.65	7.18
3	1.5	1.5	0.79	14.50
4	2	2	1.16	9.81
5	1.5	2	0.33	3.67
6	1.5	2.5	0.22	10.02
7	1.5	1	0.35	8.94
8	2	1.5	0.48	11.50
9	2.5	2.5	0.92	10.45
10	2	2.5	0.81	12.46
11	2.5	1.5	1.39	14.60
12	2.5	1	1.11	22.35